5-1-2010

Robust control strategies for hybrid solid oxide fuel cell systems

Tahar Allag

ROBUST CONTROL STRATEGIES FOR HYBRID SOLID OXIDE FUEL CELL SYSTEMS

by

Tahar Allag

A Thesis Submitted in Partial Fulfillment of the Requirements for the Degree of
Master of Science in Electrical Engineering

Advised by

Dr. Tuhin Das, Assistant Professor, Mechanical Engineering
Department of Electrical Engineering
Kate Gleason College of Engineering
Rochester Institute of Technology
Rochester, New York
May 2010

Approved By:

Dr. Tuhin Das,
Assistant Professor, Mechanical Engineering
Advisor _____

Dr. Mark A. Hopkins,
Associate Professor, Electrical Engineering _____

Dr. Athimoottil Mathew,
Professor, Electrical Engineering _____

Dr. Sohail A. Dianat,
Interim Department Head -Professor, Electrical Engineering _____

Thesis Release Permission Form

Rochester Institute of Technology

Kate Gleason College of Engineering

Robust Control Strategies for Hybrid Solid Oxide Fuel Cell Systems

I, Tahar Allag, hereby grant permission to the Wallace Memorial Library reproduce my thesis in whole or part.

Tahar Allag

Date

Acknowledgments

I would like to acknowledge the invaluable encouragement from my parents, family, and friends. I am heartily thankful to my supervisor, Dr. Tuhin Das, whose encouragement, guidance and support from the initial to the final level enabled me to develop an understanding of the subject, and the support provided by the Office of Naval Research under grants #N000140810704, and N000140910272 in conducting this research. Lastly, I offer my regards and blessings to all of those who supported me in any respect during the completion of the project. Most importantly, I thank God for granting me the strength, intelligence, and will to accomplish this task; may all the glory be unto Him.

Abstract

Solid Oxide Fuel Cell (SOFC) systems are electrochemical energy conversion devices characterized by the use of solid oxide as the electrolyte. They operate at high temperatures (between $800^\circ - 1000^\circ$C). Mitigating fuel starvation and improving load-following capability of SOFCs are conflicting control objectives. In this thesis, this issue is addressed using a hybrid SOFC ultra-capacitor configuration. The fuel cell is controlled by incorporating a steady-state property of fuel utilization into an input-shaping framework. Two comprehensive control strategies are developed. The first is a lyapunov-based nonlinear control and the second is a standard H_∞ robust control. Both strategies additionally control the state of charge (SOC) of the ultra-capacitor that provides transient power compensation. A hardware-in-the-loop test-stand is developed where the proposed control strategies are verified. An investigation to improve the hybrid fuel cell system by incorporating a lithium-ion battery as an additional power source is conducted. Combining both battery and ultra-capacitor with a fuel cell is potentially a winning combination especially for high power applications. A novel SOC estimation method for lithium-ion battery is investigated. Based on the combined ultra-capacitor battery hybrid system, a lyapunov-based nonlinear control strategy is designed.

Contents

List of Figures

Nomenclature

F	Faraday's constant ($= 96485.34$ coulomb/mol)
i	Current draw (A)
k	Anode recirculation fraction
N	Number of moles (moles)
$\mathcal{N}_{cell}$	Number of cells in series
$\dot{N}_{air}$	Molar flow rate of air (moles/sec)
$\dot{N}_f$	Molar flow rate of fuel (moles/sec)
$\dot{N}_{f,d}$	Molar flow rate demand of fuel (moles/sec)
$\dot{N}_{in}$	Anode inlet flow rate (moles/sec)
$\dot{N}_o$	Anode exit flow rate (moles/sec)
n	Number of electrons participating in electrochemical reaction ($= 2$)
$\mathcal{R}$	Species rate of formation (moles/sec)
R_u	Universal Gas Constant (8.314 J/mol/K)
T	Temperature (K)
V	Volume (m^3)
$\mathcal{X}$	Mole fraction
V_{cell}	Cell voltage (V)
U	Fuel utilization
U_{ss}	Steady state fuel utilization
V_{fc}	Fuel cell voltage (V)
i_{fc}	Fuel cell current (A)
V_L	Load current (V)

i_L	Load current (A)
V_{uc}	Ultra-capacitor voltage (V)
V_b	Battery voltage (V)
i_{uc}	Ultra capacitor current (A)
$i_{uc,c}$	Ultra-capacitor current command (A)
i_b	battery current (A)
n_1	Unidirectional dc/dc converter efficiency
n_2	Ultra-capacitor Grid Bi directional dc/dc converter efficiency
n_3	Battery Grid Bi directional dc/dc converter efficiency
C	Capacitor value 250 (F)
$\hat{g}(x,m)\hat{f}(x,m)$	Function evaluated at nominal values
δ	Uncertain nominal at 0 and bounded [-1 +1]
$\delta_1 \quad \delta_2 \quad \delta_{b1}$	Robustness terms
d	Disturbances [-1 to 1]
E_s	Error in ultra-capacitor state of chrage
E_{sb}	Error in battery state of charge
$E_{fc,t}$	Error between $i_{fc,t} - i_{fc,d}$
$E_{fc,t}$	Error between $i_{fc} - i_{fc,t}$
E_{fl}	Error between $\dot{N}_f - \dot{N}_{f,d}$
SOC	State of charge
S	State of charge of the ultra-capacitor
S_t	Target state of charge of the ultra-capacitor
$i_{fc,t}$	Fuel cell current target (A)
$i_{fc,d}$	Fuel cell current demande (A)
DC	Direct current
AC	Alternative current
$\bar{n}_1$	Estimated unidirectional dc/dc converter efficiency
$\bar{n}_2$	Estimated ultra-capacitor grid bi-directional dc/dc converter efficiency

$\bar{n}_3$	Estimated battery grid Bi-directional dc/dc converter efficiency
H_∞	H infinity
R	Resistance
V_{oc}	Open-circuit voltage

Subscripts

a	Anode control volume
c	Cathode control volume
i	Values of 1 through 7 represent
	CH_4, CO, CO_2, H_2, H_2O, N_2, and O_2
r	Reformer control volume

Chapter 1

Introduction

1.1 Motivation

In the twenty first century, the energy demand for survival of mankind has dramatically increased. The use of energy in people's daily lives is ubiquitous and pervasive [9]. However, the existing infrastructure is based only on fossil fuels that is depleting in reserves over time. Moreover fossil fuels pose a potential threat to the environment. This has triggered a significant interest in renewable energy resources. In recent years, alternate energy technologies have become a very important and attractive domain of research [10]. Fuel cell is one of the technologies that holds the promise for solving the increasing energy demands and simultaneously addressing environmental issues [11]. Several fuel cell technologies have been developed over the last decades, such as Polymer Electrolyte Membrane Fuel Cells (PEMFC), Alkaline fuel cells (AFC), Solid Oxide Fuel Cells (SOFC), and Molten Carbonate Fuel Cells (MCFC) [11].

Among different fuel cell technologies, SOFC technology has attracted significant interest in recent years [12]. They are solid state devices that produce electricity by electrochemical oxidation of fuel. SOFCs are fuel flexible, tolerant to impurities and operate at high temperatures ($800^\circ - 1000^\circ$C). However, due to their high costs and a very demanding safety requirement infrastructures, adoption has not been widespread, with most installations occurring in niche applications with heavy subsidy [13]. SOFC uses solid state oxide ion-conducting material as electrolyte. It is composed of three parts, Electrolyte, Anode

and Cathode. The electrolyte is composed of zirconia doped with 8 to 10 mole $\%$ yttria that has high capability of conducting oxygen ions. The anode is usually a zirconia cermet, a mixture of ceramic and metal. The anode and cathode must allow mass transport of reactant and product gases. The cathode is composed of strontium-doped lanthanum manganese [12].

There are many more advantages of Solid Oxide Fuel Cell (SOFC) systems over other types of fuel cell system technologies. They are simpler in concept of operation than other fuel cells. High temperature operating conditions (800° to 1000°C) in SOFCs are conducive to internal reforming of fuels and hot exhaust gases from SOFC systems are excellent means for sustaining on-board fuel reforming [11, 12]. They are not only tolerant to carbon monoxide but they can also be used as fuel, as opposed to other fuel cell types. These properties substantially simplify fuel reforming in SOFC systems and make them well poised for use with a variety of fuels.

Furthermore, high operating temperatures makes SOFC-GT (Gas-Turbine) hybrids excellent combined heat and power (CHP) systems that can achieve system efficiencies that surpass normal limitations of GT systems [14]. However, SOFCs are limited due to their poor load following capability. This is a drawback of Solid Oxide Fuel Cells. To have a better understanding of the SOFCs performance, understanding some of its performance variables is needed. One of the important performance variables of SOFCs is fuel utilization. It is defined as the ratio, often expressed in percentages, of hydrogen consumption by the fuel cell to the net available hydrogen in the anode inlet flow.

High utilization is needed for better efficiencies. Typically, the desired utilization is around 80 to 90 $\%$ [15, 16]. However, very high utilization leads to reduce partial pressure of hydrogen in the fuel cell anode, which causes voltage drop and irreversible damages due to anode oxidation. In applications with significant power transients, the resulting fluctuations in the fuel utilization and repeated and prolonged deviation from target can adversely affect stack life [14, 17, 18], more detailed discussion will be provided in the forthcoming sections.

1.2 Literature Review

The environmental goals to reduce global warming and the necessity to eliminate CO_2 emissions encourage us to look for better energy conversion devices. The motor vehicle industry is seeking for high fuel efficiency devices and less CO_2 emissions. The utility industries, following the impact of privatization and competition strive them to find comprehensive and up-to-date technologies for their applications. These reasons have stimulated the interest in the new expanding technology of fuel cells systems.

A lot of work has been done on fuel cell system in the last decades. Different types of fuel cell have been developed. Each type has advantages and disadvantages. Alkaline Fuel Cells (AFC) were the first fuel cell to be used in real life applications [19]. They are used in space vehicles. They have very high efficiency. The slow reaction of this fuel cells is a drawback that is resolved by using porous electrodes with platinum catalyst. They operate at low temperatures around $200°$C. Another disadvantage of AFCs is that they are very sensitive to carbon dioxide [20]. Hence CO_2 must be filtered out from air before supplying to the fuel cell. This poses cost restrictions on the use of AFCs.

On the other hand, Molten Carbonate Fuel Cell (MCFC) are not poisoned by CO_2 [12]. In fact, it can be used by MCFCs as fuel. They are in the class of high-temperature fuel cells. They can only reach around 45 to 47 $\%$ of efficiency [9, 21]. This is a draw back that prevents applications of MCFCs where efficiency is important.

Another well-known fuel cell type is Direct Methanol Fuel Cells (DMFC). They are supplied directly with methanol [22]. An advantage of DMFCs is compact storage because of the high density of methanol. DMFC is a relatively new technology that requires significant improvements before wider applications are feasible. Moreover, these cells have very low efficiency [12].

The first modern fuel cell module to be used as power generators is Phosphoric Acid Fuel Cells (PAFC) [23]. They use proton-conducting electrolyte. They are considered as a medium temperature fuel cells. Their high efficiency operation ($\approx 80\%$) in producing

power and heat has led to widespread use. However, producing only electricity, their efficiency does not exceed 50%. Due to economical issues, the use of this type of fuel cell has slow down lately [12].

Polymer Electrolyte Membrane Fuel Cells (PEMFC) are mostly used in transport and non-stationary applications [10, 13, 24]. They are also called Proton Exchange Membrane Fuel Cell. They are desired in non-stationary applications because of their high power density and low volume and weight [25]. However PEMFCs have draw backs such as sensitivity to impurities in the fuel source, especially carbon monoxide CO, and requiring supply of pure hydrogen [26].

Each fuel cell type solves some problems, but brings difficulties of its own. Solid Oxide Fuel Cells are high temperature fuel cells. This characteristic allows them to remove the need for precious metal catalyst, thus reduces its costs relatively. Also, they are not only tolerant to carbon monoxide but they can used it as fuel as opposed to other fuel cell types. The efficiency of SOFC is very high with proper utilization of the fuel in the fuel cell stack. However, very high utilization can cause permanent damages to fuel cell anode [16]. Thus, controlling the utilization properly is needed to have higher efficiency. SOFCs can be well suited for many types of applications. Due to all these advantages, many researchers are interested to develop SOFC to be applicable in more demanding applications.

In spite of these attributes, application of SOFCs has been limited due to their poor load following capability, and has particularly precluded their use in application involving rapid power variations [13]. Poor load following ability is a common drawback of any type of fuel cells. It is attributed to the slow dynamic response of the fuel and air delivery systems consisting of valves, pumps and reformers, [27], [28], [29], [18]. It is manifested as hydrogen or oxygen starvation, drastic voltage drop, compressor surge and choke, when the fuel cell is directly exposed to rapid power transients. The phenomenon adversely affects the cell's durability through anode oxidation [18], and through reversal of cell potential leading to catalyst corrosion [17].

Multiple authors have addressed this issue by augmenting the fuel cell with an electrical

storage device. In [27], the authors present an approach of interfacing an ultra-capacitor to a fuel cell and develop a current control strategy to minimize the fuel cell's voltage drop during sudden increase in the load. This interfacing between the primary and the secondary source of energy is relayed on bidirectional power electronic devices. The control strategy is based on observing the terminal voltage of the fuel cell by controlling the ultra-capacitor currents. Simulation results show gradual prevention in any substantial drop in the fuel cell voltage as the load power increases.

In [28], a control principle of the hydrogen utilization of PEM fuel cells is addressed. The current in the fuel cell is rate limited. $i.e.$ fuel cell current slope is controlled to prevent hydrogen starvation. The strategy is based on a DC link voltage regulation in order to make the fuel cell operate in steady state condition. The fuel cell is considered as a main power source and an ultra-capacitor is used as an auxiliary storage device. Power from the ultra-capacitor is drawn in a manner that minimizes mechanical stresses on the fuel cell. The ultra-capacitor current draw is synchronized with the fuel flow of the PEM fuel cell system and the current draw from the load.

Oxygen starvation problem in PEM fuel cells is addressed in [30]. A nonlinear reference governor approach is developed to address this issue. Parameter uncertainties are addressed using a novel approach based on sensitivity functions. The main objective of this paper is to incorporate robust control while solving the oxygen starvation problem in the fuel cell. Simulation results are included to demonstrate the effectiveness of the proposed scheme. In [29], a Model Predictive Control (MPC) is developed for a fuel cell ultra-capacitor system that minimizes oxygen starvation, bounds the ultra-capacitor's state-of-charge (SOC), and prevents compressor surge and choke while responding to power demands from the load. An MPC based approach for improving battery performance and avoiding fuel cell and battery degradation is given in [31].

In addition, a number of papers have proposed control of hybrid fuel cells without specifically addressing the above mentioned constraints, but providing a rich spectrum of

control approaches. In [32–34], rule-based control strategies are developed where the hybrid system switches between discrete operating modes. In [32], the authors focus on starting condition and the reverse regeneration of energy during braking situations. They model the fuel cell ultra-capacitor hybrid vehicle power system and design a model-based controller.

In [33], the authors focus on cars powered by fuel cells and equipped with an ultra-capacitor and a battery at the same time. They investigate a strategy to reduce fuel consumption of the vehicle. Their goal is to reduce the hydrogen consumption while maintaining the state-of-charge of the ultra-capacitor and the battery at acceptable levels. The ultra-capacitor captures significant amount of energy during braking and protects the fuel cell from instantaneous peaks in the load power. Whereas, for long duration braking and excessive power spikes the battery is used. Thus, the fuel consumption is reduced significantly.

In [34], an on-line power management system is proposed for a hybrid fuel cell. The authors of this paper discuss a method that includes an advance supervisory controller consisting of multiple layers. In the first layer, the controller captures all possible operation modes. In the second layer of the controller, a fuzzy logic algorithm is used to split the power between the fuel cell and the auxiliary power module. In the last layer, there are sub-controllers that set the operating point for each subsystem to reach the optimum performance.

In [35], adaptive control strategy adjusts the output current of the fuel cell according to the state-of-charge of the secondary power source. In [36], a two-loop control strategy is proposed for a fuel cell ultra-capacitor hybrid. The inner loop regulates the DC bus voltage and the outer loop regulates the fuel cell current. The authors considered the SOFC stack operating only at relative low pressure and are concerned about the thermal dynamics in their control design. In [37], a fuel cell system is hybridized with ultra-capacitor and battery. A non-linear sliding-mode control is developed for power management of this hybrid system. The ultra-capacitor module is used as an auxiliary transient power source

and the battery is used for long duration peaks. In [38], the authors obtain optimal power distribution in real-time by local minimization of an equivalent fuel consumption variable.

In [39], the authors develop a differential flatness ([40]) based control for a fuel cell ultra-capacitor system. The ultra-capacitor is used as secondary power source whereas the fuel cell is used as the main power supplier. The hybrid system also consists of two capacitors, DC link capacitor and output capacitor. The DC link capacitor connects both the primary and secondary power sources to the grid and the output capacitor connects the load and the grid through power electronic devices. The control strategy is based on energy regulation of both capacitors. The main source output voltage is kept constant and its dynamics are controlled.

A majority of the work mentioned above pertain to PEMFCs and appear to lack a holistic approach to the control of hybrid fuel cells. Literature review reveals that control development for hybrid SOFCs systems are in preliminary stages.

1.3 Basic Operating Principle of SOFCs

Solid Oxide Fuel Cell uses electrochemical reactions to produce electricity. The particular electrochemical reaction employed is illustrated in Fig.1.1. Hydrogen fuel and air flow through the anode and cathode, respectively. The anode collects electrons that pass through the load and are deposited back again in the cathode. The electrolyte is a dense layer of ceramic that conducts only oxygen ions. It is not a membrane, as in other types of fuel cells, that is permeable to molecules or atoms. Rather, it is a pure ionic conductor allowing only the oxygen ions to pass through, but only at elevated temperatures [41]. Thus, in order to complete the circuit, oxygen ions passes through the solid oxide electrolyte from the cathode to the anode.

Hydrogen is used as the primary fuel for generating electricity, but SOFC systems do not require pure hydrogen as the fuel. Due to the high operating temperatures (800 to 1000°C) and the presence of catalysts, hydrogen can be generated through internal reforming within

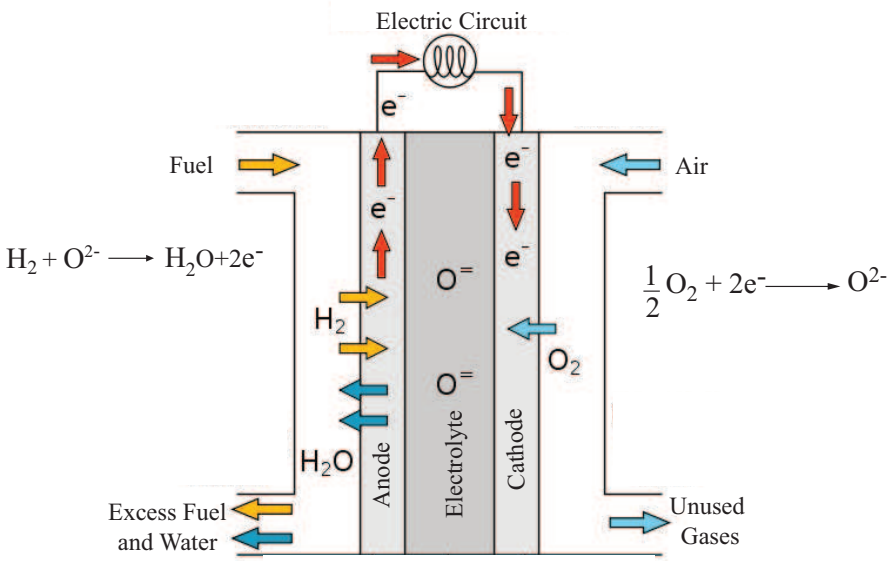

Figure 1.1: Basic Electrochemistry of an SOFC (Figure courtesy [1])

the anode chamber of an SOFC from hydrocarbon fuels [11, 12]. It is also generated through external reforming in reformers placed upstream of fuel cell. Some reforming processes are endothermic and so the hot gases exhausted from the fuel cell can serve as a means of providing heat to sustain those reformers [2]. In addition, exothermic reforming processes such as POX (Partial Oxidation) reforming exist where the fuel is partially oxidized to self-sustain the reforming process. More detailed explanation will be provided in the forthcoming sections.

As discussed previously, fuel utilization U is defined as the ratio of hydrogen consumption to the net available hydrogen in the anode of an SOFC. In the mathematical formulation of U, not only the available hydrogen but also the hydrogen that can be generated from other species through internal reforming, are accounted for [15, 42]. This is because of SOFC's tolerance to impurities that allows the reformer exhaust gas-mixture to be directly sent to the anode with minimal or no purification. While high utilization implies high efficiency, very high utilization leads to reduced partial pressure of hydrogen in the anode, leading to

voltage drop and irreversible damages due to anode oxidation [18]. Typically, $80 - 90\%$ is set as the target range [15, 16, 42].

1.4 Objectives

Control of U around a target value is a means for improving load-following in SOFC systems. However measurement of U requires a number of species-specific concentration sensors that are avoided due to cost and reliability considerations. Observer designs are possible [10, 43–45], however they are computation intensive, and rely on accurate mathematical models.

In this thesis, proposes control of U by combining an *invariant property* of the SOFC system [14], with a feedback based current regulation strategy. The invariant property is a closed-form expression relating steady-state U, fuel flow and current but is independent of variables such as reforming reaction rates, internal flow rates, temperatures, etc. The approach not only satisfies a target steady-state U but also attenuates its transient departure from this target.

The dynamics of the fuel supply system (FSS) consisting of fuel pump, compressor and /or valves, are considered unknown and the measured fuel flow is used to regulate the fuel cell current. The deficit or surplus power delivered by the SOFC due to current regulation is compensated by a storage element such as an ultra-capacitor or a battery. Current regulation is incorporated within an robust control scheme that additionally controls the storage element's SOC.

This work addresses hydrogen starvation but oxygen starvation is not considered as it is seldom observed in SOFC systems. This is because in the absence of coolants, excess air (Air utilization $\approx 20 - 25\%$, [46]) is used for temperature control of the fuel cell stack [18].

The auxiliary power storage element has to be chosen such that it responds appropriately to power delivery requirements on the hybrid system. It has to be able to store

sufficient energy and provide adequate peak power during transients [47]. In addition, the storage unit must meet the required life cycle. The ultra-capacitor proposed in the SOFC-Ultra-capacitor hybrid system cannot supply the fuel cell with long power peaks and cannot store sufficient amount of energy. Batteries have higher energy and can provide the system with power for longer period of time. However ultra-capacitors have longer life time in terms of charging and discharging cycles [48].

The primary objective is to develop robust control strategies for power-split control of a hybrid SOFC ultra-capacitor hybrid that delivers superior load-following capability of the system while attenuating transient fuel utilization. The control objectives are satisfied in presence of uncertainties. Two control strategies are developed, a nonlinear control and an H_∞ based control.

This is followed by an investigation to combine both the ultra-capacitor and battery as auxiliary storage units of the hybrid fuel cell system. Recent studies show that lithium-ion batteries are most suitable elements for high power applications [49, 50]. Thus, studying and characterizing this battery is required to design a robust nonlinear control for SOFC-Battery-Ultra-capacitor hybrid system.

This thesis is organized as follows: A detailed Solid Oxide Fuel Cell system description is provided in section 2.1 and the uncontrolled response of U to transient current is presented in section 2.2. The invariant property is derived next and used for open-loop control in section 2.3. The feedback based current regulation method is presented in section 2.4 followed by a discussion on system induced delays on fuel flow in section 2.5. An overview of batteries and ultra-capacitors are presented in sections 3.1 and 3.2 respectively. The hybrid fuel cell ultra-capacitor configuration is presented in details in section 3.3.

Chapter 4 describes detailed control design strategies used in the hybrid system. The objectives of these control approaches are presented in section 4.1. In section 4.2, a nonlinear control design is presented and the mathematical derivation are shown in details. Proofs of all theorems used for this control strategy are presented in this section. Section 4.3 shows the second control strategy, which uses the H_∞ approach.

The hardware-in-the-loop (HIL) experimental test-stand is explained in chapter 5, where all equipments used for the test stand are described in details and specifications are given. Validation of real time simulations against the computer-model simulations are shown in section 6.1. Experimental results are presented in section 6.2 and 6.3 to confirm the validity of both the nonlinear and H_∞ control designs under step changes and under drive cycle in the load demand. The need for robust control is demonstrated in section 6.4.

An investigation on improving the hybrid system by integrating lithium-ion battery is provided in chapter 7. Extending the fuel cell hybrid design is explored in section 7.1. Advantages of combining both ultra-capacitor and lithium-ion battery are discussed. A method of estimating the state of charge of lithium-ion is presented in section 7.2. In section 7.3 a detailed development of the nonlinear control design of the SOFC, ultra-capacitor and battery hybrid system is given. Finally concluding remarks and future work are stated in the chapter 8, and references are listed. Additional information are provided in the appendices.

Chapter 2

Fuel Cell System

2.1 SOFC System

The forthcoming analysis is based on a steam reformer based tubular SOFC system. The system consists of three primary components, namely, the steam reformer, the fuel cell stack and the combustor. Methane is chosen as the fuel for the system with a molar flow rate of $\dot{N}_f$. The analysis and control approach presented in this thesis can be extended to other fuels and system configurations. The overall system is described in detail in the forthcoming sections and the diagram of the SOFC system is shown in Fig.2.1.

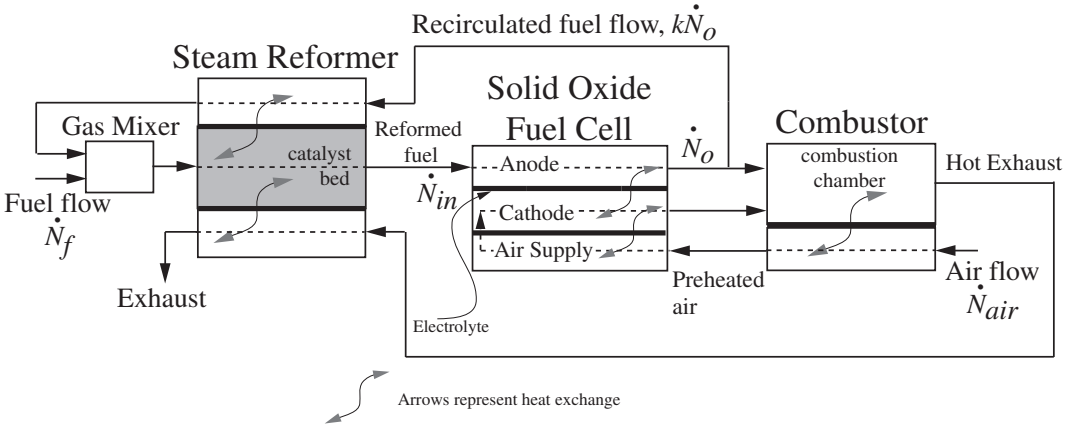

Figure 2.1: Schematic Diagram of SOFC System

The reformer produces a hydrogen-rich gas, which is supplied to the anode of the fuel cell. Electrochemical reactions occurring at the anode due to current draw results in a steam-rich gas mixture at the anode exit. A fraction k of the anode efflux is recirculated through the reformer into a mixing chamber where fuel is added. The mixing of the two fluid streams and pressurization is achieved in the gas mixer using an ejector or a recirculating fuel pump [51, 52]. The steam reforming process occurring in the reformer catalyst bed is an endothermic process. The energy required to sustain the process is supplied from two sources, namely, the combustor efflux that is passed through the reformer, and the aforementioned recirculated anode flow, as shown in Fig.2.1. The remaining anode efflux is mixed with the cathode efflux in the combustion chamber. The combustor also serves to preheat the cathode air, which has a molar flow rate of $\dot{N}_{air}$. The tubular construction of each cell causes the air to first enter the cell through the air supply tube and then reverse its direction to enter the cathode chamber. The cathode air serves as the source of oxygen for the fuel cell [53]. Detailed explanation is provided in the following sections.

2.1.1 Operation of Steam Reformer

Steam reformer configuration is shown in Fig.2.2. The fuel enters the mixer with an incoming molar flow rate of $\dot{N}_f$ and is mixed with the recirculated anode exhaust flow rich in steam. This flow then passes through the reformer catalyst where a set of endothermic reactions occur to generate a hydrogen rich gas mixture. For steam reforming of methane, a packed-bed tubular reformer with nickel-alumina catalyst is considered. Heat must be added to sustain these reactions and is done so by passing the hot exhaust and recirculated flow around the reformer. The reformate gas mixture then proceeds from the reformer to the anode of the fuel cell stack with a molar flow rate of $\dot{N}_{in}$. An exothermic electrochemical reaction occurs here based on an electrical current demand. Steam rich gas leaves the anode of the fuel cell stack at $\dot{N}_o$ mole/s and a fraction, k, of this is recirculated back to the reformer, providing necessary H_2O and heat as shown in Fig.2.1 and Fig.2.2. The recirculation is achieved by either using imperfect seals, [12], or a recirculating pump [10].

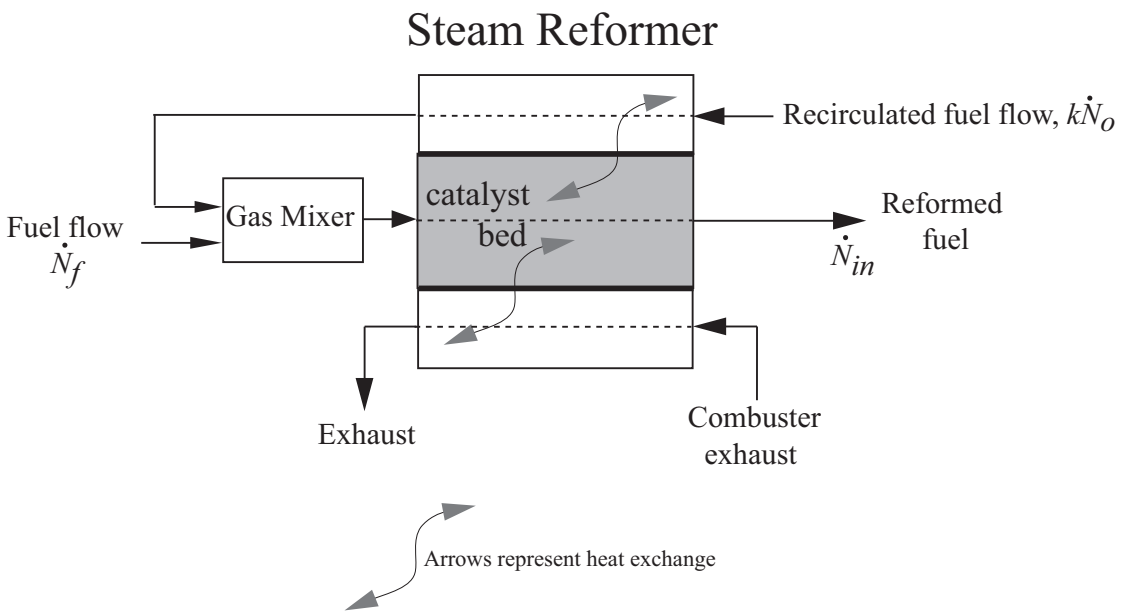

Figure 2.2: Steam Reformer Drawing

The remaining flow enters the combustion chamber with air from the cathode and is burned there. Exhaust from the combustor is sent back again to heat up the reformer.

The fuel cell system takes methane as fuel, the methane enters the steam reformer and the reaction I, II and III of the following reactions occurs [54]:

$$\begin{aligned}
&(\text{I}) && CH_4 + H_2O &&\leftrightarrow\ CO + 3H_2 \\
&(\text{II}) && CO + H_2O &&\leftrightarrow\ CO_2 + H_2 \\
&(\text{III}) && CH_4 + 2H_2O &&\leftrightarrow\ CO_2 + 4H_2 \\
&(\text{IV}) && \tfrac{1}{2}O_2 + 2e^- &&\rightarrow\ O^{2-} \\
&(\text{V}) && H_2 + O^{2-} &&\rightarrow\ 2e^- + H_2O
\end{aligned} \tag{2.1}$$

Internal reforming reactions I, II and III in Eq.(2.1) occur in the steam reformer due to high temperatures and the presence of nickel catalyst. Simultaneous electrochemical conversion of CO to CO_2 is also possible. However, this reaction is ignored since its reaction rate is much slower in presence of reactions II and V, [55].

2.1.2 Operation of Fuel Cell Stack

The SOFC stack consists of an assembly of several anode, cathode and electrolyte modules. The electrolyte is made of a thin solid ceramic material such as zirconia doped with 8 to 10 mole $\%$ yttria [11, 12]. It has high ability of conducting oxygen ions [12] at elevated temperatures. The electrolyte is placed between the anode and the cathode of the fuel cell stack as shown in Fig.2.3 and as discussed in section 1.3. It is used to only conduct oxygen ions O^{2-} resulting from the chemical reactions. Hence, the electrical conductivity must be kept as low as possible to lower the leakage-current and increase the efficiency of the fuel cell. The operating efficiency in producing electricity in SOFC is among the highest in all types of fuel cells.

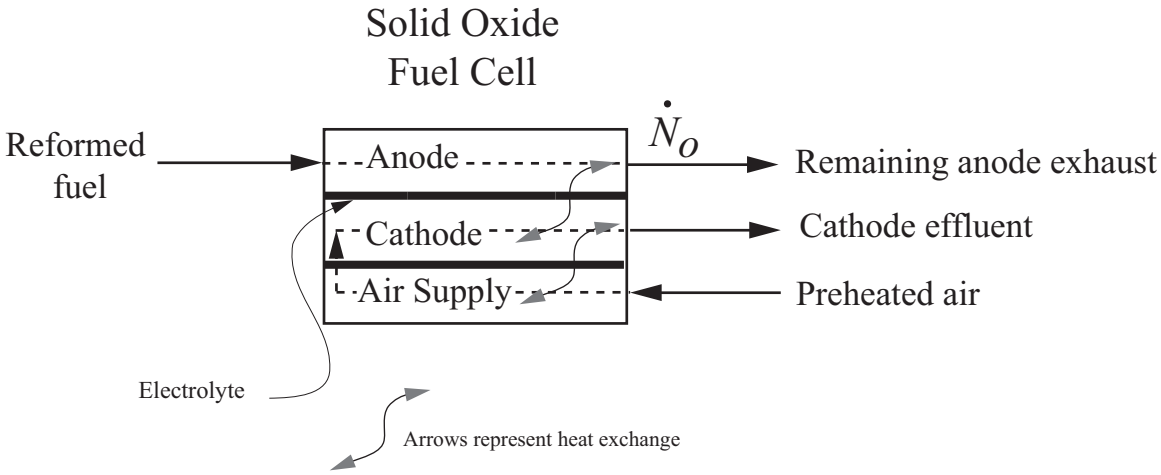

Figure 2.3: Drawing of a Solid Oxide Cell Stack

The cathode is a thin layer attached to the electrolyte where the oxygen reduction takes place. The oxygen molecules ($\frac{1}{2}O_2$) coming from air combine with electrons ($2e^-$) coming from the load to produce oxygen ions O^{2-} as shown below

$$(\text{IV}) \quad \tfrac{1}{2}O_2 + 2e^- \quad \rightarrow \quad O^{2-} \tag{2.2}$$

The oxygen ions are conducted through the impermeable electrolyte into the anode of the cell. The anode takes the oxygen ions and mix them with hydrogen pumped into it as a

fuel to produce pure water as follows

$$(\mathrm{V}) \quad H_2 + O^{2-} \quad \rightarrow \quad 2e^- + H_2O \tag{2.3}$$

The resulting electrons travel into an outside circuit to produce electric power and then travel back again to the cathode as shown in Fig.2.4.

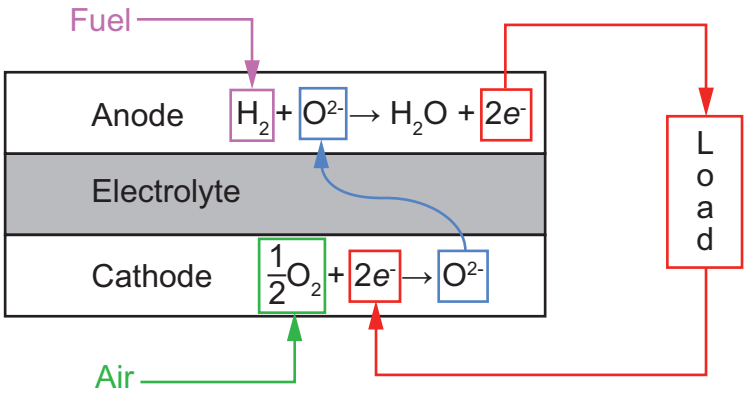

Figure 2.4: Basic Electrochemistry reactions of SOFC Stack (Figure courtesy [2])

2.1.3 Operation of Combustor

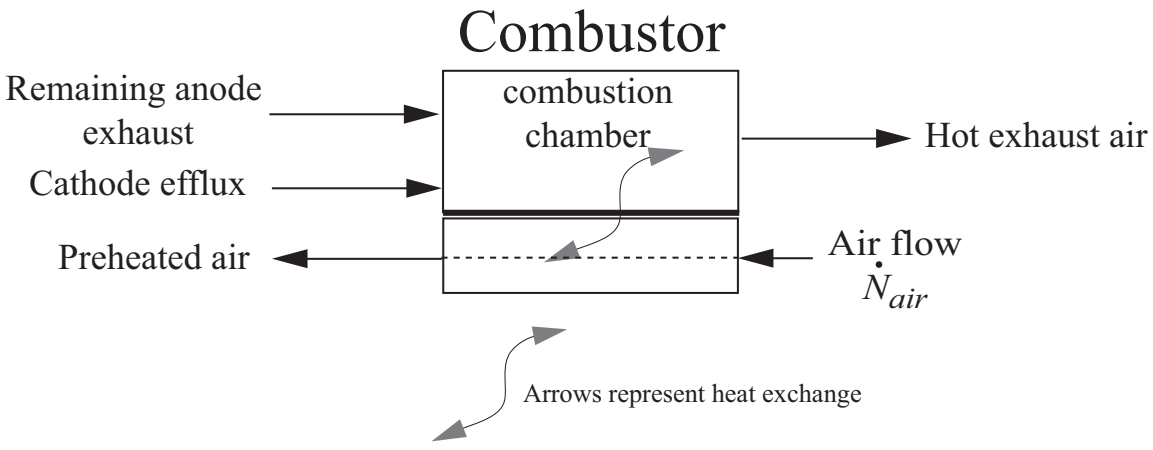

Figure 2.5: Combustor Schematic

The remaining anode exhaust of the SOFC stack is mixed with the cathode efflux in the combustion chamber as shown in Fig.2.5. In addition to burning excess fuel, the combustor also serves to preheat the cathode air which has a molar flow rate of $\dot{N}_{air}$. The air comes into the combustor at low temperatures where it is preheated and then sent to the cathode of the stack. The tubular construction of each cell causes the air to first enter the cell through the air supply tube and then reverse its direction to enter the cathode chamber Fig.2.1.

2.2 Fuel Utilization of SOFC System

The system is comprised of $\mathcal{N}_{cell}$ cells connected in series. A detailed control-oriented model of the system is developed for simulation and real-time implementation. Fuel utilization U is expressed mathematically as follows, [15, 18, 42]:

$$U = 1 - \frac{\dot{N}_o \left(4\mathcal{X}_{1,a} + \mathcal{X}_{2,a} + \mathcal{X}_{4,a}\right)}{\dot{N}_{in} \left(4\mathcal{X}_{1,r} + \mathcal{X}_{2,r} + \mathcal{X}_{4,r}\right)} \tag{2.4}$$

where, $\mathcal{X}_{1,a}$, $\mathcal{X}_{2,a}$, $\mathcal{X}_{4,a}$ and $\mathcal{X}_{1,r}$, $\mathcal{X}_{2,r}$, $\mathcal{X}_{4,r}$ are the molar concentrations of CH_4, CO and H_2 in the anode and the reformer respectively and $\dot{N}_o$ and $\dot{N}_{in}$ are shown in Fig.2.1. Eq.(2.4) is based on the observation that CH_4 can yield at most four molecules of H_2 and CO yields only to one molecule of H_2. That is indicated by reactions I, II and III in Eq.(2.1). For more mathematical details and derivations of Eq.(2.4) refer to [14].

The sensitivity of U to fuel cell current i_{fc} under uncontrolled operation is illustrated in Fig.2.6. The tubular SOFC model, with cell length of 50cm and cell area of 251cm^2, is run with $\mathcal{N}_{cell} = 50$, $\dot{N}_f = 7\times10^{-4}$moles/s and $i_{fc} = 10$A for $t < 150$s. These conditions yield a steady state utilization of $U_{ss} \approx 85\%$. Two sets of step responses are shown. The resulting U and V_{fc} are plotted in Figs.2.6(b) and (c) respectively. The following observations are made:

- Step jump of 0.5A in the fuel cell current causes a drastic fluctuation in the fuel utilization.

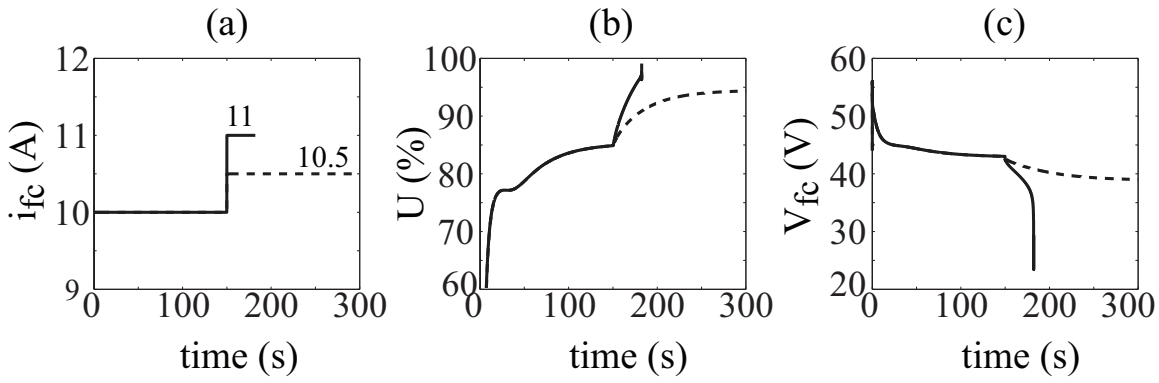

Figure 2.6: Open-Loop Response to Transient Current Demand

- Hydrogen starvation in the anode due to the transients causes a drastic voltage drop in the fuel cell voltage.
- The fuel cell system is unable to sustain a 1A increase in the fuel cell current. This is manifested as the hydrogen utilization $\rightarrow 100\%$ and the fuel cell voltage $\rightarrow$ 0V.
- The results show that under uncontrolled operation, the fuel cell is capable of responding only to very small perturbations in the power demand.

The trends are simply reversed when the step changes are applied in the negative direction. Such drastic fluctuation in U shorten the life of the fuel cell by damaging the stack. The drastic loss of voltage is undesirable in a majority of applications, where voltage must be maintained at constant level or within specific bounds. From an application point of view, the drastic fluctuations in the voltage are not acceptable unless very sophisticated power regulators are used. As discussed before, U is a common reference parameter to characterize the performance of the SOFC. It is correlated with the system efficiency. The preferred range of U is $80\% - 90\%$ [15, 16] where it gives favorable efficiency. In the next section, the fuel cell's steady-state behavior is used to develop an open-loop control of U.

2.3 Open-Loop Control of U

The molar balance equations of the species in the reformer and anode are:

$$\begin{aligned}
\dot{N}_r\mathcal{X}_{1,r} + N_r\dot{\mathcal{X}}_{1,r} &= k\dot{N}_o\mathcal{X}_{1,a} - \dot{N}_{in}\mathcal{X}_{1,r} + \mathcal{R}_{1,r} + \dot{N}_f \\
\dot{N}_r\mathcal{X}_{2,r} + N_r\dot{\mathcal{X}}_{2,r} &= k\dot{N}_o\mathcal{X}_{2,a} - \dot{N}_{in}\mathcal{X}_{2,r} + \mathcal{R}_{2,r} \\
\dot{N}_r\mathcal{X}_{3,r} + N_r\dot{\mathcal{X}}_{3,r} &= k\dot{N}_o\mathcal{X}_{3,a} - \dot{N}_{in}\mathcal{X}_{3,r} - \mathcal{R}_{1,r} - \mathcal{R}_{2,r} \\
\dot{N}_r\mathcal{X}_{4,r} + N_r\dot{\mathcal{X}}_{4,r} &= k\dot{N}_o\mathcal{X}_{4,a} - \dot{N}_{in}\mathcal{X}_{4,r} - 4\mathcal{R}_{1,r} - \mathcal{R}_{2,r} \\
\dot{N}_r\mathcal{X}_{5,r} + N_r\dot{\mathcal{X}}_{5,r} &= k\dot{N}_o\mathcal{X}_{5,a} - \dot{N}_{in}\mathcal{X}_{5,r} + 2\mathcal{R}_{1,r} + \mathcal{R}_{2,r}
\end{aligned} \tag{2.5}$$

$$\begin{aligned}
\dot{N}_a\mathcal{X}_{1,a} + N_a\dot{\mathcal{X}}_{1,a} &= \dot{N}_{in}\mathcal{X}_{1,r} - \dot{N}_o\mathcal{X}_{1,a} + \mathcal{R}_{1,a} \\
\dot{N}_a\mathcal{X}_{2,a} + N_a\dot{\mathcal{X}}_{2,a} &= \dot{N}_{in}\mathcal{X}_{2,r} - \dot{N}_o\mathcal{X}_{2,a} + \mathcal{R}_{2,a} \\
\dot{N}_a\mathcal{X}_{3,a} + N_a\dot{\mathcal{X}}_{3,a} &= \dot{N}_{in}\mathcal{X}_{3,r} - \dot{N}_o\mathcal{X}_{3,a} - \mathcal{R}_{1,a} - \mathcal{R}_{2,a} \\
\dot{N}_a\mathcal{X}_{4,a} + N_a\dot{\mathcal{X}}_{4,a} &= \dot{N}_{in}\mathcal{X}_{4,r} - \dot{N}_o\mathcal{X}_{4,a} - 4\mathcal{R}_{1,a} - \mathcal{R}_{2,a} - r_e \\
\dot{N}_a\mathcal{X}_{5,a} + N_a\dot{\mathcal{X}}_{5,a} &= \dot{N}_{in}\mathcal{X}_{5,r} - \dot{N}_o\mathcal{X}_{5,a} + 2\mathcal{R}_{1,a} + \mathcal{R}_{2,a} + r_e
\end{aligned} \tag{2.6}$$

where, r_e is the rate of electrochemical reaction given by

$$r_e = i_{fc}\mathcal{N}_{cell}/nF \tag{2.7}$$

In Eqs.(2.5), (2.6) and (2.7), $\mathcal{X}_{i,r}$ and $\mathcal{X}_{i,a}$ are the molar concentrations of species in the reformer and anode respectively, with $i = 1, 2, \cdots, 5$ representing CH_4, CO, CO_2, H_2 and H_2O in that order. N_r and N_a are the molar contents of the reformer and the anode. $\mathcal{R}_{1,r}$, $\mathcal{R}_{2,r}$ and $\mathcal{R}_{1,a}$, $\mathcal{R}_{2,a}$ are the rates of formation of CH_4 and CO in the reformer and anode respectively. i_{fc} is the fuel cell current, $n = 2$ is the number of electrons participating in an electrochemical reaction and $F = 96485.34$Coul./mole is the Faraday's constant. Further details can be found in [14]. From Eqs.(2.4), (2.5), (2.6) and (2.7), noting that the left hand sides of Eqs.(2.5) and (2.6) are zero at steady-state, the steady-state utilization U_{ss} is obtained as

$$U_{ss} = \frac{1-k}{\left(4nF\dot{N}_f/i_{fc}\mathcal{N}_{cell}\right) - k} \tag{2.8}$$

Note that Eq.(2.8) is independent of the reaction rates $\mathcal{R}_{1,r}$, $\mathcal{R}_{2,r}$, $\mathcal{R}_{1,a}$ $\mathcal{R}_{2,a}$, the flow rates $\dot{N}_{in}$, $\dot{N}_o$, temperatures and pressures and hence it represents *an invariant property* of the

fuel cell. Furthermore, since k, i_{fc} and $\dot{N}_f$ are measurable and known, Eq.(2.8) can serve as an open-loop control to achieve a target U_{ss}. Although Eq.(2.8) was derived based on the mass balance equations Eqs.(2.5) and (2.6), note that such invariant properties can be derived in a *model independent* manner with minimal system knowledge for a certain class of reformer based SOFC systems.

Consider the demanded fuel cell current to be $i_{fc,d}$. Then, from Eq.(2.8), the corresponding fuel demand $\dot{N}_{f,d}$, that satisfies a target U_{ss} is,

$$\dot{N}_{f,d} = \frac{i_{fc,d}\mathcal{N}_{cell}}{4nFU_{ss}}\left[1-(1-U_{ss})\,k\right] \tag{2.9}$$

Eq.(2.9) only addresses steady-state behavior. Hence its effectiveness must be assessed in the presence of transient current demand. Control of U using Eq.(2.9) is shown in Figs.2.7 and 2.8.

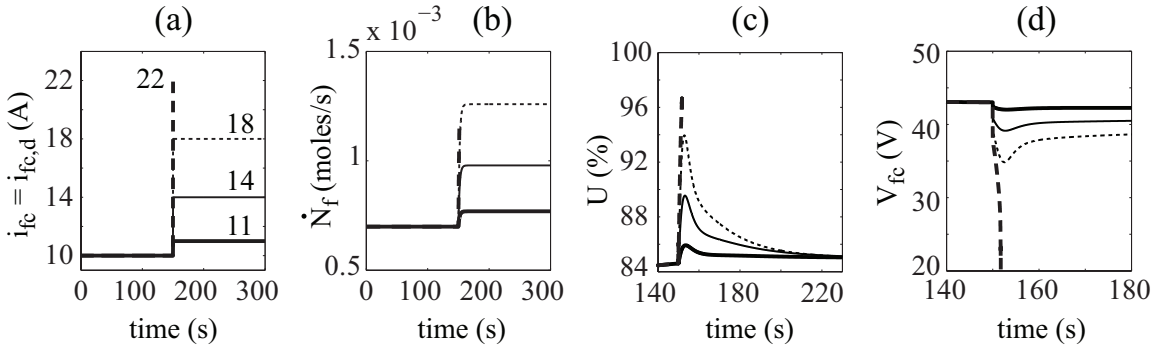

Figure 2.7: Open-Loop Control of U Using Eq.(2.9) with First Order Dynamics

The fuel cell system simulated is same as in Fig.2.6 with $i_{fc} = 10$A for $t < 150$s and target $U_{ss} = 85\%$. Four simulations are presented with $i_{fc} = 11, 14, 18, 22$A for $t \geq 150$s, Fig.2.7(a). The actual fuel injected, $\dot{N}_f$, is shown in Figs.2.7(b) and 2.8(b). Note that while $\dot{N}_{f,d}$ changes instantaneously according to Eq.(2.9), $\dot{N}_f$ experiences a lag due to the dynamics of the fuel supply system. The dynamics are assumed to be first order in Fig.2.7(b) and rate limited in Fig.2.8(b). At steady-state, $\dot{N}_f = \dot{N}_{f,d}$.

In this simulation, a first order dynamics with a time-constant of 2 seconds is assumed. However, similar response is obtained with other fuel supply dynamics, such as ramped or

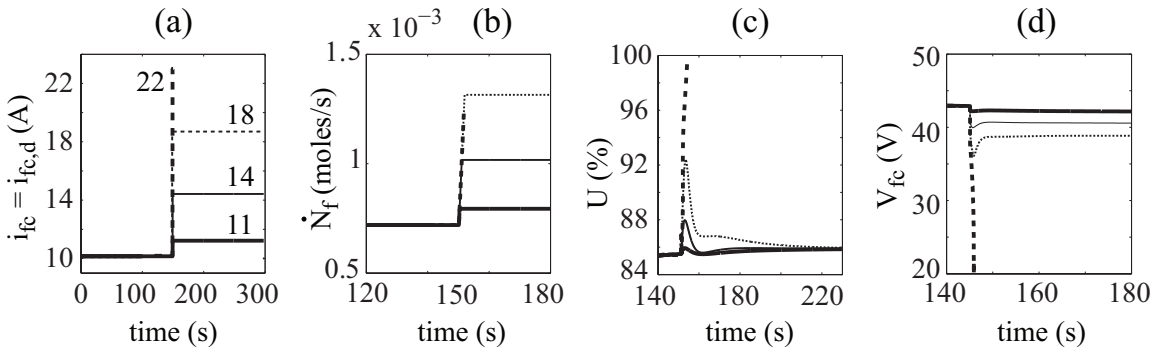

Figure 2.8: Open-Loop Control of U Using Eq.(2.9) with Rate Limited Dynamics

rate-limited behavior Fig.2.8. In Fig.2.7(c), U is plotted for individual simulations. The plots confirm $U_{ss} = 85\%$. Also, V_{fc} is plotted in Fig.2.7(d). The trends are simply reversed when negative step changes are applied.

Comparing with the uncontrolled case, under open-loop control the SOFC system is capable of handling a significantly greater amount of current fluctuation. In the uncontrolled case, the jump of 1A in the fuel cell current demand causes the utilization $U \rightarrow 100\%$ and $V_{fc} \rightarrow 0$. The open-loop controller reduces the fluctuation in U allowing bigger jumps in the fuel cell current. Less than 10% fluctuation in the utilization is observed for a jump of ≈ 8A in the current and the voltage does not drop below 35V level. The overall observation here is that the open-loop controlled case provides us with better results than the uncontrolled case.

Under the open-loop control, the utilization deviates from the target steady state utilization, U_{ss} , during transients in current as shown in Figs.2.7 and 2.8 (c). The fluctuations get bigger as the jumps in current increases. The simulation abruptly ended when the step increase was bigger than 10A. This is due to hydrogen starvation manifested by $U \rightarrow 100\%$ and correspondingly $V_{fc} \rightarrow 0$, as seen in Figs.2.7(c) and (d) for step change of 12A. Thus, the controller is not practical for bigger jumps and multiple fluctuations in the load power. A more sophisticated controller is required for more aggressive power transients.

2.4 Fuel Cell Current Regulation

The advantage of the approach in section 2.3 is that target U_{ss} is achieved without any knowledge of internal flow rates, temperatures, species concentrations or reaction rates. No sensor devices are needed for this control strategy. However, transients produces fluctuations in U and drops in fuel cell voltage because this strategy is based on steady-state behavior. Hence improving its effectiveness must be considered in the presence of transient current demand. A close-loop controller is proposed in this section to increase the performance of the fuel cell during transients. The overshoots and the undershoots in the fuel cell voltage are addressed in this approach. The fluctuations in the utilization need to be reduced to ensure that the SOFC can handle bigger transients in power.

The strategy uses feedback to dynamically shape the current draw from the fuel cell system. Noting that $\dot{N}_f \neq \dot{N}_{f,d}$ during transients, due to delays in the fuel supply system. These delays are described in the forthcoming discussion. The fuel cell current i_{fc} is shaped using Eq.(2.8), as follows:

$$i_{fc} = \frac{4nFU_{ss}\dot{N}_f}{\mathcal{N}_{cell}} \frac{1}{[1-(1-U_{ss})\,k]} \tag{2.10}$$

Implementing Eq.(2.10) requires the measurement of the actual fuel flow $\dot{N}_f$, which is assumed to be available. The feedback based current regulation scheme and the open-loop approach are shown in Fig.2.9 by the switch positions CL and OL respectively. Simulations are presented in Fig.2.10 to demonstrate the effect of current regulation on transient utilization and voltage.

The fuel cell current demand $i_{fc,d}$ is determined directly based on the current demand from the load i_L. The fuel flow rate demand $\dot{N}_{f,d}$ is also determined based on the fuel cell current demand $i_{fc,d}$ according to Eq.(2.9). However, the theoretically calculated fuel flow rate demand $\dot{N}_{f,d}$ is different than the actual fuel flow rate $\dot{N}_f$ obtained at the output of the fuel supply system during transients as indicated in Fig.2.9. $\dot{N}_f$ has delays caused by the fuel supply system. Having the ability to measure the delayed fuel flow rate or the

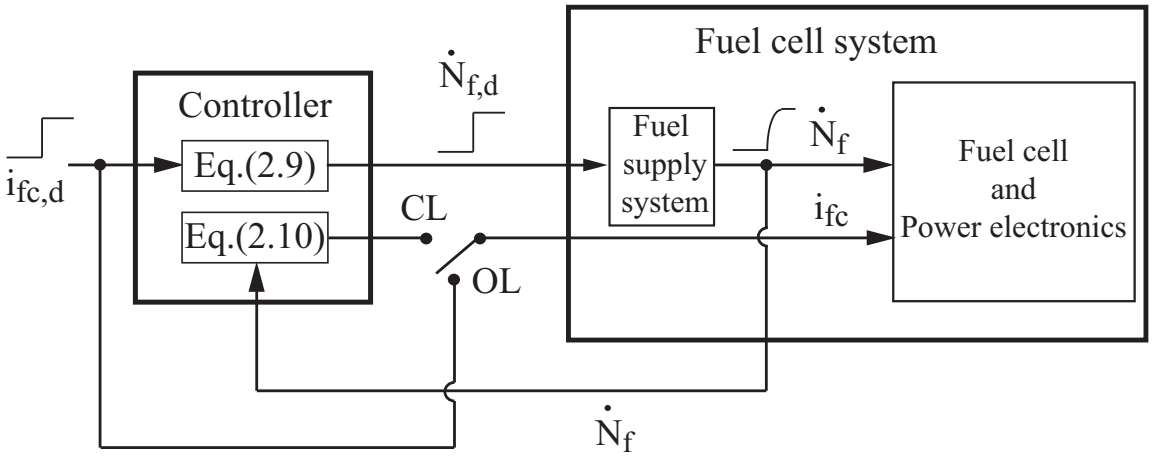

Figure 2.9: Scheme for Transient Utilization Control

actual fuel flow rate at the output of the fuel supply system and using Eq.(2.10), the target current can be estimated. By drawing this calculated current, the SOFC attenuates transient fluctuation in U and improves the voltage response.

The system simulated is the same manner as in Figs.2.6 and 2.7 in section 2.2 and section 2.3 respectively. In the feedback-based control approach, referring to Fig.2.9, the simulation results represent the closed-loop (CL) mode. Three different simulations are conducted to prove the validity of this control strategy under transients. The target $U_{ss} = 85\%$ and an initial current draw of 10A are used. After the first 150s, three different step changes in the current draw are applied. The first jump is from 10A to 18A. The second step is from 10 to 30A. Lastly, a jump of 40A from 10A is applied. These instantaneous jumps in the current demand are used to prove the validity of this approach under drastic transients.

The experimental results are shown in Figs.2.10 and 2.11 for first order and rate limited dynamics of the fuel supply system respectively. Since the same results are obtained for both dynamics thus we refer only to Fig.2.10 in the following discussion. In response to the step changes in $i_{fc,d}$, the target fuel $\dot{N}_{f,d}$ also undergoes step changes, Figs.2.10 (a) and (b) respectively. $\dot{N}_f$ changes according to the fuel supply dynamics which is assumed

to be first order with a time constant of 2 sec, Fig.2.10(b), as in the previous simulations. Measured $\dot{N}_f$ is assumed to be available and the shaped i_{fc} is computed using Eq.(2.10) and is shown in Fig.2.10(a). The resulting transient U and V_{fc} are shown in Figs.2.10(c) and (d) respectively.

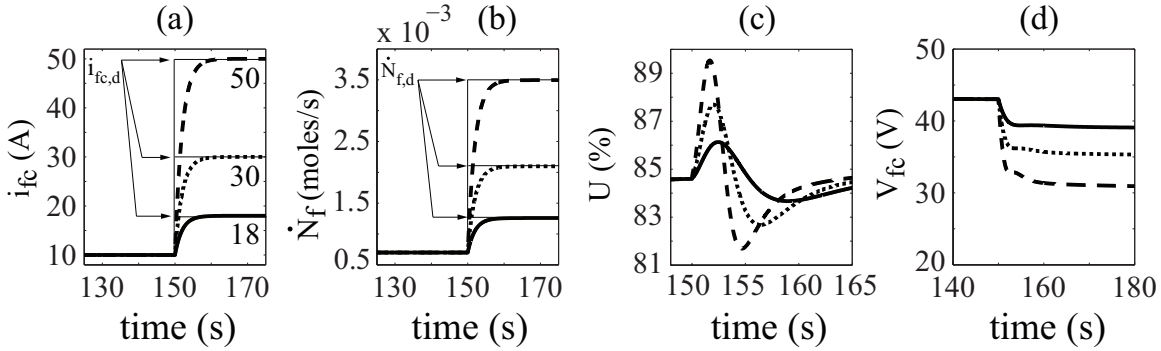

Figure 2.10: Effect of i_{fc} Regulation on Transient U and V_{fc} with First Order Dynamics

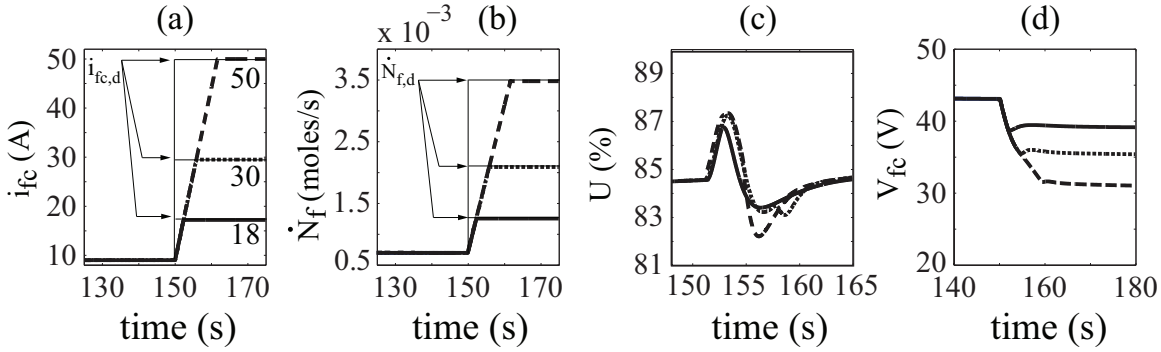

Figure 2.11: Effect of i_{fc} Regulation on Transient U and V_{fc} with Rate Limit Dynamics

It is evident from the results above that the feedback based regulation of i_{fc} drastically reduces transient U. It also improves transient response of V_{fc}. For instance, the step change to $i_{fc,d} = 18$A led to a deviation in U from 85% to $\approx 94\%$ in the open-loop mode Fig.2.7(c), whereas only a jump from 85% to $\approx 86\%$ is observed in closed-loop mode Fig.2.10(c). Note here that while the transient U is considerably attenuated, it is not

completely eliminated. In the next section, we present a detailed discussion of its causes.

Current regulation also increases the transient current handling capability of the fuel cell by a considerable margin. Even with a step change to $i_{fc,d} = 50$A which is 40A jump in the current demand, transient U remains within a $\pm 5\%$ range. The fuel cell utilization is well regulated under this control strategy and only small fluctuations are observed. That keeps the efficiency of the fuel cell at optimum levels, which is desired in a majority of applications. In addition to the reduction in the U, the voltage transients are considerably reduced. Much bigger jumps in the current demands are applied, but lower transients in the voltages are observed in Fig.2.10(d). From application point of view, this improvement in voltage transients allows simple voltage regulator to be used.

This current regulation approach requires only one additional sensor, namely a flow rate sensor that measures $\dot{N}_f$, which is assumed to be available in the SOFC. The sensor is placed upstream of the reformer of the SOFC system as shown in Fig.2.12. This is because downstream of the reformer the methane is already decomposed as explained in section 2.1.1 and shown in reforming reactions I, II, and III in Eq.(2.1).

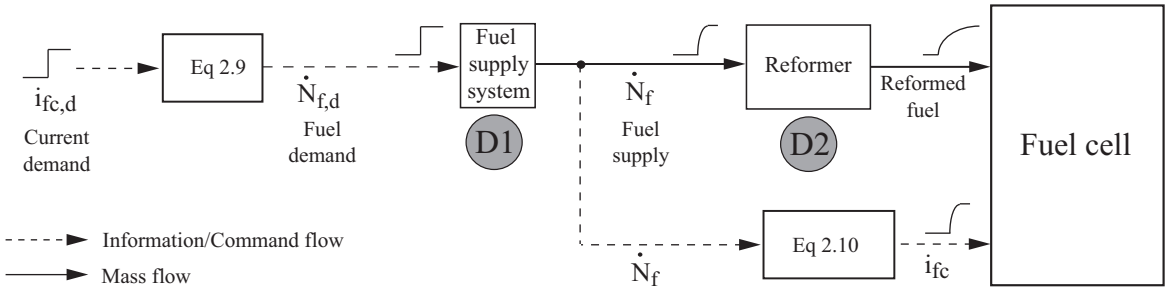

Figure 2.12: Flow Rate Sensor Arrangement

The outcomes of this strategy are encouraging, the fluctuations in the fuel cell utilization are reduced drastically and voltage transients are significantly improved. However, it is evident that during transients i_{fc} is dynamically shaped to reduce fluctuations in U from the target value. This will lead to a mismatch between the demanded power and fuel cell delivered power as evident in Fig.2.10(a). This is a fitting scenario to consider a hybrid

fuel cell system with a supplementary power source such as a battery or a ultra-capacitor. Thus during transient operation, while the proposed control strategy ensures that the fuel utilization undergoes minimal deviation from U_{ss}, the power deficit or surplus will be managed by discharging or charging the supplementary energy storage element. This will be discussed in details in the forthcoming sections.

2.5 Delays Induced along Fuel Path

At the end of section 2.3, we observed that the transient deviation of U from target U_{ss} is due to delays induced along the fuel path shown in Fig.2.12. This delay is attributed to two primary factors,

D1: The lag between $\dot{N}_{f,d}$ and $\dot{N}_f$ introduced by dynamics of the fuel supply system

D2: The delay introduced by the dynamics of the fuel processor (reformer).

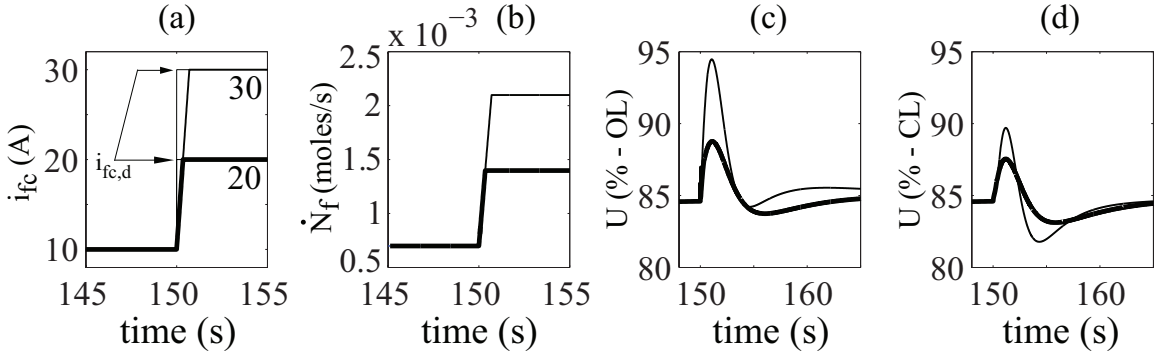

Figure 2.13: Open and Closed-Loop Responses for Ramped $\dot{N}_f$

Current regulation in section 2.4 compensates for D1, Eq.(2.10), Fig.2.9. The residual transient in U shown in Fig.2.10 (c) is attributed to D2. In sections 2.3 and 2.4, a first order and ramped response dynamics in the fuel supply system are assumed. However, the observations made are applicable to a wide variety of dynamic responses. As another

example, a different ramped response of the fuel supply systems is considered in Fig.2.13. For $t < 150$s, the fuel cell current is kept constant at $i_{fc} = 10$A. For $t \geq 150$s, two simulations are shown, with $i_{fc,d} = 20$ and 30A. $\dot{N}_f$ ramps at a rate of 0.002moles/s in response to change in $i_{fc,d}$, Fig.2.13(b). As shown in Fig.2.13(a), $i_{fc} = i_{fc,d}$ in OL and is ramped in CL. U in OL and CL configurations are shown in Figs.2.13(c) and (d) respectively. As before, significant deviation in U is observed in OL mode that is considerably attenuated in CL mode.

To explore the effect of D1 in the current feedback regulation approach, the previous experiments are conducted again, however step changes in i_{fc} and different delays in D1 are assumed. As the delay D1 becomes smaller, the effect of input shaping diminishes. This trend is shown in Fig.2.14 where for $t < 150$s, $i_{fc} = 10$A and $i_{fc,d} = 15$A for $t \geq 150$s. Three simulations are shown, all with first order fuel-supply dynamics and time-constants chosen as 0.5s, 2s and 6s. It is clear from Fig.2.14 that greater the delay D1, greater is the

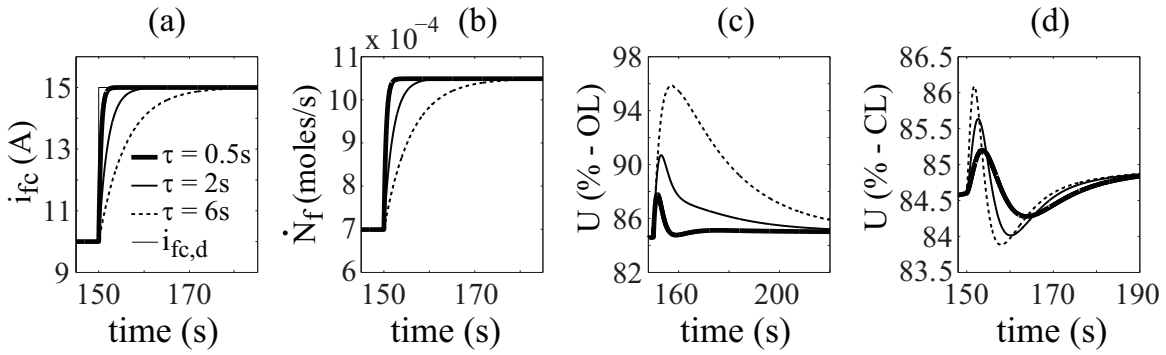

Figure 2.14: Effect of D1 on Transient U in OL and CL Modes

degradation of the transient response of U, and greater is the effect of current regulation. If the fuel supply system responds instantaneously, then current regulation is inconsequential.

For perfect disturbance rejection, i_{fc} must be further regulated, based on the reformer dynamics, to compensate for delay D2. Achieving this using a model-independent approach is a topic of future research. It is observed that the effect of D1 is more pronounced

than D2 in a majority of cases. However, the effect of D2 is magnified when the reformer's void volume is much larger compared to the anode volume or when there exists severe flow restriction between the reformer and the anode. The later effect is demonstrated in Fig.2.15, where the corresponding friction factor is increased by a factor of 100 in the model. As shown in Fig.2.15, in the presence of heightened flow restriction, the transient deviation in U is not as well attenuated as in the default case.

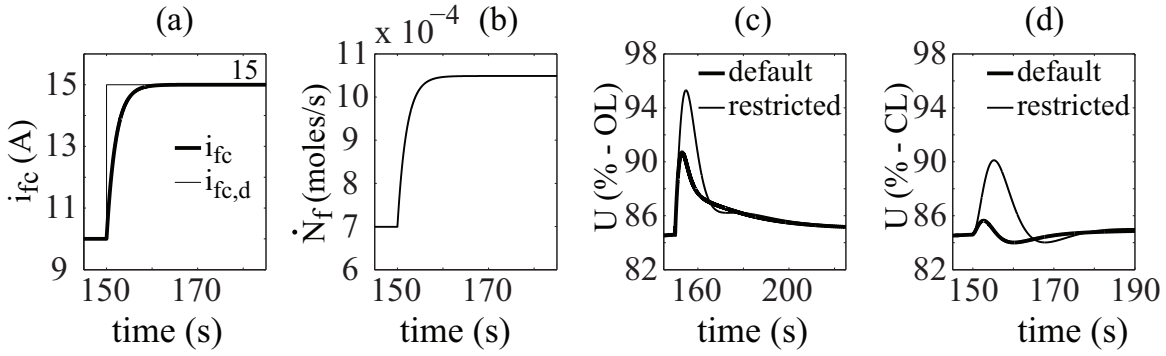

Figure 2.15: Effect of D2 on Transient U in OL and CL Modes

Chapter 3

Hybrid Fuel Cell Configuration

In the previous chapter, the fuel cell current shaping approach is proposed to reduce drastic fluctuations in U. This approach consequently reduces the transients in cell voltage. The simulation results obtained by the application of this control strategy are very encouraging. However, regulating the fuel cell current to satisfy these two constraints leads to a mismatch between the demanded power from the load and the power supplied by the fuel cell. Hybridizing the SOFC with an energy storage element is proposed to compensate for this mismatch.

In the hybrid system, when the fuel cell delivers lower than the demanded power, the storage element must supply the deficit. Similarly, when the fuel cell power is greater than the power demand, the excess power will absorbed and charge up the storage element. Hence, a power split control algorithm must be designed to maintain the State-Of-Charge (SOC) of the auxiliary storage element. The aforementioned storage device can be a battery, or an ultra-capacitor, or both at the same time and that depends on the type of the application and the nature of the load. Batteries have high energy density compared to ultra-capacitor. Ultra-capacitors have very high power density (> 1000W/Kg) and are medium energy density ($1 - 10$Wh/Kg) devices, as indicated in Fig.3.1 [3, 56]. Detailed discussions about these storage devices are provided in the following sections.

3.1 Batteries

The basic operation of batteries is based on chemical reactions. Fundamentally, when chemical reactions occur, there is a consequent release or absorption of energy. The release and the absorption of energy mostly appears in heat (exothermic and endothermic reactions), however in certain materials it appears as electric energy (electrochemical reaction). Accordingly, batteries are electrochemical devices that can store energy and deliver power to the load [56].

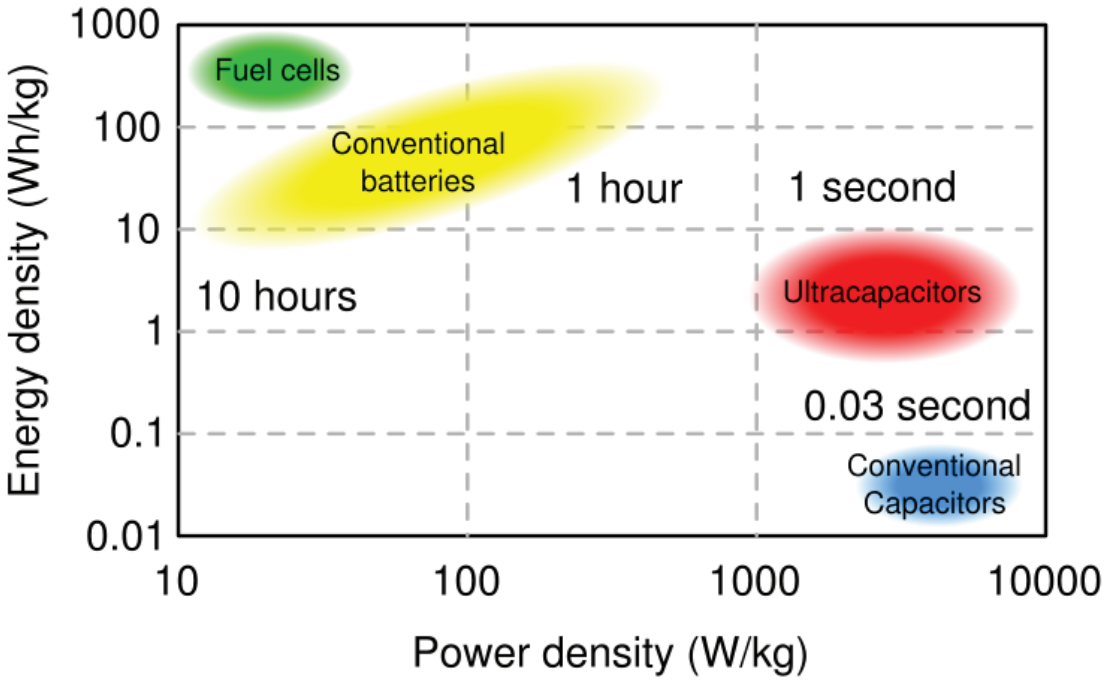

Figure 3.1: Energy and Power Density of Different Power Storage Devices (Figure courtesy [3])

Usually, batteries are composed of cells that are connected in parallel or series. The performance of the battery cell depends on its electrical characteristics and physical properties. Batteries are characterized with high energy density as shown in Fig.3.1. Energy

density is a measure of the amount of energy stored compared to the weight of the battery. It is expressed in Watt-hours/Kg. Volumetric energy density is also another parameter used to characterize the battery. It is a standard of comparison between the stored energy in a battery and its volume. Among the recent battery technologies, lithium-ion battery has the highest energy density and volumetric energy density. It can store more than 100 Watt-hour/kg [56, 57].

Several types of batteries exist, such as lead-acid and lithium-ion batteries. Lead-acid is one of the traditional types. They are attractive in many applications, especially in automotive systems. They have advantages of sustaining high voltage per cell and supplying big surge in current. Nevertheless, they are relatively heavy and have slow recovery time [56]. In the recent years, lithium-ion technology has dominated the field of advanced power systems and replaced many other battery technologies in the market. Different types of lithium-ion batteries use different materials and concepts.

The basic components are a cathode, an anode and a thin electrolyte. During the discharge process, lithium ions from the anode transfer into the cathode. During the charging process, exactly the inverse process occurs, involving extraction of ions from the cathode to the anode, [58]. Cathode materials include lithium-metal oxides, vanadium oxides or olivines. Anode materials are lithium, graphite, lithium-alloys, inter-metallics, or silicon [57]. The light weight of these materials and the high energy to volume ratio give lithium-ion battery technology superiority over other types of batteries. However, they have poor cycle life. For every charge and discharge, the internal resistance increases slightly and adversely affects the cell's ability to deliver power [57]. This is the main draw back of lithium-ion batteries.

3.2 Ultra-capacitors

The concept of the ultra-capacitors is different from the known conventional capacitors. A conventional capacitor stores energy by removing electrons from the positive plate and

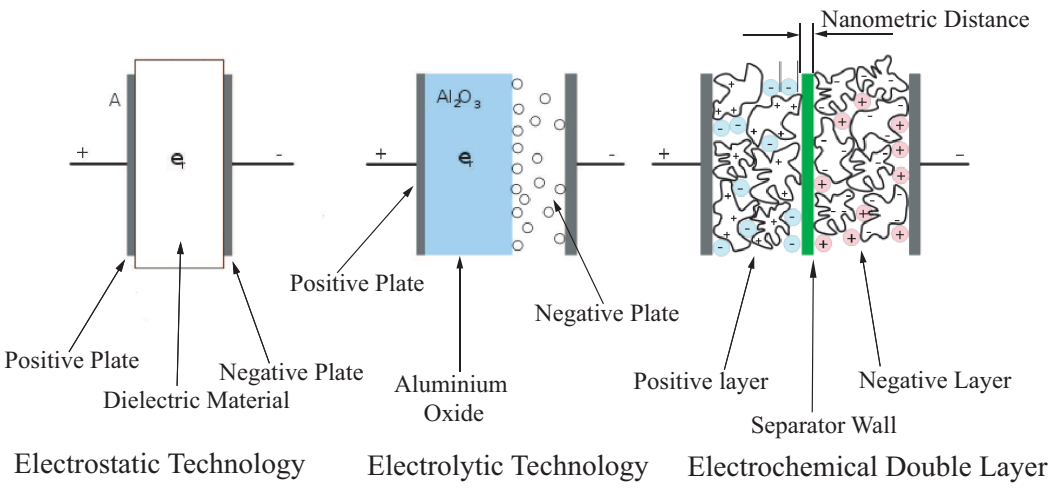

Figure 3.2: Capacitor and Ultra-capacitor Structure (Figure courtesy [3])

storing them in the negative plate [3]. These plates are usually separated by dielectric materials that consume space and increase weight. Instead of having dielectric material between plates, ultra-capacitors have one plate with two layers separated by an ultra-thin (nanometer sized) wall. They are called electrical double layer as shown in Fig.3.2.

Although the separator wall is very thin, but it provides very effective separation of charge. This allows the plates to have much larger surface area in a smaller size. Each plate can store significant amount of energy. This structure provides the ultra-capacitor with extraordinarily high capacitance (ranging up to 2000 Farads). The layers themselves are very conductive, they can release instantaneously very high amount of energy. No chemical reaction is involved in its energy storage mechanism and hence ultra-capacitors have long charging/discharging life cycle.

The only drawback of this technology is that they cannot operate at high voltages. To operate in high voltages, multiple cells need to be connected in series. Also, ultra-capacitors store smaller amount of energy than batteries [3].

3.3 Hybrid SOFC Ultra-capacitor Configuration Design

Based on the discussion above, choosing the right device as an auxiliary storage element plays a very important role in designing the hybrid system. In this thesis, SOFC ultra-capacitor hybrid system is proposed and an investigation on combining both lithium-ion battery and ultra-capacitor is conducted in chapter 7. In the following sections, control

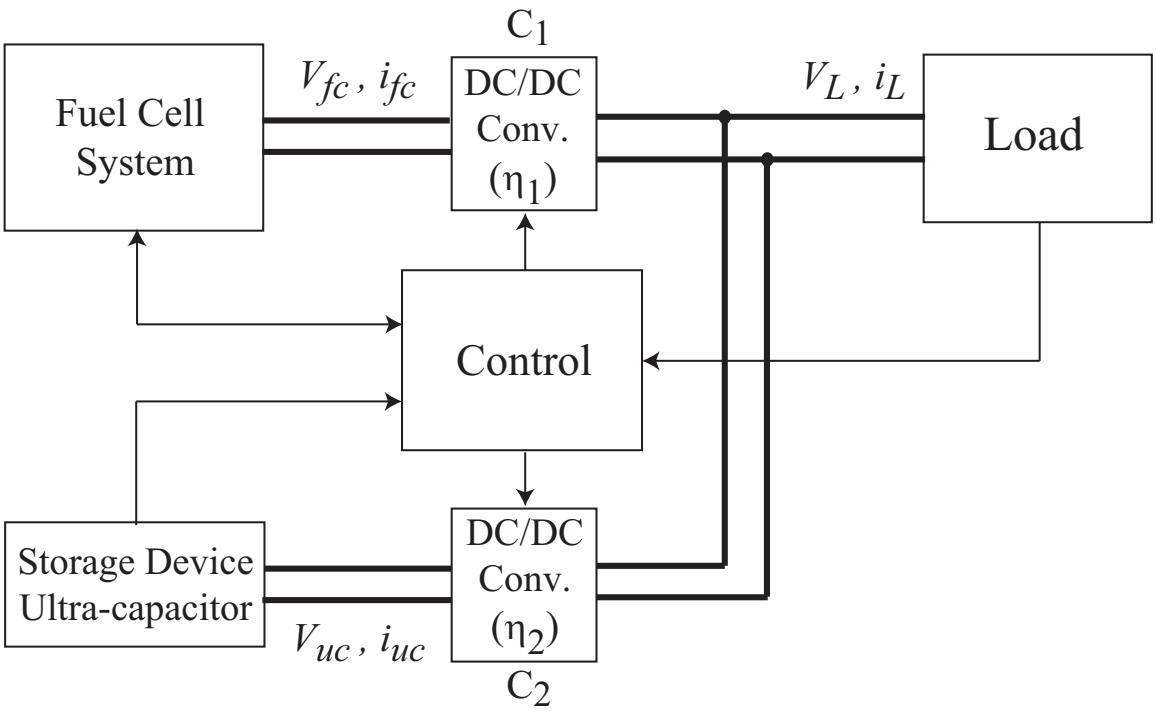

Figure 3.3: Hybrid Fuel Cell System

strategies with combined objectives of achieving load following while controlling U and the ultra-capacitor's SOC at their respective target values are developed. The fuel cell and the ultra-capacitor are connected to the electrical bus through DC/DC converters, C_1 and C_2, as shown in Fig.3.3. The architecture used in this thesis is similar to that adopted in [31]. Alternate approaches for interfacing fuel cell and ultra-capacitor/battery are discussed in [27, 29, 59] and references therein. In the control development, the DC/DC converters are treated as static power conversion devices. From Fig.3.3, the instantaneous power balance

equation is obtained as follows

$$V_L i_L = \eta_1 V_{fc} i_{fc} + \eta_2 V_{uc} i_{uc} \tag{3.1}$$

The following aspects are considered in the control development:

- We operate the SOFC in constant utilization mode, section 2.4. Hence the fuel cell voltage is expected to change with power draw because of the voltage-current characteristic of fuel cell. Therefore, a DC to DC converter is required to regulate the output voltage to a fixed value.

- The bus (supply) voltage V_L is held constant. This can be implemented by operating C_1 in voltage control mode and C_2 in the current control mode or vice-versa. Without any loss of generality, we follow the former combination with C_2 following the commanded ultra-capacitor current $i_{uc,c}$ (we treat $i_{uc} = i_{uc,c}$) and C_1 as fuel cell voltage regulator.

- The ultra-capacitor current i_{uc} and the fuel demand $\dot{N}_{f,d}$ are treated as control inputs. The ultra-capacitor current is commanded in both directions using the bi-directional DC to DC converter C_2. The $\dot{N}_{f,d}$ is determined from the demanded fuel cell current using Eq.(2.9).

- Measurement of the ultra-capacitor voltage is necessary for the controller to calculate the ultra-capacitor's SOC.

- Measurements of V_{fc}, V_{uc}, i_L, i_{fc} and $\dot{N}_f$ are available. Current sensors are required to measure i_L and i_{fc}.

- The DC/DC converter efficiencies η_1 and η_2 vary with operating conditions and are treated as unknowns with constant estimates $\bar{\eta}_1$ and $\bar{\eta}_2$, where $\bar{\eta}_1, \bar{\eta}_2 > 0$.

Chapter 4

Control Design

4.1 Control Objectives and Approaches

Based on the discussion on the prior sections, the control objectives are:

1. to minimize the fluctuation in the fuel cell utilization, consequently reduces dropping in fuel cell voltage,

2. maintain the SOC of the ultra-capacitor at desired level, and

3. the proposed control strategies are required to be robust to specific uncertainties of the system.

Two control strategies are proposed in this section, a Lyapunov-based nonlinear control and a standard H_∞ robust control. Note that , H_∞ is very standard approach and requires precise knowledge of the hybrid system.

4.2 Nonlinear Control

The schematic diagram shown in Fig.4.1 represents a nonlinear control strategy for the hybrid system consisting of SOFC and ultra-capacitor. The strategy incorporates the fuel cell system discussed in section 2.4 and an ultra-capacitor discussed in section 3.2. The fuel cell serves as the primary energy source of the hybrid system. The ultra-capacitor is

considered as secondary power source that helps the fuel cell to handle transients in power demands while preventing drastic fluctuation in fuel utilization.

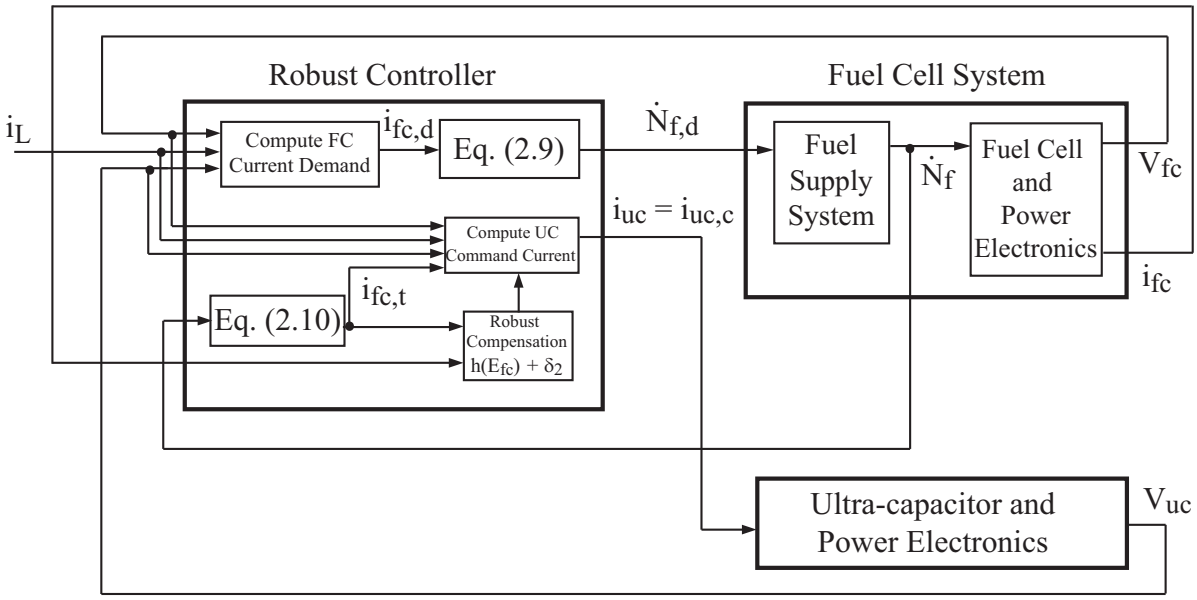

Figure 4.1: Nonlinear Control Approach

Based on Eq.(2.9), the demanded the fuel flow $\dot{N}_{f,d}$ is an algebraic function of fuel cell current demand, $i_{fc,d}$. As shown in Fig.3.3, if the fuel cell is the only energy source in the system and the efficiency η_1 is completely known, then the control problem will be much simpler and the demanded fuel cell current will be

$$i_{fc,d} = \frac{V_L i_L}{\eta_1 V_{fc}}$$

However, this is an idealistic scenario of the SOFC system. Based on the discussion in the section 2.4, the fuel cell current, i_{fc} is shaped to avoid drastic fluctuations in the utilization Eq.(2.10). Also as discussed in chapter 2 and 3, the current shaping introduces a mismatch between the demanded power and the delivered power from the fuel cell during transients. This mismatch is compensated by the ultra-capacitor, leading to SOC variation.

Moreover, the efficiencies of the power converters are unknown. They are only estimated based on imprecise knowledge of the system and the power converters. Thus, η_1 is uncertain and the SOC of the ultra-capacitor should be kept at the desired level. The fuel cell current demand above is redesigned to address these constraints as follows

$$i_{fc,d} = \frac{V_L i_L}{\bar{\eta}_1 V_{fc}} + g(E_s) + \delta_1, \tag{4.1}$$

The robustness in η_1 is handled by adding a constant term δ_1. This constant will be designed in the ensuing analysis. Controlling the ultra-capacitor SOC to avoid undercharge/overcharge states is handled by a function $g(E_s)$. This function depends on the error E_s which is the difference between the measured SOC (S) and the target SOC (S_t), expressed as follows

$$E_s = S - S_t \tag{4.2}$$

The $g(E_s)$ function simply regulates $i_{fc,d}$ to compensate for E_s.

The target SOC, S_t is set to 80% to ensure that there is energy buffer in the ultra-capacitor and there is enough room to absorb extra power from the grid during transients. The measured S is obtained by measuring the ultra-capacitor voltage and using the following

$$S = \frac{V_{uc}}{V_{max}} \tag{4.3}$$

where V_{max} is the maximum ultra-capacitor voltage.

To avoid drastic fluctuations of the utilization, the obtained measured fuel from the fuel supply system, $\dot{N}_f$ is used to find the fuel cell target current as shown in Fig.4.1, and is computed using Eq.(2.10), expressed as follow

$$i_{fc,t} = \frac{4nFU_{ss}\dot{N}_f}{\mathcal{N}_{cell}} \frac{1}{[1-(1-U_{ss})\,k]} \tag{4.4}$$

Due to the delays in the fuel supply system, it is evident that $i_{fc,t} \neq i_{fc,d}$. Consequently, mismatch in power occurs between the demanded power and the supplied power from the fuel cell. This mismatch is compensated by the the ultra-capacitor as follows

$$i_{uc} = \frac{V_L i_L - \eta_1 V_{fc} i_{fc,t}}{\eta_2 V_{uc}} \tag{4.5}$$

However, as mentioned before, the efficiencies in both the power converters η_1 and η_2 are unknown because they change with operating conditions. Efficiencies are treated as uncertain parameters in the control design. Hence in the control designs, estimated efficiencies are used. An additional robustness term δ_2 is added to the above expression to compensate for uncertainties in the hybrid system. The actual fuel cell current is also affected by the these uncertainties, making $i_{fc} \neq i_{fc,t}$, where i_{fc} is the actual fuel cell current. Thus, the ultra-capacitor current is designed as follows

$$i_{uc} = \frac{V_L i_L - \bar{\eta}_1 V_{fc} i_{fc,t}}{\bar{\eta}_2 V_{uc}} + h\left(E_{fc}\right) + \delta_2, \tag{4.6}$$

where E_{fc} is the error produced between the actual (measured) and the target fuel cell current and expressed as follows

$$E_{fc} = i_{fc} - i_{fc,t}, \tag{4.7}$$

The function $h\left(E_{fc}\right)$ and the robustness term δ_2 will be developed further in the ensuing analysis.

Our control objectives are to stabilize the origin $E_s = E_{fc} = 0$ in the presence of fluctuating i_L with the designs of $i_{fc,d}$ and i_{uc} in Eqs.(4.1) and (4.6) respectively. In addition, the dynamics of the fuel supply system introduces a transient error between $i_{fc,d}$ and $i_{fc,t}$ given by

$$E_{fc,t} = i_{fc,t} - i_{fc,d}, \tag{4.8}$$

The dynamics of $E_{fc,t}$ is a characteristic of the fuel supply system, which are considered unknown in the design.

Note that the feedback based current regulation approach detailed in section 2.4 is designed to compensate for D1 , where D1 represents the lag between the rate of change in the fuel demand, $\dot{N}_{f,d}$, and the rate of change in the actual fuel, $\dot{N}_f$, introduced by dynamics of the fuel supply system. While the dynamics of the fuel supply system is considered

unknown, it is evident from the results of section 2.5 that the fuel supply system, and specifically the error variable $E_{fl} = \dot{N}_f - \dot{N}_{f,d}$, satisfies a general stability property. With this observation, we state and prove the following theorems:

Theorem 1 *If the origin of E_{fl} is exponentially stable, then the hybrid SOFC system in Fig.3.3, with the control approach in Fig.4.1, satisfies exponential stability of the origin of $\mathcal{E} = [E_s \; E_{fc,t} \; E_{fc}]^T$, $E_{fc,t}$ as in Eq.(4.8), with $i_{fc,d}$ and i_{uc} as in Eqs.(4.1) and (4.6) respectively , also $g(E_s)$ is designed to be*

$$g(E_s) = -k_s \, E_s, \quad k_s > 0, \tag{4.9}$$

$h(E_{fc})$ is

$$h(E_{fc}) = k_p E_{fc} + k_d \dot{E}_{fc}, \quad k_p, k_d > 0, \tag{4.10}$$

δ_1 and δ_2 are chosen to satisfy

$$\delta_1 \begin{cases} \leq & (V_L i_L / \eta_1 V_{fc}) \, (1 - \eta_1 / \bar{\eta}_1) \quad \textit{for} \quad E_s > 0 \\ \geq & (V_L i_L / \eta_1 V_{fc}) \, (1 - \eta_1 / \bar{\eta}_1) \quad \textit{for} \quad E_s \leq 0 \end{cases} \tag{4.11}$$

$$\delta_2 \begin{cases} \geq & \beta \quad \textit{for} \quad E_{fc} > 0 \\ \leq & \beta \quad \textit{for} \quad E_{fc} \leq 0 \end{cases}, \tag{4.12}$$

where,

$$\beta = \frac{1}{\eta_2 V_{uc}} \left[V_L i_L \left(1 - \frac{\eta_2}{\bar{\eta}_2} \right) - \eta_1 V_{fc} i_{fc} \left\{ 1 - \frac{\bar{\eta}_1}{\eta_1} \frac{\eta_2}{\bar{\eta}_2} \right\} \right] \tag{4.13}$$

Proving of the above theorem is long and involved many parts of the hybrid system. Thus we though it is convenient to start with a summary. The following prove is organized as follows

- From the exponential stability of E_{fl} and the relationship $E_{fc,t} = \sigma E_{fl} \Rightarrow E_{fc,t}$ is exponential stable

- Using *Converse Lyapunov Theorems*, there exist a positive definite function $\bar{V}_{fc}$ with $\dot{\bar{V}}_{fc} \leq 0$

- The Lyapunov function candidate for the hybrid system is

$$\bar{V} = \frac{1}{2}\left(E_s^2 + E_{fc}^2\right) + \bar{V}_{fc}$$

- Prove along the system trajectories and the designed δ_1, δ_2, and β that

$$\dot{\bar{V}} = \frac{\partial \bar{V}}{\partial t} + \frac{\partial \bar{V}}{\partial \mathcal{E}}\dot{\mathcal{E}} = E_s\dot{E}_s + E_{fc}\dot{E}_{fc} + \dot{\bar{V}}_{fc} < 0$$

  That is by finding expressions for $E_s\dot{E}_s$ and $E_{fc}\dot{E}_{fc}$

Proof: Exponential stability of E_{fl} implies [60]

$$|E_{fl}(t)| \leq \gamma\,|E_{fl}(0)|\; e^{-\alpha t}, \quad \gamma, \alpha > 0, \quad \forall\, t > 0 \tag{4.14}$$

Note that, E_{fl} is

$$E_{fl} = \dot{N}_f - \dot{N}_{f,d} \tag{4.15}$$

and γ and α are unknown but their upper and lower bounds respectively exist and can be estimated. From Eqs.(2.9) and (4.4), it is evident that

$$E_{fc,t} = \sigma E_{fl}, \quad \sigma = \frac{4\eta F U_{ss}}{N_{cell}} \frac{1}{[1-(1-U_{ss})k]} > 0 \tag{4.16}$$

Eqs.(4.14) and (4.16) implies

$$|E_{fc,t}(t)| \leq \gamma\,|E_{fc,t}(0)|\; e^{-\alpha t}, \tag{4.17}$$

From Eq.(4.17) and *Converse Lyapunov Theorems* [60, 61], because $E_{fc,t}$ has an exponentially stable behavior, there exists a positive definite function $\bar{V}_{fc}$ such that,

$$\alpha_1 E_{fc,t}^2 \leq \bar{V}_{fc}(E_{fc,t}) \leq \alpha_2 E_{fc,t}^2, \quad 0 < \alpha_1 < \alpha_2 \quad \text{and} \quad \dot{\bar{V}}_{fc} \leq -\alpha_3 E_{fc,t}^2, \quad \alpha_3 > 0 \tag{4.18}$$

We use the following Lyapunov function candidate

$$\bar{V} = \frac{1}{2}\left(E_s^2 + E_{fc}^2\right) + \bar{V}_{fc} \tag{4.19}$$

Consequently

$$\dot{\bar{V}} = \frac{\partial \bar{V}}{\partial t} + \frac{\partial \bar{V}}{\partial \mathcal{E}}\dot{\mathcal{E}} = E_s\dot{E}_s + E_{fc}\dot{E}_{fc} + \dot{\bar{V}}_{fc} \tag{4.20}$$

where $\dot{\bar{V}}_{fc}$ is negative definite according to Eq.(4.18).

Based on Eq.(4.2)

$$\dot{E}_s = \dot{S} \tag{4.21}$$

From Eq.(4.3),

$$\dot{S} = \frac{\dot{V}_{uc}}{V_{max}} \tag{4.22}$$

because V_{max} is constant. Substituting for $\dot{S}$ from Eq.(4.22) into Eq.(4.21),

$$\dot{E}_s = \frac{\dot{V}_{uc}}{V_{max}} \tag{4.23}$$

From the dynamical equation of the ultra-capacitor, $\dot{V}_{uc}$ can be expressed as

$$\dot{V}_{uc} = -\frac{i_{uc}}{C} \tag{4.24}$$

which implies

$$\dot{E}_s = -\frac{i_{uc}}{CV_{max}} \tag{4.25}$$

From the power balance relationship in Eq.(3.1) and Eq.4.25, the following is obtained

$$\dot{E}_s = -\frac{1}{CV_{max}}[\frac{V_L i_L - \eta_1 V_{fc} i_{fc}}{\eta_2 V_{uc}}] \tag{4.26}$$

From Eqs.(4.7) and (4.8), i_{fc} can be expressed in terms of the errors in E_{fc} and $E_{fc,t}$ as follows

$$E_{fc} = i_{fc} - i_{fc,t},\ E_{fc,t} = i_{fc,t} - i_{fc,d} \ \Rightarrow\ i_{fc} = E_{fc} + E_{fc,t} + i_{fc,d}$$

Substituting the above expression of i_{fc} into Eq.(4.26),

$$\dot{E}_s \;=\; (-1/CV_{max})\left[(V_L i_L/\eta_2 V_{uc}) - (\eta_1 V_{fc}/\eta_2 V_{uc})\left(E_{fc} + E_{fc,t} + i_{fc,d}\right)\right] \tag{4.27}$$

Substituting for $i_{fc,d}$ as designed in Eq.(4.1), the following is obtained

$$\begin{aligned}\dot{E}_s = [\quad & (-1/CV_{max}) \\ & [(V_L i_L/\eta_2 V_{uc}) - (\eta_1 V_{fc}/\eta_2 V_{uc})\left\{E_{fc} + E_{fc,t}\left(V_L i_L/\bar{\eta}_1 V_{fc}\right) + g(E_s) + \delta_1\right\}] \quad]\end{aligned} \tag{4.28}$$

Replacing $g(E_s)$ by its designed expression as in Eq.(4.9)

$$\begin{aligned}\dot{E}_s = [\quad & (-1/CV_{max}) \\ & [(V_L i_L/\eta_2 V_{uc}) - (\eta_1 V_{fc}/\eta_2 V_{uc})\left\{E_{fc} + E_{fc,t} + (V_L i_L/\bar{\eta}_1 V_{fc}) - k_s E_s + \delta_1\right\}] \quad]\end{aligned} \tag{4.29}$$

Finally, the expression of $E_s\dot{E}_s$ is

$$\begin{aligned}E_s\dot{E}_s = [\quad & (-E_s/CV_{max}) \\ & [(V_L i_L/\eta_2 V_{uc}) - (\eta_1 V_{fc}/\eta_2 V_{uc})\left\{E_{fc} + E_{fc,t} + (V_L i_L/\bar{\eta}_1 V_{fc}) - k_s E_s + \delta_1\right\}] \quad]\end{aligned} \tag{4.30}$$

Next, the expression for $\dot{E}_{fc}E_{fc}$ is driven to complete the proof. Note from Eq.(3.1) that

$$V_L i_L = \eta_1 V_{fc} i_{fc} + \eta_2 V_{uc} i_{uc}$$

and from Eq.(4.6)

$$i_{uc} = \frac{1}{\bar{\eta}_2 V_{uc}}(V_L i_L - \bar{\eta}_1 V_{fc} i_{fc,t}) + h\left(E_{fc}\right) + \delta_2$$

Substituting i_{uc} from Eq.(4.6) into Eq.(3.1) gives

$$V_L i_L = \eta_1 V_{fc} i_{fc} + \eta_2 V_{uc}\left[\frac{V_L i_L - \bar{\eta}_1 V_{fc} i_{fc,t}}{\bar{\eta}_2 V_{uc}} + h(E_{fc}) + \delta_2\right] \tag{4.31}$$

From Eq.(4.10), substituting the designed expression of $h(E_{fc})$, the following is obtained

$$V_L i_L = \eta_1 V_{fc} i_{fc} + \eta_2 V_{uc} \left[\frac{V_L i_L - \bar{\eta}_1 V_{fc} i_{fc,t}}{\bar{\eta}_2 V_{uc}} + k_p E_{fc} + k_d \dot{E}_{fc} + \delta_2 \right] \tag{4.32}$$

Solving Eq.(4.32) for $\dot{E}_{fc}$,

$$\begin{aligned} \dot{E}_{fc} = [\quad & - \left[k_p/k_d + \left(V_{fc}/k_d V_{uc} \right) \left(\bar{\eta}_1/\bar{\eta}_2 \right) \right] E_{fc} + \\ & \frac{1}{k_d \eta_2 V_{uc}} \left[V_L i_L \left(1 - \frac{\eta_2}{\bar{\eta}_2} \right) - \eta_1 V_{fc} i_{fc} \left\{ 1 - \frac{\bar{\eta}_1}{\eta_1} \frac{\eta_2}{\bar{\eta}_2} \right\} \right] - \frac{1}{k_d \delta_2} \quad] \end{aligned} \tag{4.33}$$

Rearranging Eq.(4.33)

$$\dot{E}_{fc} = -\alpha E_{fc} + \frac{\beta - \delta_2}{k_d} \tag{4.34}$$

where, β is given in Eq.(4.13) and α is given by

$$\alpha = \left[k_p/k_d + \left(V_{fc}/k_d V_{uc} \right) \left(\bar{\eta}_1/\bar{\eta}_2 \right) \right]$$

Note that constants k_p and k_d are positive values in the design $h(E_{fc})$. The fuel cell voltage V_{fc} and the ultra-capacitor voltage V_{uc} are always positive. The estimated efficiencies of the power converters $\bar{\eta}_1$ and $\bar{\eta}_2$ are also positive and their values are between 0 and 1. Thus

$$\alpha = \left[k_p/k_d + \left(V_{fc}/k_d V_{uc} \right) \left(\bar{\eta}_1/\bar{\eta}_2 \right) \right] > 0 \tag{4.35}$$

Then

$$E_{fc} \dot{E}_{fc} = -E_{fc} (\alpha E_{fc} + \frac{\beta - \delta_2}{k_d}) \tag{4.36}$$

All the terms in the first derivative of the Lyapunov's function in (4.20) are evaluated. From Eqs. (4.18), (4.30) and (4.36) the Equation (4.20) can be rewritten as

$$\dot{\bar{V}} \leq -\mathcal{E}^T Q \mathcal{E} + \frac{E_s}{C V_{max} \eta_2 V_{uc}} \left[\eta_1 V_{fc} \delta_1 - V_L i_L \left(1 - \frac{\eta_1}{\bar{\eta}_1} \right) \right] + \frac{E_{fc}}{k_d} \left(\beta - \delta_2 \right) \tag{4.37}$$

where,

$$\mathcal{E} = \begin{bmatrix} E_s \\ E_{fc,t} \\ E_{fc} \end{bmatrix}, \quad Q = m \begin{bmatrix} k_s & -0.5 & -0.5 \\ -0.5 & \alpha_3/m & 0 \\ -0.5 & 0 & \alpha/m \end{bmatrix}, \quad m = \frac{\eta_1 V_{fc}}{C V_{max} \eta_2 V_{uc}} \tag{4.38}$$

Note that the conditions in Eqs.(4.11) and (4.12) are implementable since E_s, E_{fc}, and all voltage and current variables in $(V_L i_L/\eta_1 V_{fc})\,(1-\eta_1/\bar{\eta}_1)$ and β are measurable. Although the efficiencies η_1 and η_2 are not known, their upper and lower bounds can be estimated. These guarantee that

$$\frac{E_s}{CV_{max}\eta_2 V_{uc}}\left[\eta_1 V_{fc}\delta_1 - V_L i_L\left(1-\frac{\eta_1}{\bar{\eta}_1}\right)\right] + \frac{E_{fc}}{k_d}\left(\beta-\delta_2\right) \leq 0$$

Moreover, in Eq.(4.38) that Q is symmetric. Furthermore, $m>0$ and has finite positive upper and lower bounds over the range of operation of the hybrid system. Among the positive constants k_s, α and α_3, note that α_3 is not a tunable parameter since it is determined by the dynamics of the fuel supply system. However, by choosing k_s and α appropriately, $Q>0$ can be ensured for all feasible values of m. Thus from the *Rayleigh-Ritz Inequality* [62],

$$\mathcal{E}^T Q \mathcal{E} \geq \inf\left(\lambda_{min,Q}\right)||\mathcal{E}||^2 > 0 \quad \forall\, \mathcal{E}\neq 0 \tag{4.39}$$

where $\lambda_{min,Q}$ represents the smallest eigenvalue of Q at any instant. Furthermore note that by choosing δ_1 and δ_2 to satisfy Eqs.(4.11) and (4.12), we have from Eqs.(4.37) and (4.39)

$$\dot{V} \leq -\mathcal{E}^T Q \mathcal{E} \leq -\inf\left(\lambda_{min,Q}\right)||\mathcal{E}||^2 < 0, \quad \forall\, \mathcal{E}\neq 0 \tag{4.40}$$

From Eqs.(4.14), (4.19) and (4.40), we conclude that the control design in Eqs.(4.1) and (4.6), with functions $g(E_s)$, $h(E_{fc})$, δ_1, and δ_2 designed as in Eq.(4.9), Eq.(4.10), Eqs.(4.11) and (4.12) respectively, guarantee *exponential stability* of $\mathcal{E}=0$. This completes the proof. $\Diamond\Diamond\Diamond$

Now, let relax the exponential stability of E_{fl} in the following theorem:

Theorem 2 *If the origin of E_{fl} is Input-to-State Stable, ISS [60], then the hybrid SOFC system in Fig.3.3, with the control approach in Fig.4.1, satisfies ISS property of the origin of $\bar{\mathcal{E}} = [E_s\ E_{fc}]^T$, with $i_{fc,d}$ and i_{uc} designed as in Eqs.(4.1), (4.6), (4.9), (4.11) and (4.12).*

Proof: ISS property of E_{fl} implies

$$|E_{fl}(t)| \leq f_{\mathcal{KL}}\left(|E_{fl}(t_0)|, t-t_0\right) + \gamma_{\mathcal{K}}\left(\sup_{t_0\leq\tau\leq t}||u(\tau)||\right), \quad \forall\, t\geq t_0 \tag{4.41}$$

where $f_{\mathcal{KL}}$ and $\gamma_{\mathcal{K}}$ are class $\mathcal{KL}$ and class $\mathcal{K}$ functions respectively. The definitions of class $\mathcal{K}$, $\mathcal{L}$, and $\mathcal{KL}$ functions are given as:

- Definition 01: A continuous function α : [0, a) $\rightarrow$ [0, ∞) is said to be belong to class $\mathcal{K}$ if it is strictly increasing and α(0) = 0. It is said to be belong to class $\mathcal{K}_\infty$ if a = ∞ and α(r) $\rightarrow \infty$

- Definition 02: A continuous function γ : [0, ∞) $\rightarrow$ [0, ∞) is said to be of class $\mathcal{L}$ if it monotonically decreasing and γ(s) = 0 as s $\rightarrow \infty$

- Definition 03: A class $\mathcal{KL}$ function is class $\mathcal{K}$ with respect to the first argument and class $\mathcal{L}$ with respect to the second argument

From Eqs.(2.9) and (4.4), it is evident that Eq.(4.41) implies $E_{fc,t}$ is ISS, i.e.

$$|E_{fc,t}(t)| \leq f_{\mathcal{KL}}\left(|E_{fc,t}(t_0)|, t-t_0\right) + \bar{\gamma}_{\mathcal{K}}\left(\sup_{t_0\leq\tau\leq t}||u(\tau)||\right), \quad \forall\, t \geq t_0 \tag{4.42}$$

where $\bar{\gamma}_{\mathcal{K}} = \gamma_{\mathcal{K}}\mathcal{N}_{cell}\left[1-(1-U_{ss})k\right]/4nFU_{ss}$. In the state equations of E_s and E_{fc}, given in Eqs.(4.27) and (4.33), note that $E_{fc,t}$ can be considered as an input. Using the Lyapunov function candidate

$$\bar{V} = \left(E_s^2 + E_{fc}^2\right)/2 \tag{4.43}$$

we have

$$\dot{\bar{V}} \leq -\bar{\mathcal{E}}^T\bar{Q}\bar{\mathcal{E}} + \frac{E_s}{CV_{max}\eta_2 V_{uc}}\left[\eta_1 V_{fc}(\delta_1 + E_{fc,t}) - V_L i_L\left(1-\frac{\eta_1}{\bar{\eta}_1}\right)\right] + \frac{E_{fc}}{k_d}\left(\beta-\delta_2\right) \tag{4.44}$$

where,

$$\bar{Q} = m\begin{bmatrix} k_s & -0.5 \\ -0.5 & \alpha/m \end{bmatrix}, \quad m = \frac{\eta_1 V_{fc}}{CV_{max}\eta_2 V_{uc}}$$

By choosing k_s and α appropriately, $\bar{Q} > 0$ can be ensured for all feasible m. Furthermore,

by choosing δ_1 and δ_2 to satisfy Eqs.(4.11) and (4.12) respectively, we have from Eq.(4.44),

$$\begin{aligned}
\dot{\bar{V}} &\leq -\bar{\mathcal{E}}^T\bar{Q}\bar{\mathcal{E}} + (\eta_1 V_{fc}/CV_{max}\eta_2 V_{uc})E_s E_{fc,t} \\
&\leq -\inf\left(\lambda_{min,\bar{Q}}\right)||\bar{\mathcal{E}}||^2 + (\eta_1 V_{fc}/CV_{max}\eta_2 V_{uc})||\bar{\mathcal{E}}||\,|E_{fc,t}(t)| \\
&\leq -\inf\left(\lambda_{min,\bar{Q}}\right)(1-\theta)||\bar{\mathcal{E}}||^2, \quad 0<\theta<1 \\
&< 0, \quad \forall \quad ||\bar{\mathcal{E}}|| \geq \eta_1 V_{fc}/\left[CV_{max}\eta_2 V_{uc}\,\theta\,\inf\left(\lambda_{min,\bar{Q}}\right)\right]|E_{fc,t}(t)|
\end{aligned} \tag{4.45}$$

From Eqs.(4.43), and (4.45), we infer that the control design in Eqs.(4.1) and (4.6), with functions $g(E_s)$, $h(E_{fc})$, δ_1, and δ_2 designed as in Eq.(4.9), Eq.(4.10), Eqs.(4.11), and (4.12) respectively , guarantee that $\bar{\mathcal{E}} = 0$ is ISS. This completes the proof.

$\Diamond\Diamond\Diamond$

The ultimate bounds on $\bar{\mathcal{E}}$ will depend on the ultimate bound on $E_{fc,t}$. Hence, the more accurately the fuel supply system tracks $\dot{N}_{f,d}$, the lower will be the bound on $||\bar{\mathcal{E}}||$. ISS is less restrictive than exponential and asymptotic stability since Eq.(4.41) requires that the origin of the unforced system (with $u(t) \equiv 0$) be *uniformly asymptotically stable* only. For example, for a first order response of the fuel supply system,

$$\dot{N}_f(s)/\dot{N}_{f,d}(s) = 1/\left[(1/a)s+1\right], \quad a>0 \quad \Rightarrow \quad \dot{E}_{fl} = -aE_{fl} - \ddot{N}_{f,d}$$

Assuming exponential stability of E_{fl} implies neglecting $\ddot{N}_{f,d}$ and ISS property implies modeling $\ddot{N}_{f,d}$ as input u. The latter is more realistic and it is reasonable to assume $\ddot{N}_{f,d}$ to be bounded with upper and lower bounds.

4.3 H_∞ Control

This section presents an alternate control design incorporating a standard H_∞ base approach. While the nonlinear control discussed in section 4.2 leads to custom designed algorithms that address system uncertainties, we also explore the application of standard robust control techniques for this application. The advantage of standard methods lies in the availability of computational tools for controller synthesis. Specifically, we show that the simplicity of the ultra-capacitor's dynamic model, Eq.(4.24), allows the design of an H_∞ control for SOC regulation.

Signal based approach is used to design the controller because it is very appropriate for problems in which several objectives must be taken into account simultaneously. In this approach, the plant and all possible model uncertainties need to be defined. Also, all inputs, outputs and reference signal of the system need to be well defined and weights should be assigned as shown in Fig.4.2. The weights are used to capture the expected frequency content of the exogenous signals and the desired frequency content of the error signals [63].

Referring to Fig.4.1 and Eq.(4.1), the only difference introduced by the H_∞ approach compared to the nonlinear control in section 4.2 is that $i_{fc,d}$ is computed as

$$i_{fc,d} = V_L i_L / \bar{\eta}_1 V_{fc} + \delta_{i_{fc}} \tag{4.46}$$

where, $\delta_{i_{fc}}$ will be designed in the forthcoming analysis. A state space representation of the system is needed to perform the H_∞ control synthesis where all uncertainties and disturbances are included. From Eqs.(3.1) and (4.24),

$$\dot{V}_{uc} = [V_L i_L - \eta_1 V_{fc} i_{fc}] / C V_{uc} \eta_2 \tag{4.47}$$

Expressing i_{fc} as

$$i_{fc} = i_{fc,d} + \sigma \tag{4.48}$$

where σ represents a bounded unknown error term, from Eqs.(4.46), (4.47) and (4.48), the following is obtained

$$\dot{V}_{uc} = \frac{1}{C V_{uc} \eta_2} \left[V_L i_L \left(1 - \frac{\eta_1}{\bar{\eta}_1} \right) - V_{fc} \eta_1 (\delta_{i_{fc}} + \sigma) \right] \tag{4.49}$$

Eq.(4.49) can be expressed as

$$\dot{V}_{uc} = f - p(\delta_{i_{fc}} + \sigma), \quad f = V_L i_L \left(1 - \frac{\eta_1}{\bar{\eta}_1} \right) / C V_{uc} \eta_2, \quad p = V_{fc} \eta_1 / C V_{uc} \eta_2 \tag{4.50}$$

Design $\delta_{i_{fc}}$ as follows,

$$\delta_{i_{fc}} = \frac{1}{\hat{p}} \left(\hat{f} - v \right) \quad \Rightarrow \quad i_{fc,d} = \frac{V_L i_L}{\bar{\eta}_1 V_{fc}} + \frac{1}{\hat{p}} \left(\hat{f} - v \right) \tag{4.51}$$

where $\hat{f}$ and $\hat{p}$ are the estimates of the functions f and p respectively, evaluated with nominal values. In the H_∞ control design, we evaluate the maximum bounds of deviation by evaluating f and p with maximum upper and minimum lower bounds possible for all uncertain and variable quantities. Substituting for $\delta_{i_{fc}}$ from Eq.(4.51) into Eq.(4.50), we get

$$\dot{V}_{uc} = \frac{p}{\hat{p}} v + \left[f - \frac{p}{\hat{p}} \hat{f} - p\sigma \right] \tag{4.52}$$

Representing $p/\hat{p}$ as a nominal value β_0 plus maximum deviation $\Delta\beta_0$, and assigning the rest of Eq.(4.52) as disturbances d, we have

$$\dot{V}_{uc} = (\beta_0 + \Delta\beta) v + d \tag{4.53}$$

where the modified control input v is computed using the dynamic feedback law. Now, it is evident that finding the maximum bounds of the uncertainties and the deviation from the nominal values is just a matter of numerical calculation based on knowledge of the hardware set up of the system, such as the efficiencies of the DC to DC converters, nominal voltage of the ultra-capacitor, and the bus voltage. Disturbances can also be predicted using knowledge of the sensor (measurement) noise and the accumulated signal delays, which become so important during fast transients.

After defining all these parameters, the H_∞ problem simplifies to finding the controller K_∞ that stabilizes the norm of the input/output transfer function of the system. The controller required to make the system robust to deviation from nominal values of the parameters of the hybrid system. The Matlab® Robust Toolbox is used to find the optimum controller K_∞ that satisfies the necessary following equation

$$\delta_{i_{fc}} = K_\infty(s)\,(-e(s)), \quad e(t) = V_{uc,t} - V_{uc} \tag{4.54}$$

where K_∞ is controller transfer function obtained using standard H_∞ synthesis, and $V_{uc,t} = S_t\, V_{max}$ is the target ultra-capacitor voltage.

Fig.4.2 shows the H_∞ setup. In the H_∞ synthesis, weights are chosen such that $(A,\, B_2,\, Z_2)$ is stable, $(A,\, Z_2)$ is detectable and D_{12} and D_{21} are full rank matrices. The inputs are weighted to satisfy *the small gain theorem of stability*. The outputs are weighted such that

the sensitivity is lower at lower frequencies and high at higher frequencies [63]. The H_∞ synthesis is carried out using the Robust Toolbox. This approach is an effective alternate

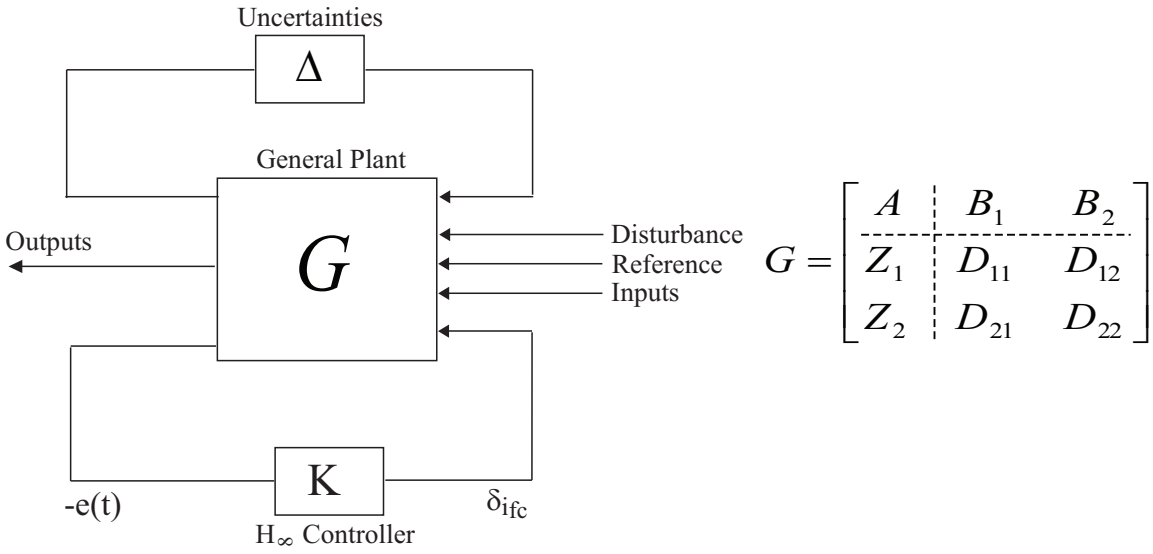

Figure 4.2: H_∞ Classical Setup

control synthesis method.

Remark 1 *Throughout the control design, C_1 and C_2 are assumed to operate in voltage and current control modes respectively. If the combination is reversed, $E_{fc} = 0$, i.e. $i_{fc} = i_{fc,t}$, and current control of the ultra-capacitor and hence Eq.(4.6) are irrelevant. Referring to Theorems 1 and 2, the exponential and ISS property of the origin of E_{fl} would still imply exponential and ISS property respectively of $E_s = 0$ with $i_{fc,d}$, E_s and δ_1 designed as in Eqs.(4.1), (4.9) and (4.11). The H_∞ control design would remain unchanged.*

Finally, note that although stack temperature control is important, it is not considered in the control development. This is because stack temperature transients are considerably slower (order of tens of minutes) compared to transient U (order of tens of seconds) [64], [18]. Also, in absence of coolants, SOFC stack temperature is typically controlled separately by manipulating the cathode air.

Chapter 5

Experimental Test-Stand

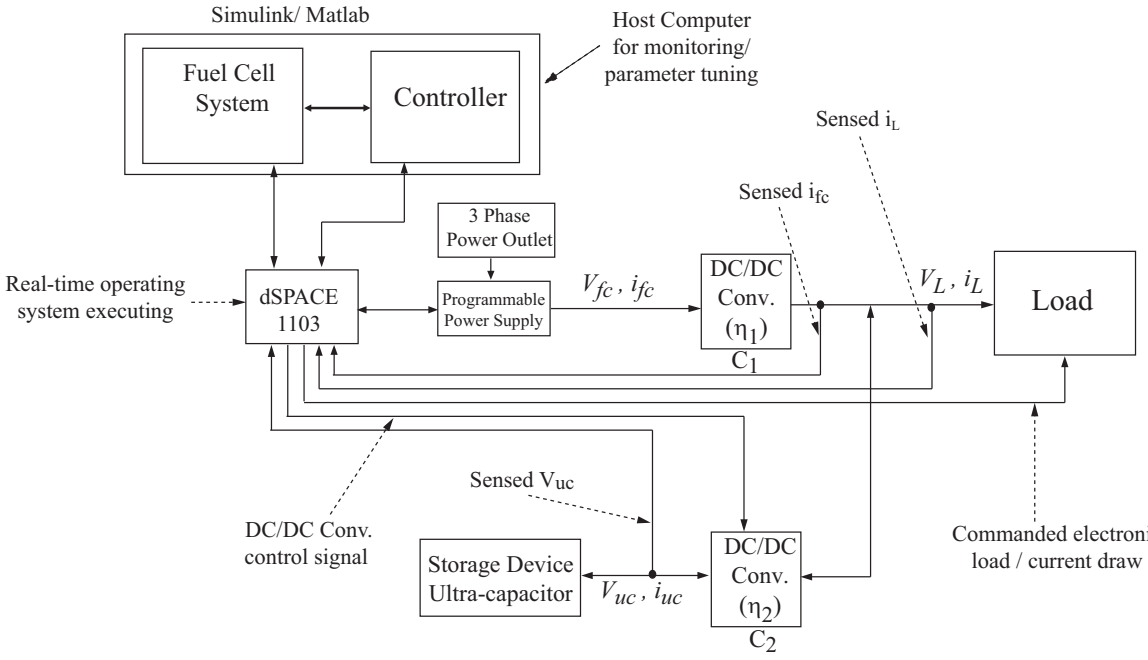

Figure 5.1: Fuel Cell Emulator within Hybrid Energy System Schematic

The control strategies developed in sections 4.2 and 4.3 are tested on an experimental test-stand, shown in Figs.5.1 and 5.2 which implements the hybrid system schematically depicted in Fig.3.3. The test-stand consists of the fuel cell model and ultra-capacitor bank connected in parallel through power electronics devices C_1 and C_2 Fig.5.1. C_1 and C_2 are

DC/DC converters. C_2 controls the power draw from the ultra-capacitor bank and C_2 regulates the bus voltage. The bus voltage refers to the voltage V_L in Fig.5.1. A programmable electronic load is used to draw power from the hybrid system. The overall hybrid system is designed to operate at nominal power of 1KW. The following sections describe the hybrid system in details.

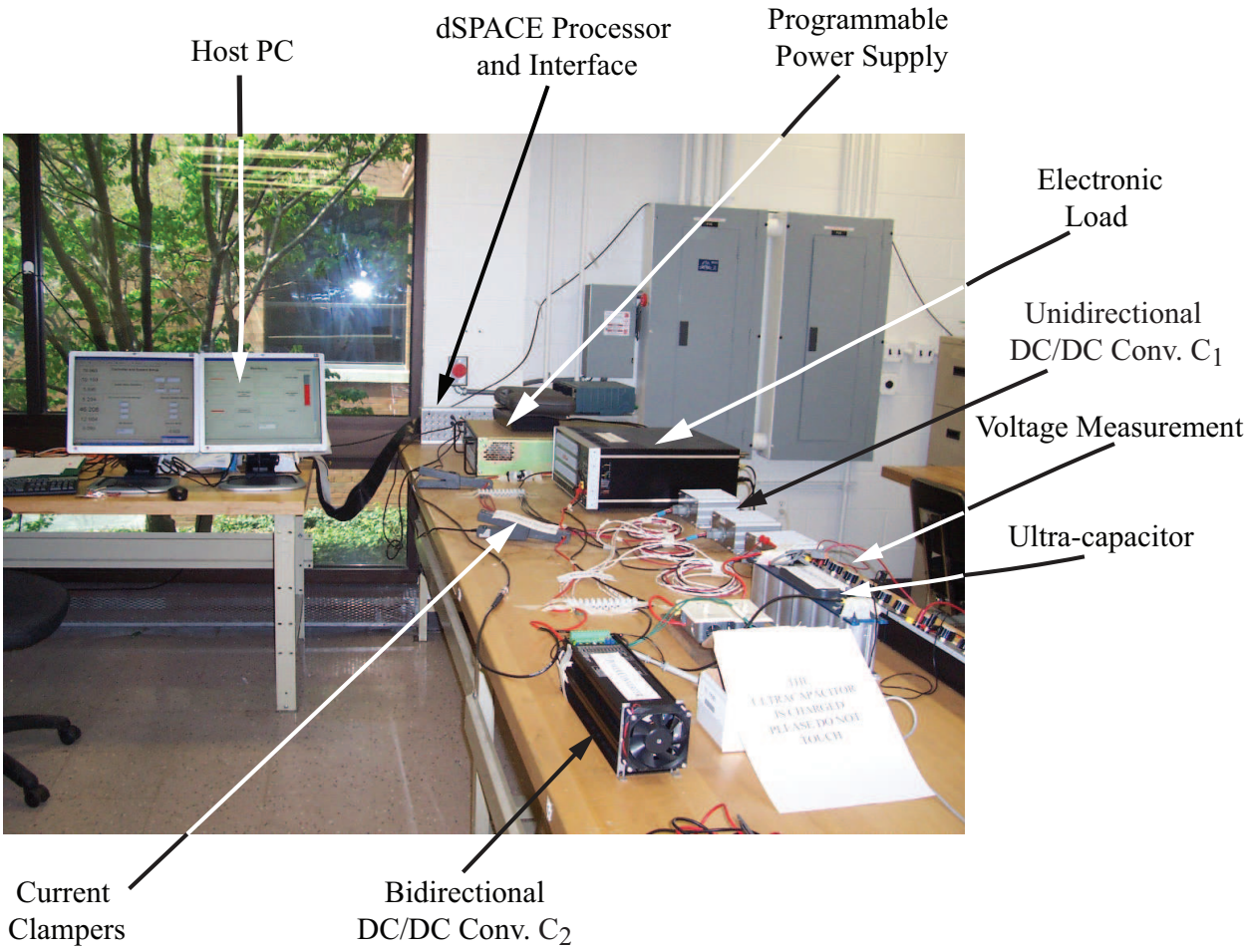

Figure 5.2: Experimental Test Stand Setup

5.1 Fuel Cell Emulator

A Solid Oxide Fuel Cell system is emulated by executing a detailed mathematical model on a dSPACE® DS1103 real time processor in conjunction with a $100V/50A$ programmable power supply. A schematic diagram of the emulator is shown in Fig.5.3. The DS1103PPC controller is fully programmable from the MATLAB® / Simulink® environment. The programmable power supply is run in voltage control mode with isolated analog input from the DS1103PPC controller. A host PC is used for real-time monitoring and tuning of the hybrid system using dSPACE® Control-Desk® software.

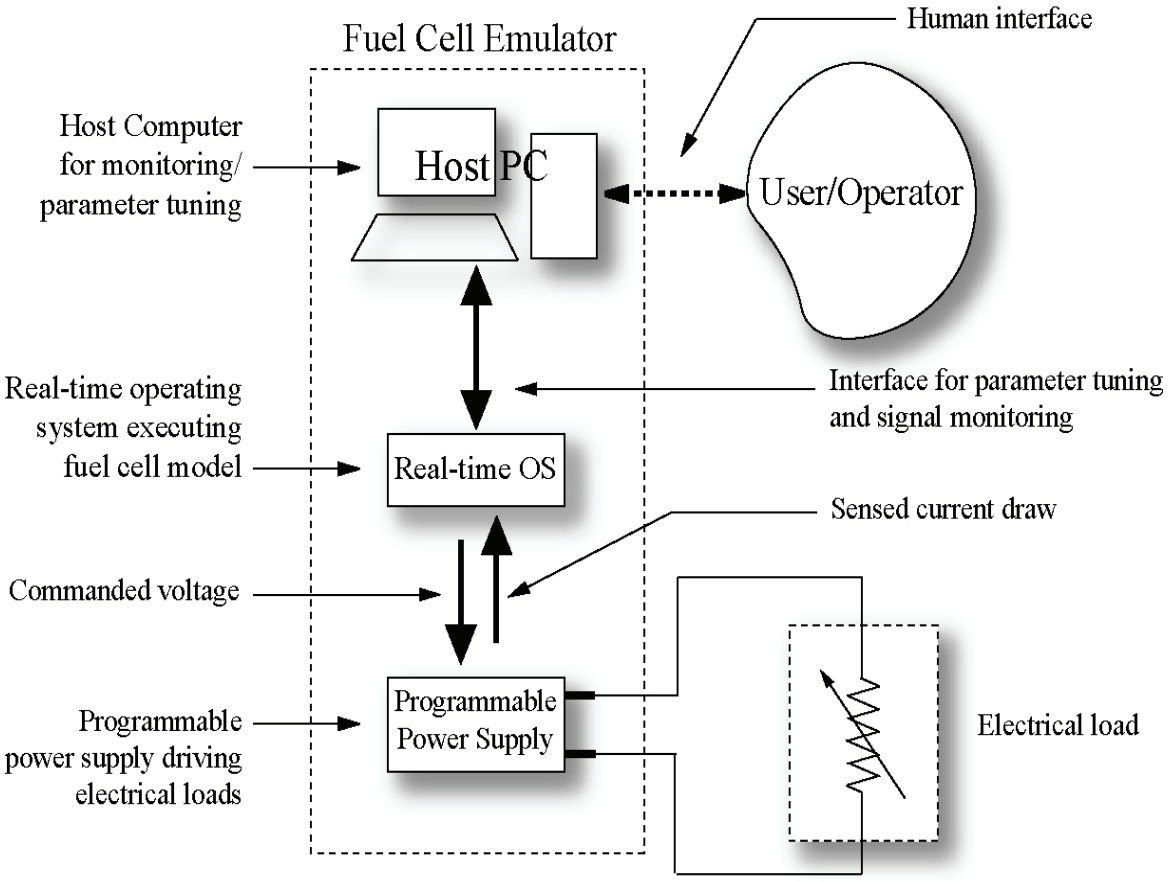

Figure 5.3: Fuel Cell Emulator

5.1.1 Fuel Cell Model

The fuel cell Module used in this experimental set up is a tubular Solid Oxide Fuel Cell system, described in section 2.1. It is modeled in Simulink® / Matlab® environment. The essential dynamics of the fuel cell system are modeled using fundamental solid volume and gas control volume models. The details of this model are provided in [14, 53] and a simulink® block diagram of the model is shown in Fig.5.4. The model is validated against data published in [18, 46]. The voltage-current characteristic of the SOFC system under consideration, at 80% utilization, is shown in Fig.5.5. The SOFC model is validated against published data in literature [18, 46]. The V-I characteristics in Fig.5.5 matches well with typical SOFC V-I characteristics in [12].

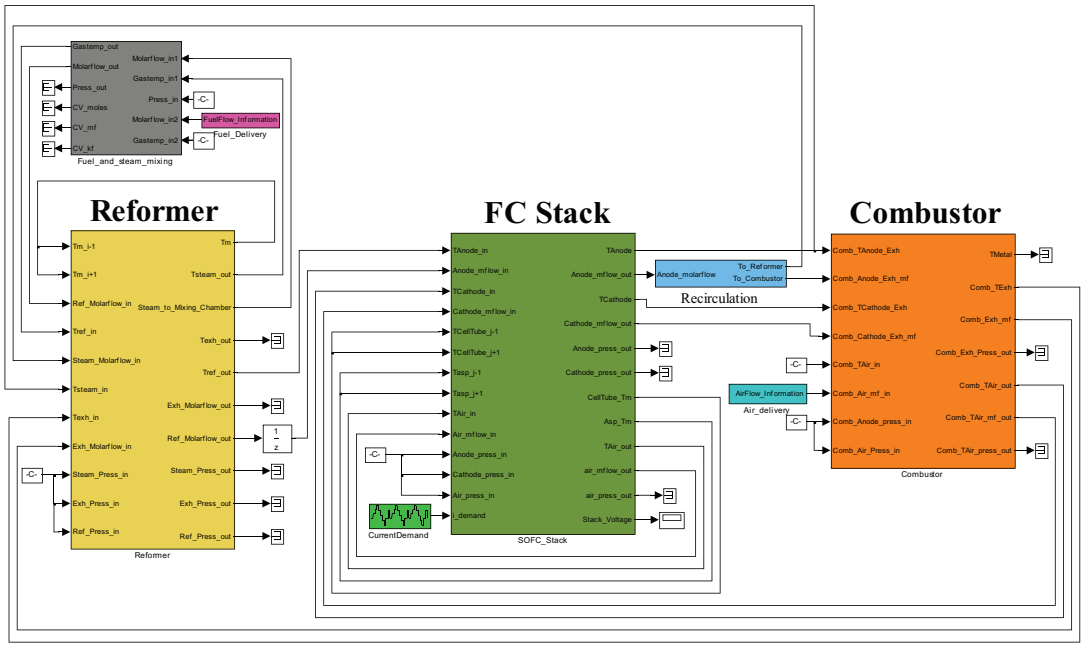

Figure 5.4: Fuel Cell Simulink Model Block Diagram

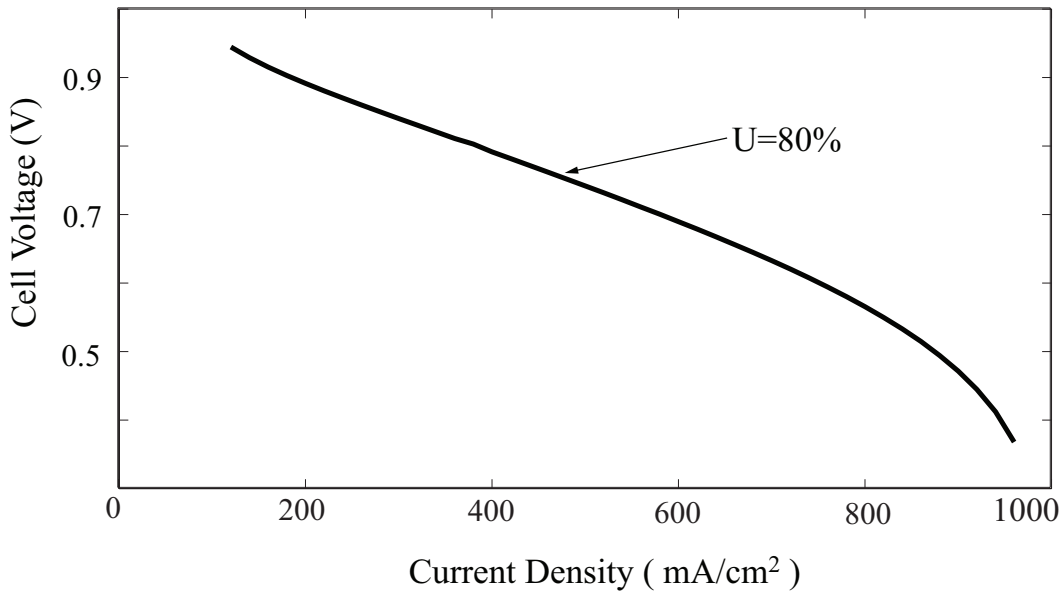

Figure 5.5: SOFC Voltage-Current Characteristics at 80% Utilization

5.1.2 dSPACE DS1103PPC

dSPACE® DS1103PPC is a controller board designed specifically for controlling high speed multi-variable digital controllers in real time simulations. It is a standardized controller that plugs into any computer using Industrial Standard Architecture bus, ISA as shown in Fig.5.6. CLP1103 is provided with 20 Analog to Digital channels (ADC), and 18 Digital to Analog channels (DAC). The digital to analog channels serve as output connectors that convert digital signals send from a computer to analog signals to be sent to analog world applications. The analog to digital channels serve as input channels of the dSPACE® that take analog input from analog devices, then convert them into digital signal to be used by the computer. Basically, these channels serve as an interface between the computer and the analog world. The dSPACE® board also comes with interface software called Control-Desk. The software allows on line monitoring during real-time simulation.

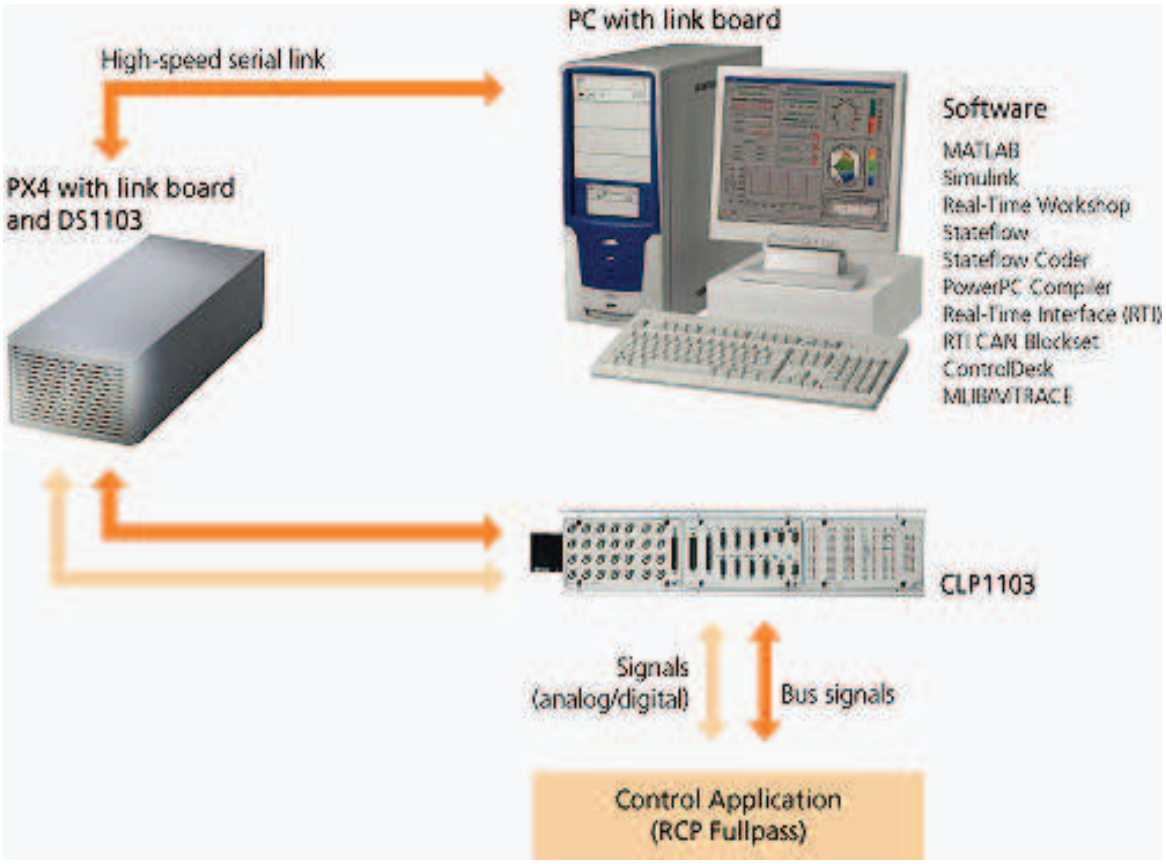

Figure 5.6: dSPACE DS1103 (Figure courtesy [4])

5.1.3 Programmable Power Supply

Programmable power supply used in this test stand is an SGA Series DC power supply from Elgar Sorensen. It is a general purpose power supply designed for laboratory tests and applications. It can supply up to 100V and 50A. It has the ability to operate in constant voltage or constant current mode with automatic cross over feature implemented through the voltage and current adjuster knobs shown in Fig.5.7. The input power is $208/220$VAC 3 phase AC, and can take frequencies between 47 to 63 Hz.

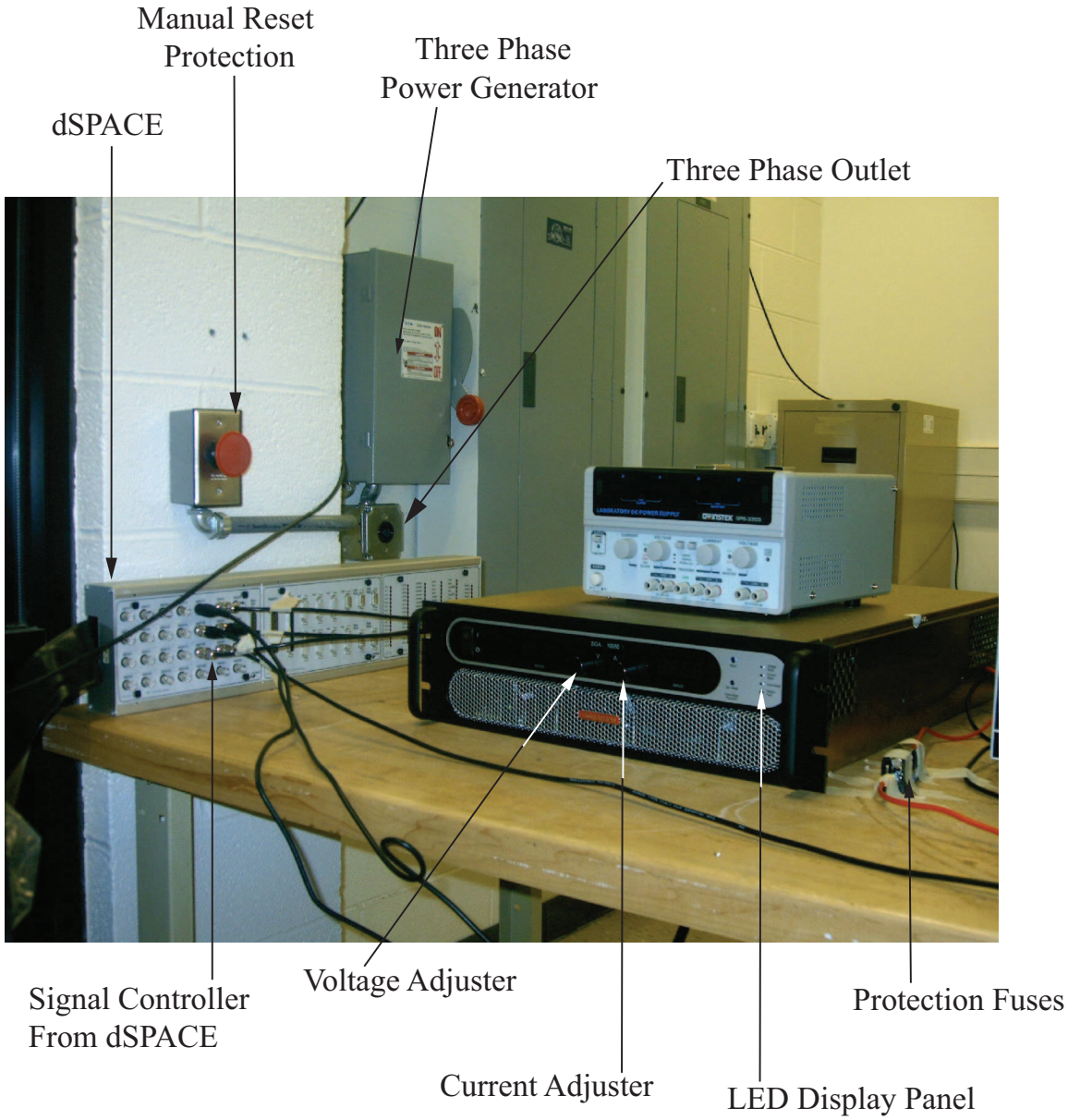

Figure 5.7: SGA Programmable Power Supply Setup

5.2 Electronic Load

The SLH series high power DC electronic load is designed to consume only DC power. In the experimental set up, a 1.8KW DC electronic load is used to consume the power of the fuel cell and the ultra-capacitor. The SLH can be programmed to operate in six different modes. In this application only constant current mode is used. In this mode, the current at the input of the load is fixed to a desired level regardless of the input voltage. The desired current level can be fixed by using analog signal sent from a computer through dSPACE. It can draw a maximum power of 1.8KW with a maximum voltage of 60V or a maximum current of 120A. The SLH DC electronic load series are provided with multiple features such as level selection of the operating modes and local voltage sensor dynamic operation mode. It is also provided with a memory bank, where applications sets can be stored. This allows the user to save settings of experiments. Detailed features are indicated in Fig.5.8.

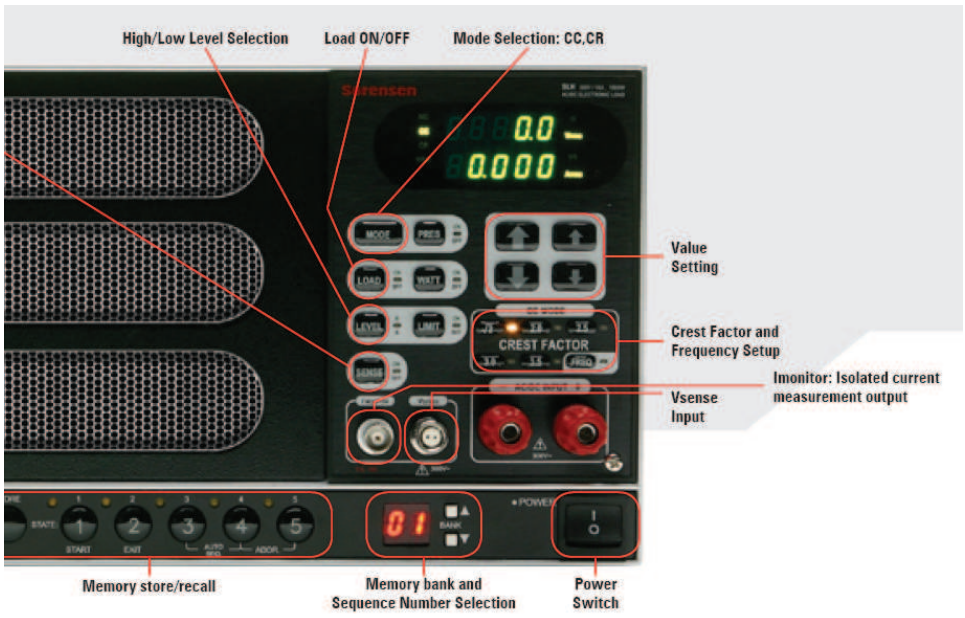

Figure 5.8: SLH Electronic Load Features (Figure courtesy [5])

5.3 Unidirectional DC/DC Converter

An SD-1000L-24 DC/DC converter, from Mean Well Inc, is used as unidirectional DC/DC converter, denoted by C_1 in Fig 5.1. This converter can adjust the output voltage to different levels. In the hybrid set up, it maintains the bus voltage V_L at a constant value of 24V at the output, with maximum output current rating of ≈ 40A. The efficiency of the converter varies between 88% and 91%. The higher the power level of the operation, the higher the efficiency becomes. This power converter is designed only to conduct in one direction, $i.e.$ from the fuel cell to the grid. The isolation from the output to the input is desired because the fuel cell needs to be protected from power delivered by the ultra-capacitor. While the voltage at the output is maintained at a fixed value, the input voltage varies from 19 to 72V, and the input current can go up to 50A.

5.4 Voltage Measurement

In this experimental set up, the dSPACE® DS1103 real time processor is used to convert the analog ultra-capacitor voltage measurements into digital values. In the voltage measuring unit, zero current draw from the ultra-capacitor is desired because dSPACE® is limited only to 10mA input current only. Thus, measurement of the ultra-capacitor voltage requires very high input impedance probes to prevent current draw by dSPACE®. In addition, the voltage range of dSPACE® channels is limited only to ± 10V and the ultra-capacitor voltage can go up to 16.2V. Thus scaling down the measurements is also required. Two precise decade resistors are connected in series as shown in Figs.5.2 and 5.9. They are adjusted to very high resistance values (MΩ range) to minimize current draw. The voltage probe measures the voltage across only one of the two resistances to scale down the measurements and provides the dSPACE with valid range of readings without drawing current.

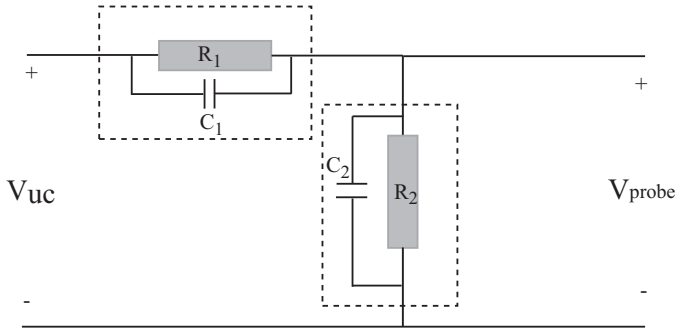

Figure 5.9: Voltage Probes

5.5 Ultra-capacitor Module

Ultra-capacitor is a very useful power storage device for applications that requires very high power density as discussed in section 3.2. Ultra-capacitors have resistive and capacitive components. The capacitive component determines the amount of voltage difference

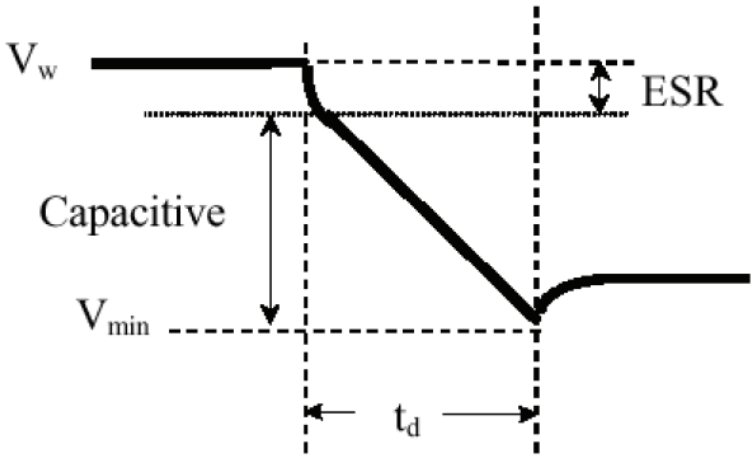

Figure 5.10: Ultra-capacitor Constant Discharge Profile (Figure Courtesy [3])

between its terminals with respect to the energy stored in each cell and the resistive component represents the difference in voltage due to the equivalent series resistance appearing across its terminals, as shown in Fig.5.10. The ultra-capacitor voltage during charging or discharging depends on both these components as shown in the following equation

$$dV = \frac{idt}{C} + iR$$

In this application, both these factors are critical. The capacitive component determines the amount of energy the system can relay on during transients. Thus, the higher the capacitive component the better the system performance becomes. The resistive component is not desired because can cause losses in the power and affects the speed in which the ultra-capacitor responds to power demands of the hybrid system.

A 16.2V series BMOD0250-E016 ultra-capacitor module, from Maxwell Technologies shown in Fig.5.11, is found to be ideal storage device for the hybrid system. The module has 250F capacitance and very low internal resistance estimated to be around 4.1 mΩ. Note that this resistance component is ignored in the calculations/derivations in sections 4.2 and

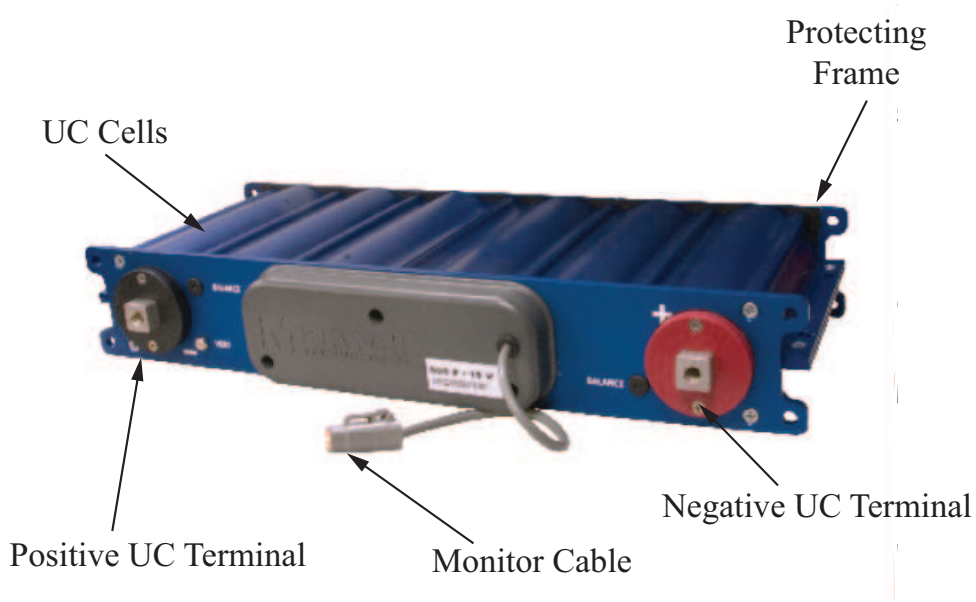

Figure 5.11: BMOD0250-E016 Ultra-capacitor Module (Figure Courtesy [3])

4.3.

5.6 Bidirectional DC/DC Converter

A bidirectional DC5050F-SU DC/DC converter from Zahn Electronics Inc, denoted by C_2 in Fig.5.1, is used to command the ultra-capacitor current i_{uc}. This converter has the ability to conduct power in both directions, $i.e.$ from the ultra-capacitor to the grid or from the grid into the ultra-capacitor. It is very important to have this capability because in addition to supplying power, the ultra-capacitor needs to have access to power from the grid at any time. The amount current and its direction are controlled by using an analog voltage regulator as shown in Figs.5.12 and 5.13.

DC5050F-SU consumes about 6W in normal operating conditions. Thus, its efficiency varies and depends on the operating conditions. The higher the operating power, the higher

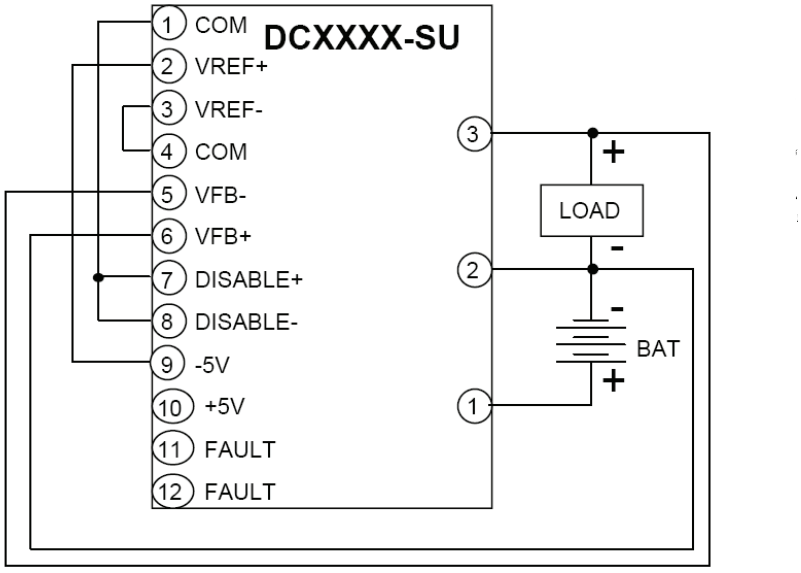

Figure 5.12: Bidirectional DC to DC Converter Configuration (Figure courtesy [6])

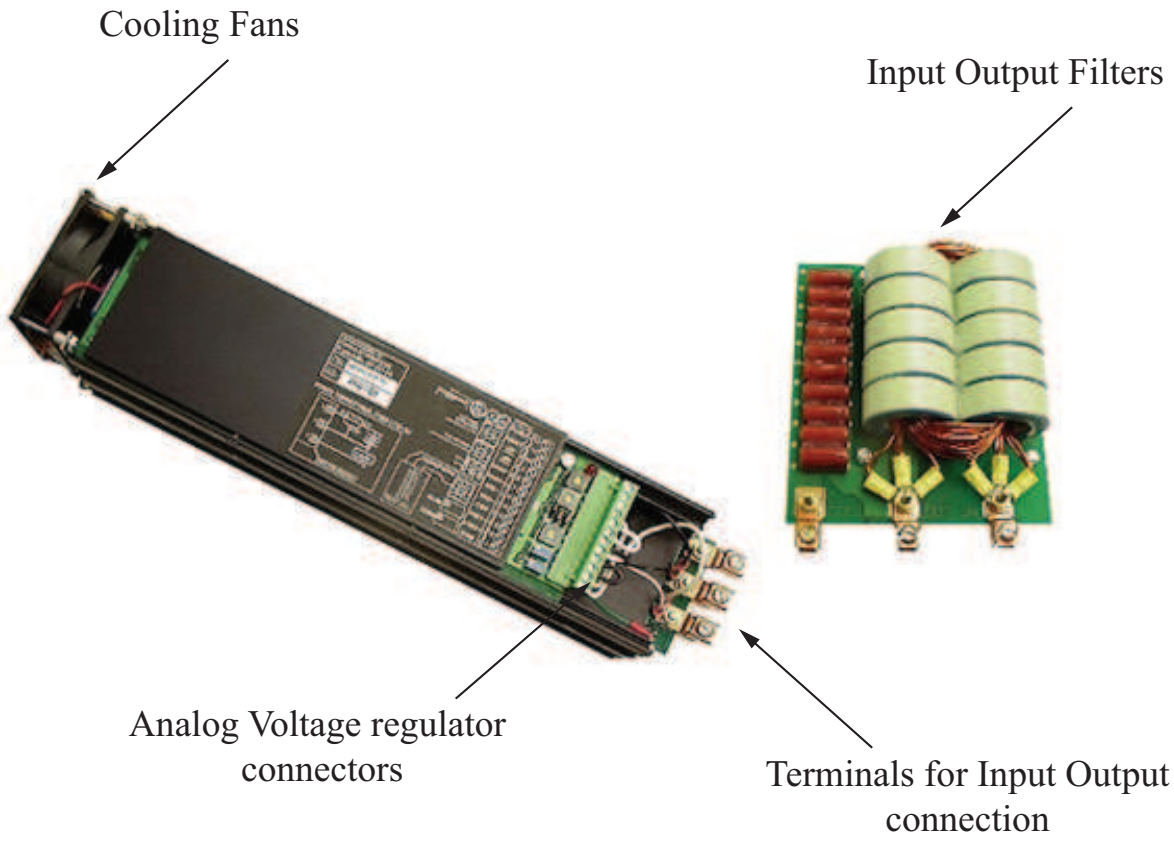

Figure 5.13: DC5050F-SU Bidirectional DC to DC Converter (Figure courtesy [6])

is the efficiency, and it can be as high as 98%. The switching frequency of this device is very important. The switching needs to be fast to respond to high frequency transients. For DC5050F-SU converter is exactly 125 kHz.

The converter connects both the grid and the ultra capacitor as shown in Fig.5.12. The ground is common and the converter is controlled through an analog signal from dSPACE in this experimental setup.

5.7 Current Clampers

Sensing the fuel cell and the load currents in the system are important for the control strategy. In this experimental set up, the current measurements are obtained using Fluke 80i-110s AC/DC current probes shown in Fig.5.14. This current clamper provides safe and wide range measurement capability without consuming any power from the system. The range of measurement is between 50mA and 100A with high fidelity output voltage. It has its own built in feature to filter undesired noise. It can be used both for DC or AC currents and up to 100kHz in frequency.

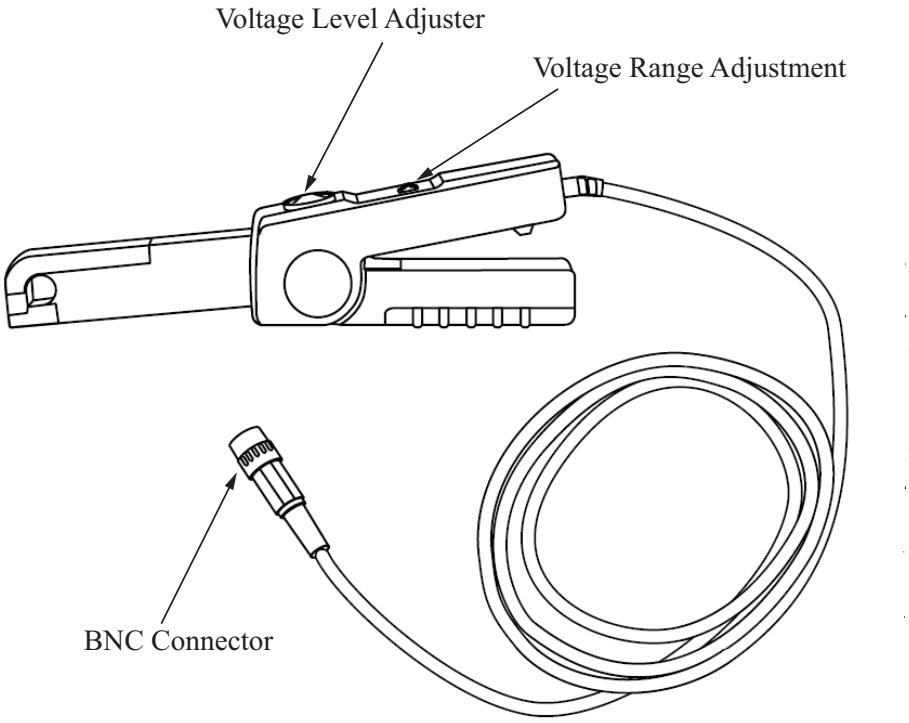

Figure 5.14: 80i-110s Current Clamper (Figure courtesy [7])

Chapter 6

Experimental Results

This section presents results of experiments carried out on the test-stand described in chapter 5. We first present the results of the nonlinear control strategy followed by those of the H_∞ approach. In all tests, the Solid Oxide Fuel Cell system is emulated (section 5.1) with 50 cells connected in series, and each cell has an active area of $251\ cm^2$. In the plant model, the fuel supply dynamics is assumed to follow a first order dynamics with $\dot{N}_f(s) = [1/(2s+1)]\,\dot{N}_{f,d}(s)$. Neither control designs assume a knowledge of this dynamics. The bus voltage is maintained at $V_L = 24$V by converter C_1 in all experiments. Other salient aspects of the hybrid energy system, mentioned in chapter 3, are also applicable for all results presented in this section.

6.1 Validating Real-Time Simulation

As mentioned before, the Solid Oxide Fuel Cell system is emulated by executing a detailed mathematical model on a dSPACE® DS1103 real time processor in conjunction with a $100V/50A$ programmable power supply. To validate the real time simulations, a comparison test is conducted with the computer-model (Computer-model: Simulink model of SOFC without a dSPACE control board and the programmable power supply). A series of step changes in current demand are applied to both computer-model and emulated system under the same conditions. The objective of this test is to evaluate the effects of

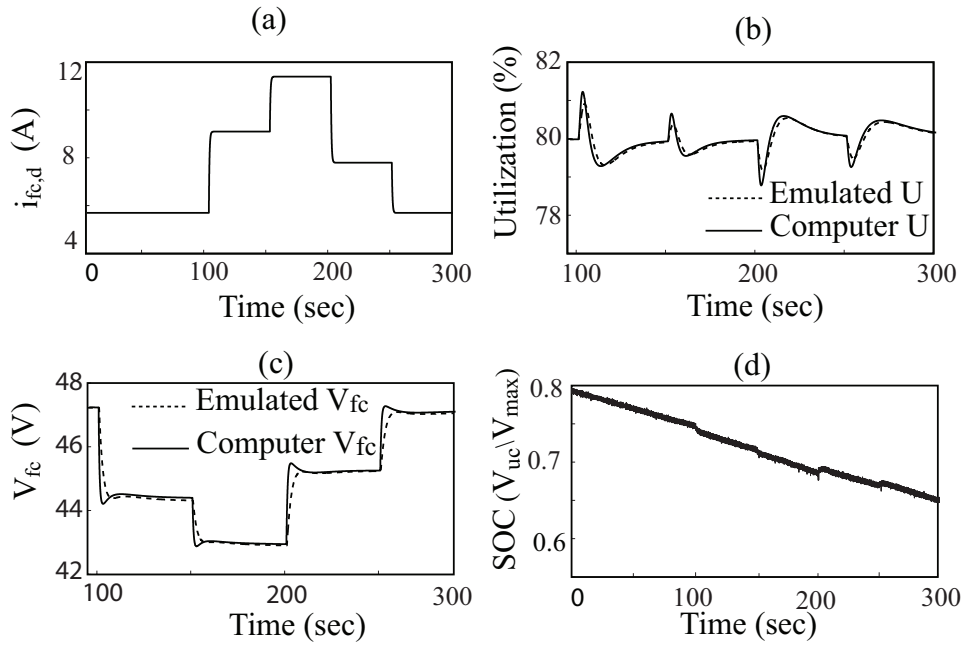

Figure 6.1: Hardware Emulator vs. Computer Simulator Results in Close-Loop Control

the dSPACE delays, the programmable power supply loses, and the sensor noises with respect to the detailed mathematical Simulink model of the SOFC. The computer-model is considered as a point of reference in this test.

The obtained results are shown in Fig.6.1. The step changes in fuel cell current demand are shown in Fig.6.1 (a). The utilization of both systems are captured in Fig.6.1 (b). There is a small difference between the computer model and the emulated utilization and that is due to accumulated delays in sensor reading and conversion time from analog to digital or from digital to analog in dSPACE®. Other than these small delays (negligible), both results match, as was expected. The same remark can be made for the fuel cell voltage shown in Fig.6.1 (c).

The nonlinear and the H_∞ control designs are designed to be robust to system uncertainty. However in the hardware simulations, the uncertainties of the hybrid system were not considered and that is evident in the decay of the SOC in the ultra-capacitor shown in Fig.6.1 (d). That demonstrates the need for need for robust control.

6.2 Nonlinear Control

This section presents results of two experiments where the nonlinear control strategy of section 4.1 was applied. The results are presented in Figs.6.2 and 6.3. Both experiments use the following parameter values: $U_{ss} = 0.8$, $S_t = 0.8$, $\bar{\eta}_1 = 1$, $\bar{\eta}_2 = 0.98$, $k_s = 0.1$, $k_p = 0.2$, and $k_d = 0.004$. The parameters δ_1 and δ_2 were chosen based on Eqs.(4.11) and (4.12), as follows:

$$\delta_1 \begin{cases} = 0 & \text{for} \quad E_s > 0 \\ = 2 & \text{for} \quad E_s \leq 0 \end{cases}, \quad \delta_2 \begin{cases} = 2 & \text{for} \quad E_{fc} > 0 \\ = -2 & \text{for} \quad E_{fc} \leq 0 \end{cases} \tag{6.1}$$

In Fig.6.2, i_L follows the current profile of Fig.6.2(a). This profile represents a standard drive cycle obtained from [65], where the velocity variation was simply interpreted as current variation. The variables related to the fuel cell, i_{fc}, V_{fc}, U and $\dot{N}_f$ are plotted in Figs.6.2(b), (c), (d) and (e) respectively. The results show very close control of U in spite

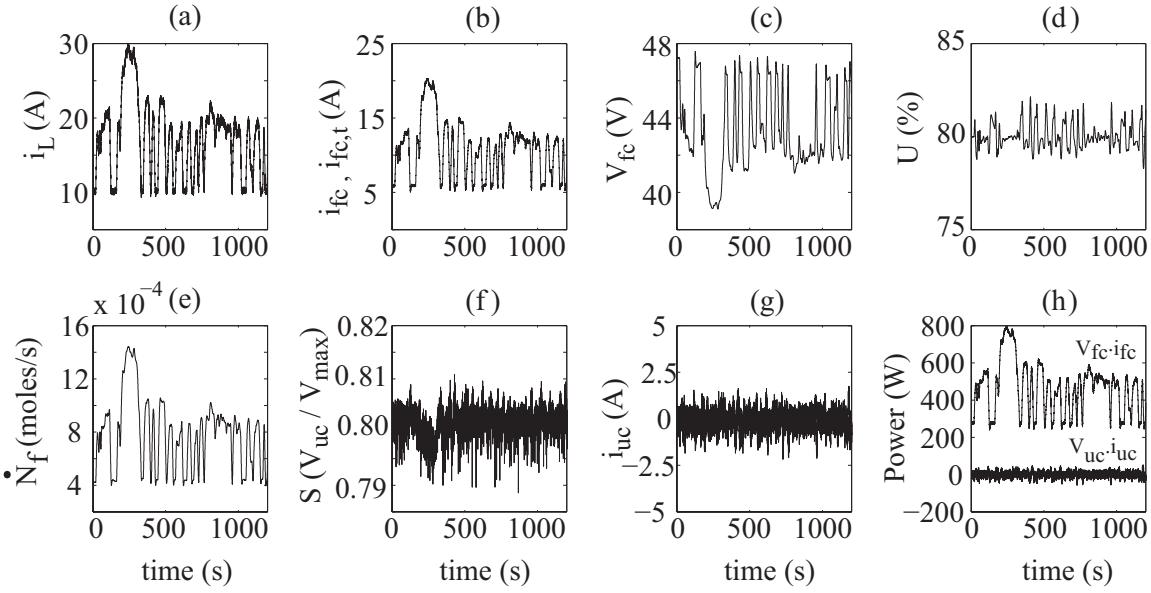

Figure 6.2: Nonlinear Control under Drive-cycle Variation of i_L

of rapidly varying i_L. The variables S and i_{uc} are plotted in Figs.6.2(f) and (g) respectively.

The plots show tight control of S around the target $S_t = 0.8$. Fuel cell current i_{fc} is consistently lower than i_L since V_{fc} is higher than the bus voltage $V_L = 24$V. The rapid variation of i_{uc} around zero shows that the ultra-capacitor supplies transient power and is also due to the parameter δ_2. The fuel cell and ultra-capacitor powers are plotted together in Fig.6.2(h).

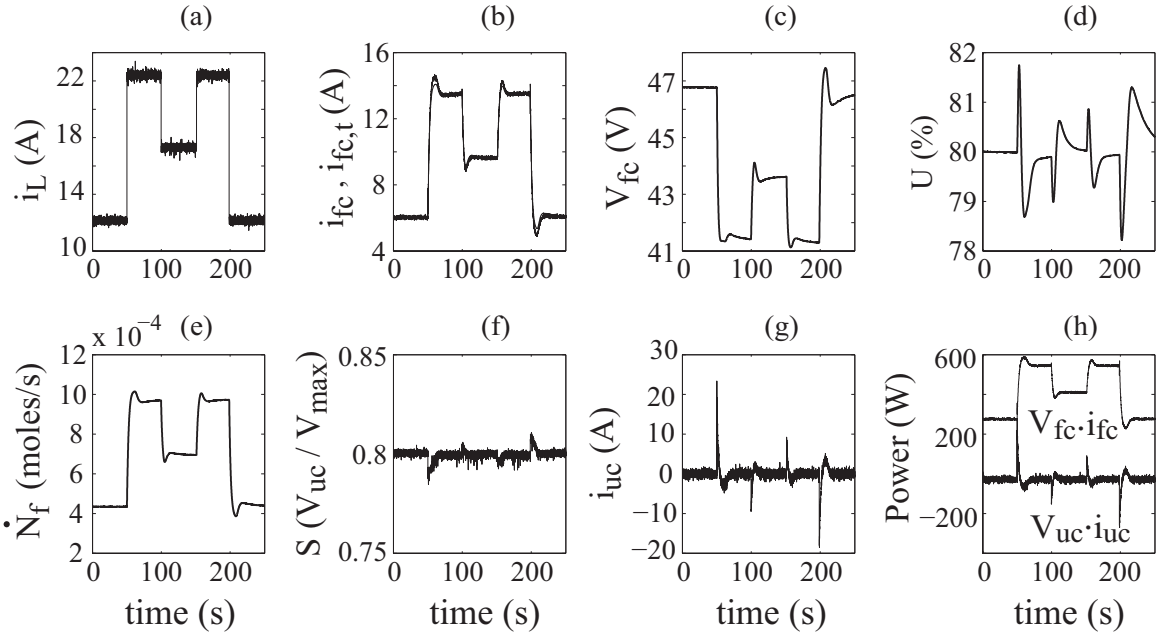

Figure 6.3: Nonlinear Control under Step Changes in i_L

The next result, shown in Fig.6.3, illustrates the system's close-loop response under a series of step changes in the power demand. In Fig.6.3(a), i_L is subject to step changes. The corresponding variations in i_{fc}, V_{fc}, U and $\dot{N}_f$ are plotted in Figs.6.3(b), (c), (d) and (e) respectively. In Fig.6.3(b), both i_{fc} and $i_{fc,t}$ are plotted together but the difference is not clear as they are almost coincident ($E_{fc} \approx 0$). S and i_{uc} are plotted in Figs.6.3(f) and (g) respectively, and the fuel cell and ultra-capacitor power are plotted together in Fig.6.3(h). The results show very close control of U in spite of drastic transients in i_L. In comparison to Figs.6.2(f), (g) and (h), Figs.6.3(f), (g) and (h), show greater variations in S, i_{uc} and the ultra-capacitor instantaneous power. This is because step changes introduce faster transients than the drive cycle.

6.3 H_∞ Control

The results of H_∞ control are presented in Figs.6.4 and 6.5. In this experiment, the following control parameters were chosen: $U_{ss} = 0.8$, $S_t = 0.8$, $k_p = 0.2$, and $k_d = 0.004$. The following ranges were chosen for uncertain quantities with nominal values at the middle of their respective ranges, $\bar{\eta}_1, \bar{\eta}_2 \in [0.8\ 1]$, $V_{fc} \in [40\ 60]$V and $V_{uc} \in [9.6\ 16.2]$V. Referring to Eq.(4.54), the following dynamic feedback law was determined through H_∞ synthesis,

$$K_\infty = \frac{v(s)}{e(s)} = \frac{3.587 \times 10^4 s + 1.75 \times 10^4}{s^2 + 1049s + 105.4}$$

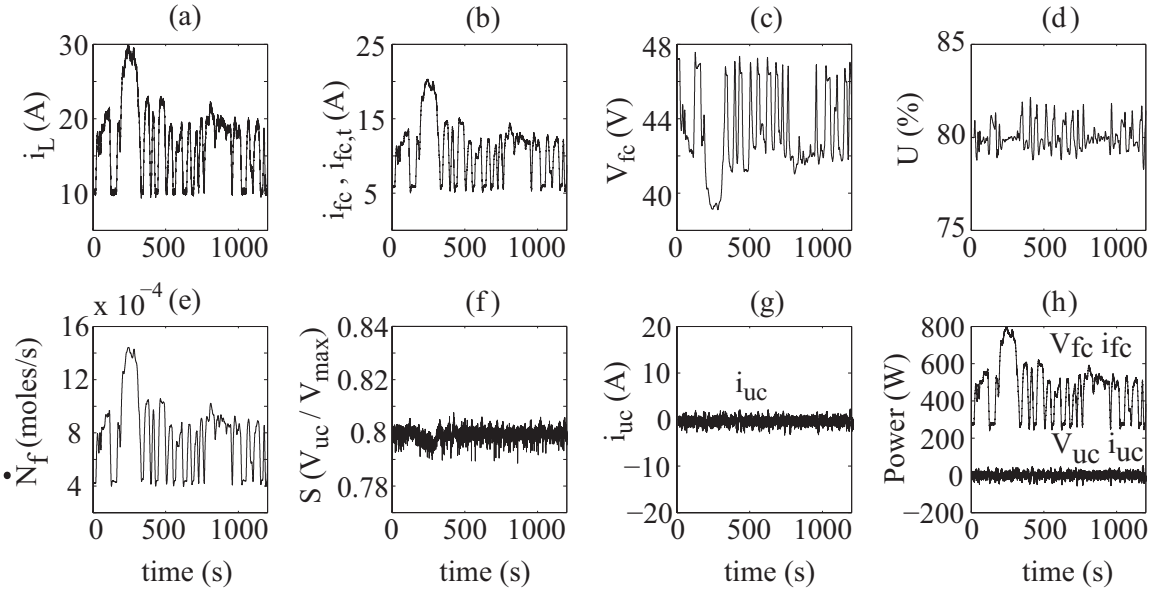

Figure 6.4: H_∞ Control under Drive-cycle Variation of i_L

Figs.6.2 and 6.4 compare the performance of the H_∞ controller and the nonlinear control strategy under drive cycle variation of i_L. There is no remarkable difference in the results using nonlinear control and H_∞ control. The non linear control performance is slightly better whereas the H_∞ control can be tuned to have a better performance. In Fig.6.5, i_L is subject to the same step changes as in Fig.6.3. The only noticeable difference between nonlinear and H_∞ strategies is in the SOC control, Figs.6.3(f) and 6.5(f), where the nonlinear control seems to perform slightly better.

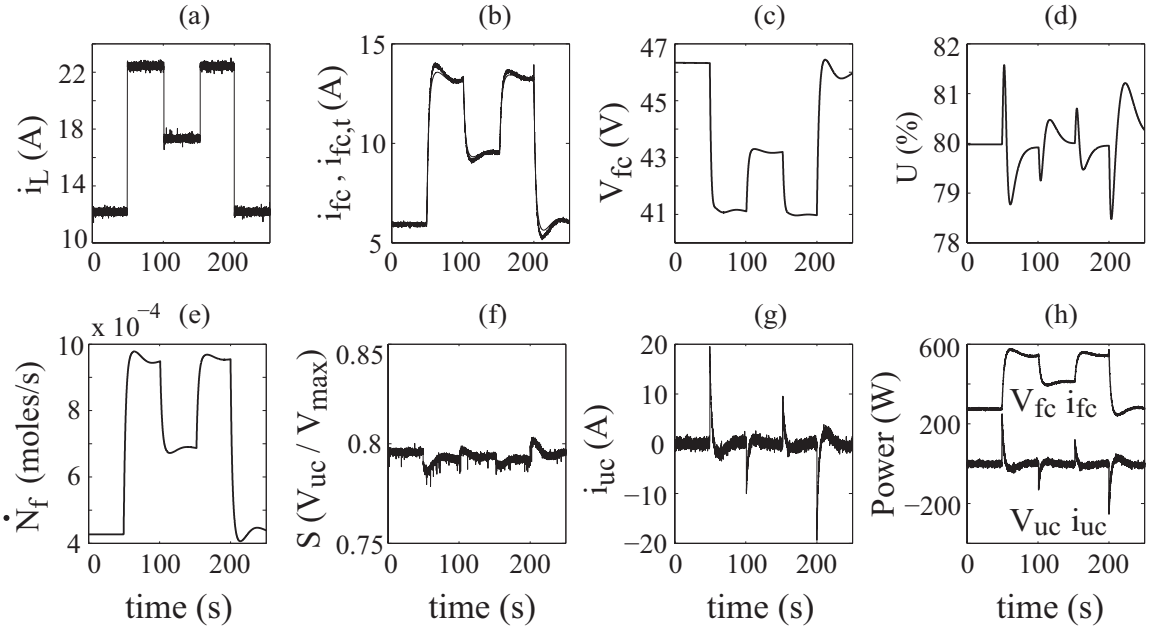

Figure 6.5: H_∞ Control under Step Changes in i_L

6.4 Demonstrating the Need for Robust Control

To demonstrate the the need for robustness of the nonlinear control strategy, three different tests are applied to the hybrid system. During these tests, the hybrid system is considered without the uncertainties in its parameters (η_2 and η_2), i.e. the robustness terms (δ_1 and δ_2) from the design in section 4.2 are ignored.

In the first test, the same spectrum shown in Fig.6.2 (a) is applied as fuel cell current demand. The results are shown in Fig.6.6. It is evident that the fluctuations in the utilization are bigger in Fig.6.6 (d) compared to Fig.6.2 (d), where fluctuation does not exceed 2%. Also, the i_{fc} and $i_{fc,t}$ are different as shown in Fig. 6.6 (b).

The second test, a step change in power is applied as shown in Fig.6.7 (a). The obtained results shows that the ultra-capacitor SOC is not maintained at the desired level as shown in Fig.6.6 (f). It deviates from target as the current demand changes. Moreover, the target and the measured fuel cell currents are not the same as shown in Fig.6.6 (b) because uncertainties in the power electronics' efficiencies are ignored by the controller. There is

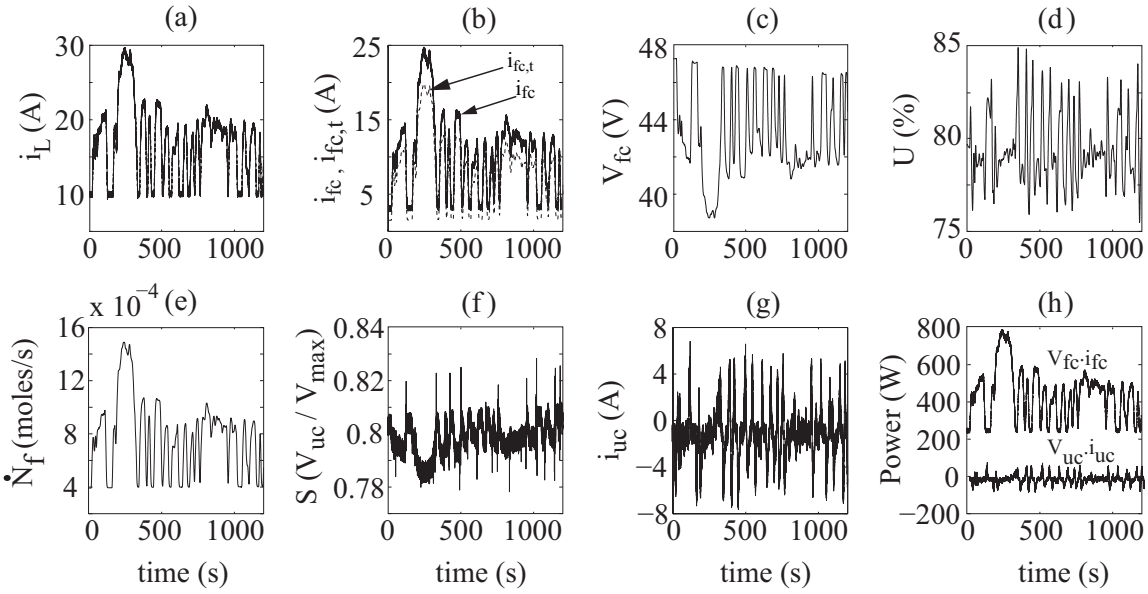

Figure 6.6: Nonlinear Control under Drive-cycle Variation of i_L without Robustness Terms

almost a 2A difference between them and that causes bigger fluctuations in the utilizations as shown.6.7 (d).

In the third test, a different pattern of step change in fuel cell current demand is applied as shown in Fig.6.8 (a). Again, the SOC of the ultra-capacitor is not maintained constant ($S \neq 0.8 \rightarrow E_s > 0$), also the target and measured fuel cell current are not equal ($i_{fc} \neq i_{fc,t}$ $\rightarrow |E_{fc}| > 0$).

Based on the results obtained from these three tests, uncertainties of the hybrid system parameter need to be considered in the control strategy. These results also demonstrate the robustness of the controller designed in section 4.2.

As mentioned in section 6.1, the uncertainties of the hybrid system are not taken in consideration for the hardware test. Consequently, the state of charge of the ultra-capacitor is not regulated at desired level as shown in fig.6.1 (d). The SOC decreased by 15% after 300 sec. With longer running time, the ultra-capacitor will completely discharge and will stop supporting the fuel cell. Again, this confirms the need for robust control.

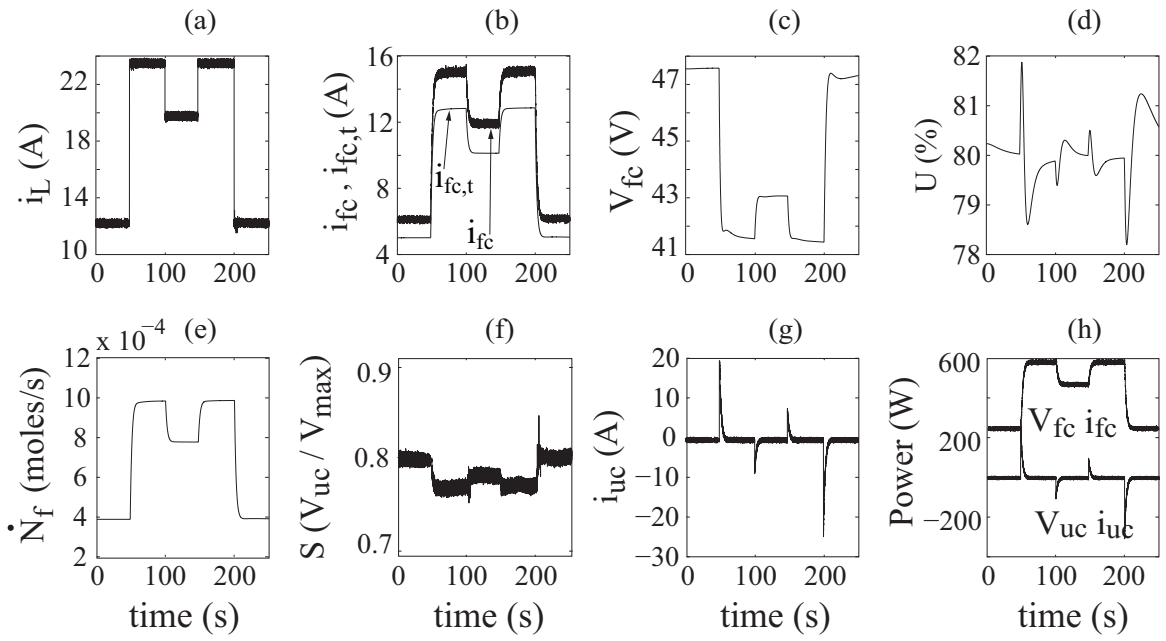

Figure 6.7: Nonlinear Control under Step Changes in i_L without Robustness Terms

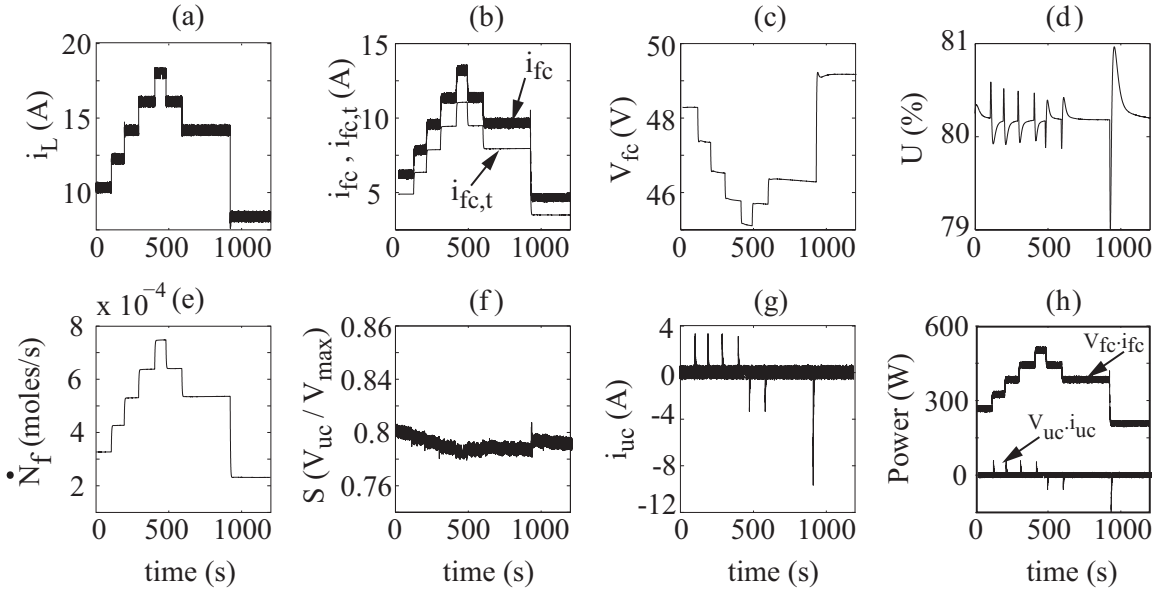

Figure 6.8: Nonlinear Control under Additional Step Changes i_L without Robustness Terms

Chapter 7

SOFC Ultra-capacitor Battery Hybrid System

7.1 Comparison of Hybrid Architectures

A new hybrid system design is proposed in this chapter. Previously, only an ultra-capacitor was used as a secondary storage element. However, due to limitations of the ultra-capacitor described in section 3.2, the hybrid system cannot operate in high power applications. In this design, shown in Fig 7.1, a lithium-ion battery is added to the system as another secondary storage unit. The battery is connected in parallel with the ultra-capacitor and the SOFC using a bidirectional DC/DC converter, C_3, in a configuration similar to the ultra-capacitor.

The objective behind this design is to improve the ability of the hybrid system to operate in high power applications. As described in section 3.1, lithium-ion batteries have high energy density and light weight. However, they have poor cycle life. Hence in this strategy, the ultra-capacitor is used to handle fast transients in power demand, and the battery is used to protect both the ultra-capacitor and the fuel cell from big transients. This ensures that the high efficiency and high durability of the ultra-capacitor are fully utilized, and the lifetime of the battery is maximized by protecting it from fast-current charges and discharges. The delayed degradation of the battery life and improved the ability of the hybrid system to

handle big transients in power demands are major advantages for the combined battery ultra-capacitor as secondary power unit.

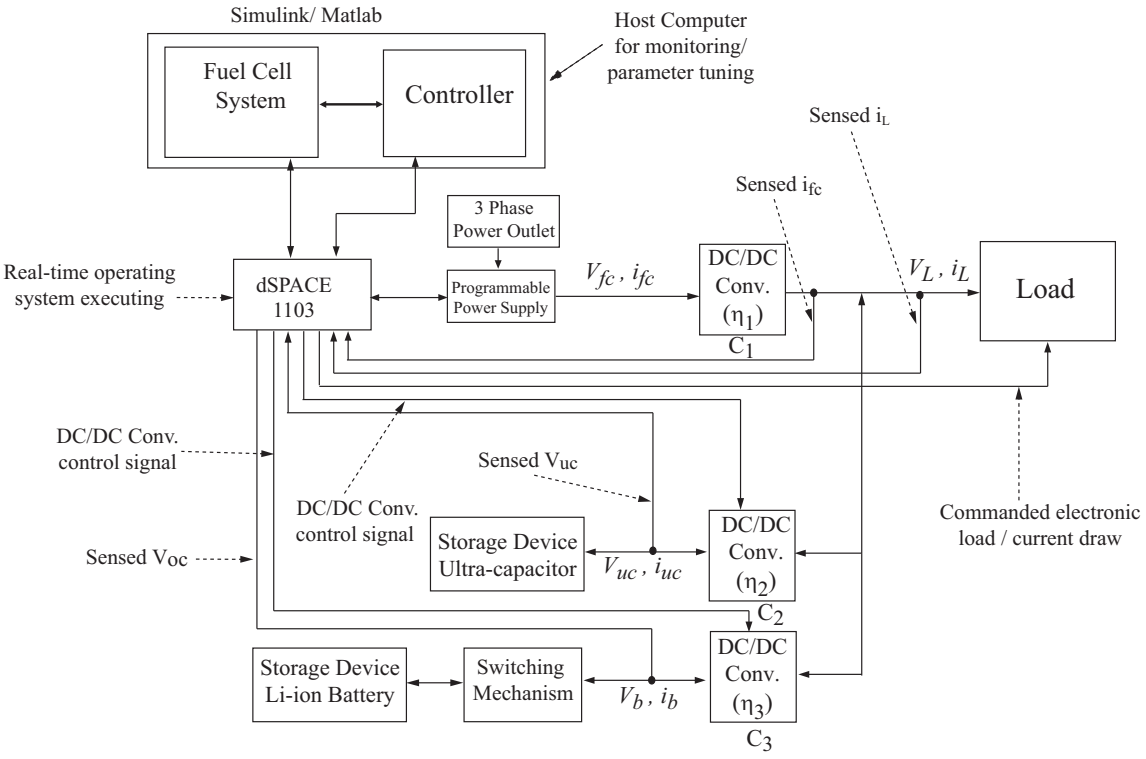

Figure 7.1: Schematic Diagram of SOFC Ultra-capacitor Battery Hybrid System

7.2 Characterizing U24-12RT Series Lithium-ion Battery

7.2.1 Battery State of Charge Measurements/Estimation Method

State of charge of the battery unit is required for the proposed control strategy of the ultra-capacitor battery hybrid system. Measuring SOC of lithium-ion batteries is a challenging problem. Using V_{oc} to estimate SOC is found to be roughly used for any type of batteries. The simplicity of this method makes it attractive in many applications. In this method, measuring V_{oc} provides the corresponding SOC of the battery as long as the relationship

between them is well known. However, the relationship cannot be exactly the same for every battery. But, it varies with the difference in capacity among batteries, and presents different results even if the batteries are fabricated from the same materials and structures. Moreover, the needed time for the terminal voltage of any battery to converge to V_{oc} (response time)is different and critical. The following section compares the response time of U24-12RT lithium-ion battery from Valence Technology Inc, with a conventional lead-acid battery.

7.2.2 Lithium-ion vs. Lead-acid Battery V_{oc} Convergence time

As an investigation, a comparison test between a NP65-12BFR lead-acid and U24-12RT lithium-ion battery shown in Figs.7.2 and 7.3 respectively, is conducted. The same charging / discharging conditions are applied for both batteries at the same time. The terminal voltage is measured and the results are shown in Figs.7.4 and 7.5 for the lead-acid and lithium-ion, respectively. Response time of the lead-acid battery is slower than the lithium-ion and it is represented as rise time and fall time in both figures. As shown in 7.5, the open

Figure 7.2: NP65-12BFR Lead-acid Battery Module from Energies, Inc

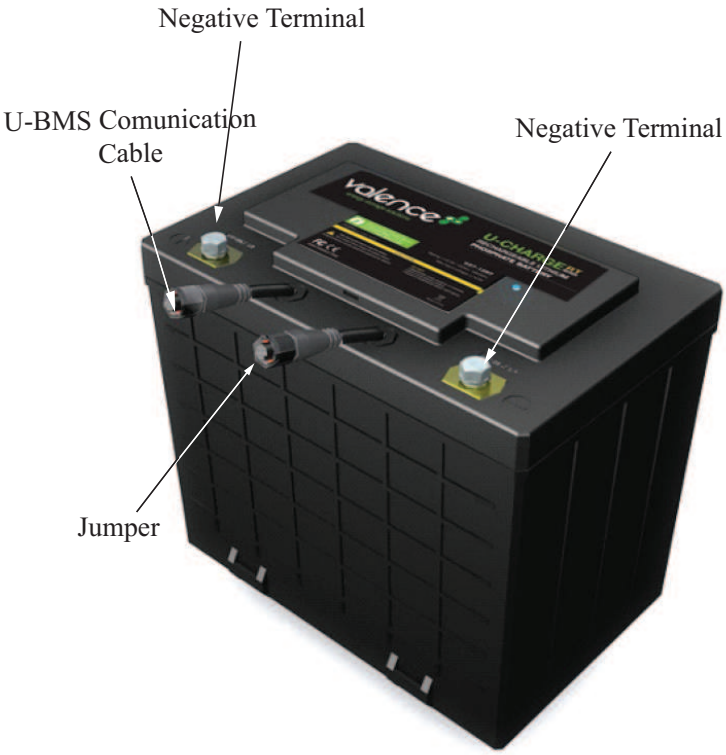

Figure 7.3: U24-12RT Li-ion Battery from Valence Technology,Inc(Figure courtesy [8])

circuit voltage can be approximated in about 5 sec after the terminals are disconnected from the applied charging/discharging voltages. However, lead-acid battery needs more than 80 sec to converge to V_{oc}.

Based on this result, obtaining the open circuit voltage for lithium-ion battery is practically easier and faster. Thus, estimating SOC of lithium-ion battery using V_{oc} is possible as long as the relationship between them is available. The outcome of this investigation is encouraging. Therefore, there is a strong possibility to incorporate this method into the hybrid system as future work. The following section explores this idea further, the relationship between V_{oc} and SOC of U24-12RT lithium-ion battery is investigated.

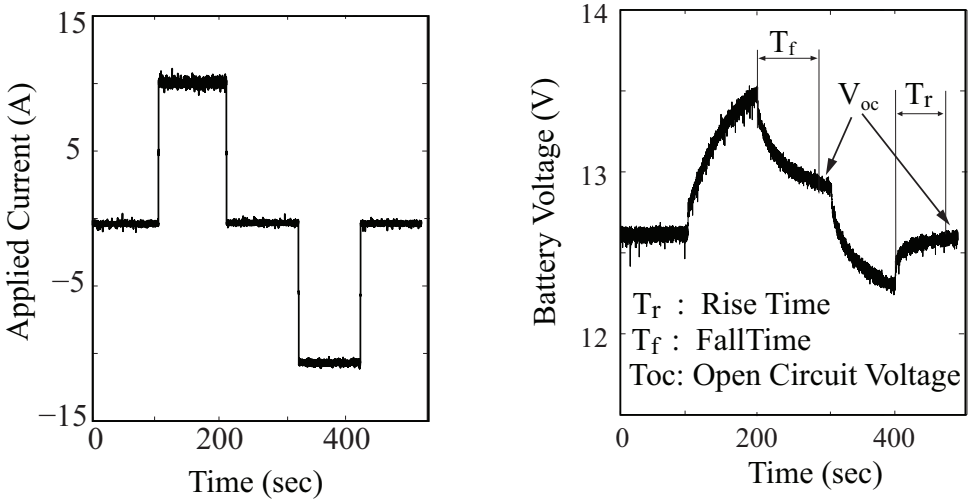

Figure 7.4: Lead-acid Battery Charging / Discharge Response

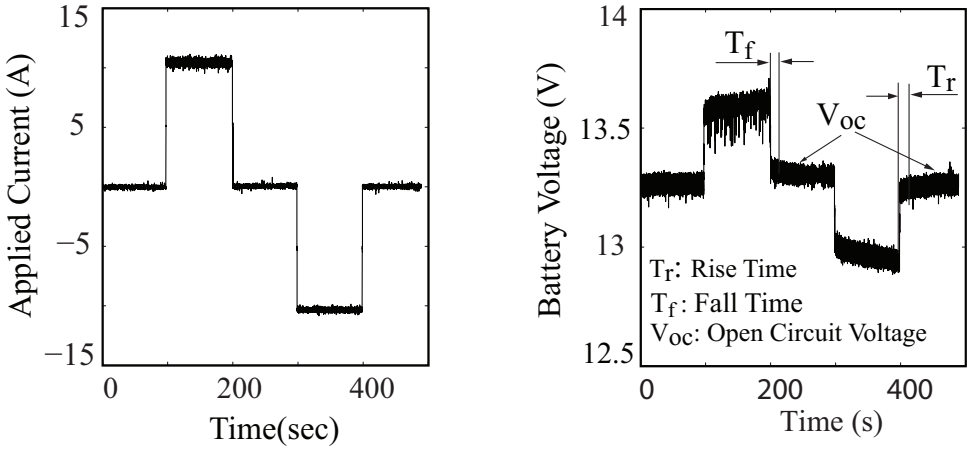

Figure 7.5: Lithium-ion Battery Charging / Discharge Response

7.2.3 SOC / Voc of U24-12RT Lithium-ion Battery

To measure SOC of the battery using the proposed approach, SOC versus V_{oc} data are required. U24-12RT lithium-ion battery from Valence Technologies Inc, shown in Fig.7.3, is included with a module Diagnostics Tool-kit shown in Fig.7.6. The Diagnostic Tool-kit can provide SOC of the battery at any time. Note that, the Diagnostic Tool-kit cannot be used for in the control strategy. However, it is used only to create a relationship between the V_{oc} and SOC of the U24-12RT Battery. The obtained relationship will be used in the SOC estimation in the control development.

In the previous section, 5 sec waiting time for the terminal voltage to converge to an approximate V_{oc} is found to be enough to estimate SOC. Based on this, a plot of V_{oc} vs. SOC is generated. The plot is shown in Fig.7.7. The measured terminal voltages under charging and discharging are very close to the actual V_{oc}. However, the slop of the plots between 10 to 90% SOC are very flat. This magnifies the error in the corresponding SOC as highlighted in Fig.7.7. Thus, 5sec waiting time is not enough.

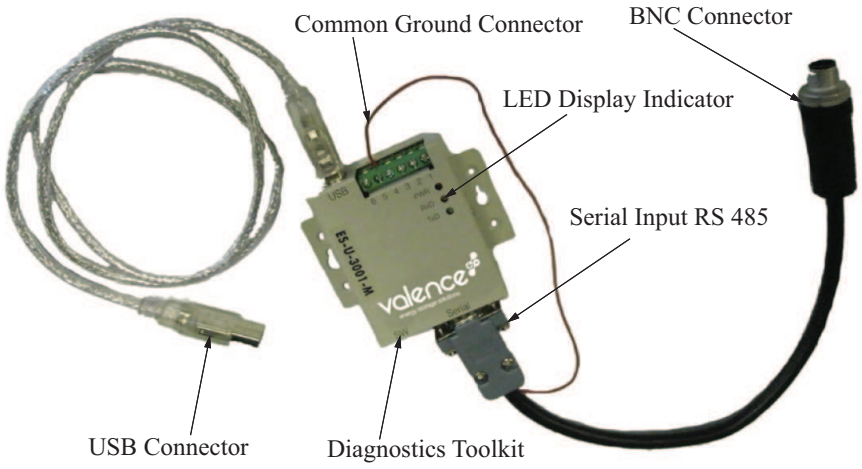

Figure 7.6: Diagnostics Tool-Kit for SOC Measurements of the Valence Lithium-ion Battery (Figure courtesy [8])

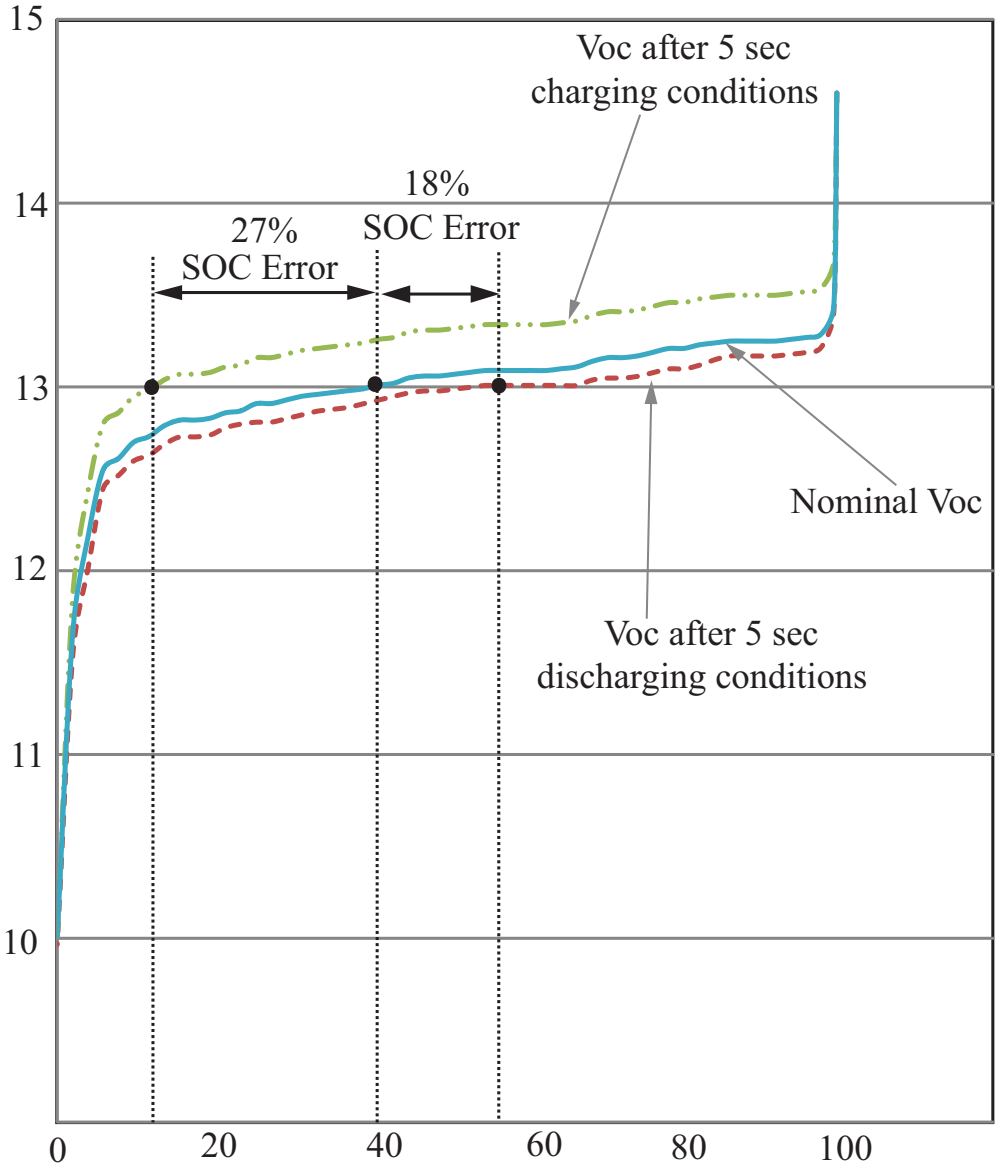

Figure 7.7: SOC vs. V_{oc} of Lithium-ion Battery

More tests are conducted to find the optimum waiting time. Four tests have been done to the battery to characterize its behavior under charging and discharging conditions. The table in Fig.7.8 shows the state of charge of lithium-ion battery and its corresponding open circuit voltage.

In the first test, a charging voltage is applied, both V_{oc} and the SOC of the battery are measured. The SOC measurements are done by using the Diagnostic-Tool-Kit from Valence Technologies Inc. The measurements of the corresponding V_{oc} are done after 5 sec from disconnecting the terminals of the battery from the applied voltage. In the second test, the same terminal voltage is measured but after 20 sec from opening the terminals. The results of the first and the second tests are shown in the second and the third column of table.7.8 respectively.

In the third and the fourth test, a discharging voltage is applied instead. The V_{oc} is measured after 5 sec and 20 sec respectively. The results are shown for both tests in fourth and the fifth column in table 7.8. The corresponding measurement of SOC using the Diagnostic Tool-Kit are shown in the last column of the table.

The results in table of Fig.7.8 indicates that the measurement of V_{oc} (both under charging and discharging conditions) converges to nominal values as the waiting time increases. To analyze these results precisely, All the obtained data in table 7.8 are plotted and compared with the nominal V_{oc} as shown in Fig.7.9. A 20 sec waiting time results show a better approximation of SOC but still with a margin error. Further research is required to improve this method.

Using this method in the hybrid system, a switching mechanism as shown in Fig 7.1 is required to disconnect the battery from the hybrid system. Then, waiting about 20 sec to measure the approximated V_{oc}. The other draw-back of this method is that during the disconnection of the battery, the ultra-capacitor is required to handle all the transients. That could practically not possible. To validate this proposed algorithm, further investigation is required and that is addressed as future work. In the following analysis, The battery SOC is assumed to be available.

SOC_RT_Software	Charging V_OC after 5 sec (V)	Charging V_OC after 20 sec (V)	Discharging V_oc after 5 sec (V)	Discharging V_oc after 20 sec (V)	SOC_Estimated (%)
255	14.6	14.6	14.6	14.6	100
254	13.69	13.49	13.41	13.39	99.60784314
250	13.54	13.34	13.22	13.24	98.03921569
245	13.52	13.32	13.19	13.22	96.07843137
240	13.51	13.31	13.18	13.21	94.11764706
235	13.5	13.3	13.17	13.2	92.15686275
230	13.5	13.3	13.17	13.2	90.19607843
225	13.5	13.3	13.17	13.2	88.23529412
220	13.5	13.3	13.17	13.2	86.2745098
215	13.49	13.29	13.15	13.19	84.31372549
210	13.48	13.28	13.12	13.18	82.35294118
205	13.46	13.26	13.1	13.16	80.39215686
200	13.46	13.26	13.1	13.16	78.43137255
195	13.44	13.24	13.08	13.14	76.47058824
190	13.42	13.22	13.06	13.12	74.50980392
185	13.41	13.21	13.05	13.11	72.54901961
180	13.41	13.21	13.05	13.11	70.58823529
175	13.39	13.19	13.04	13.09	68.62745098
170	13.36	13.16	13.01	13.06	66.66666667
165	13.35	13.15	13.01	13.05	64.70588235
160	13.34	13.14	13.01	13.04	62.74509804
155	13.34	13.14	13.01	13.04	60.78431373
150	13.34	13.14	13.01	13.04	58.82352941
145	13.34	13.14	13.01	13.04	56.8627451
140	13.34	13.14	13.01	13.04	54.90196078
135	13.33	13.13	13	13.03	52.94117647
130	13.32	13.12	12.99	13.02	50.98039216
125	13.31	13.11	12.98	13.01	49.01960784
120	13.31	13.11	12.98	13.01	47.05882353
115	13.3	13.1	12.97	13	45.09803922
110	13.27	13.07	12.95	12.97	43.1372549
105	13.26	13.06	12.93	12.96	41.17647059
100	13.24	13.04	12.91	12.94	39.21568627
95	13.23	13.03	12.89	12.93	37.25490196
90	13.22	13.02	12.88	12.92	35.29411765
85	13.21	13.01	12.87	12.91	33.33333333
80	13.2	13	12.85	12.9	31.37254902
75	13.18	12.98	12.83	12.88	29.41176471
70	13.16	12.96	12.81	12.86	27.45098039
65	13.16	12.96	12.81	12.86	25.49019608
60	13.12	12.92	12.8	12.82	23.52941176
55	13.11	12.91	12.78	12.81	21.56862745
50	13.08	12.88	12.74	12.78	19.60784314
45	13.07	12.87	12.73	12.77	17.64705882
40	13.07	12.87	12.73	12.77	15.68627451
35	13.04	12.84	12.69	12.74	13.7254902
30	12.98	12.78	12.63	12.68	11.76470588
25	12.95	12.75	12.6	12.65	9.803921569
20	12.86	12.66	12.52	12.56	7.843137255
15	12.8	12.6	12.45	12.5	5.882352941
10	12.43	12.23	12.01	12.13	3.921568627
5	11.85	11.65	11.53	11.65	1.960784314
0	10	10	9.97	10.02	0

Figure 7.8: Results of the Characterizing Tests of Lithium-ion Battery

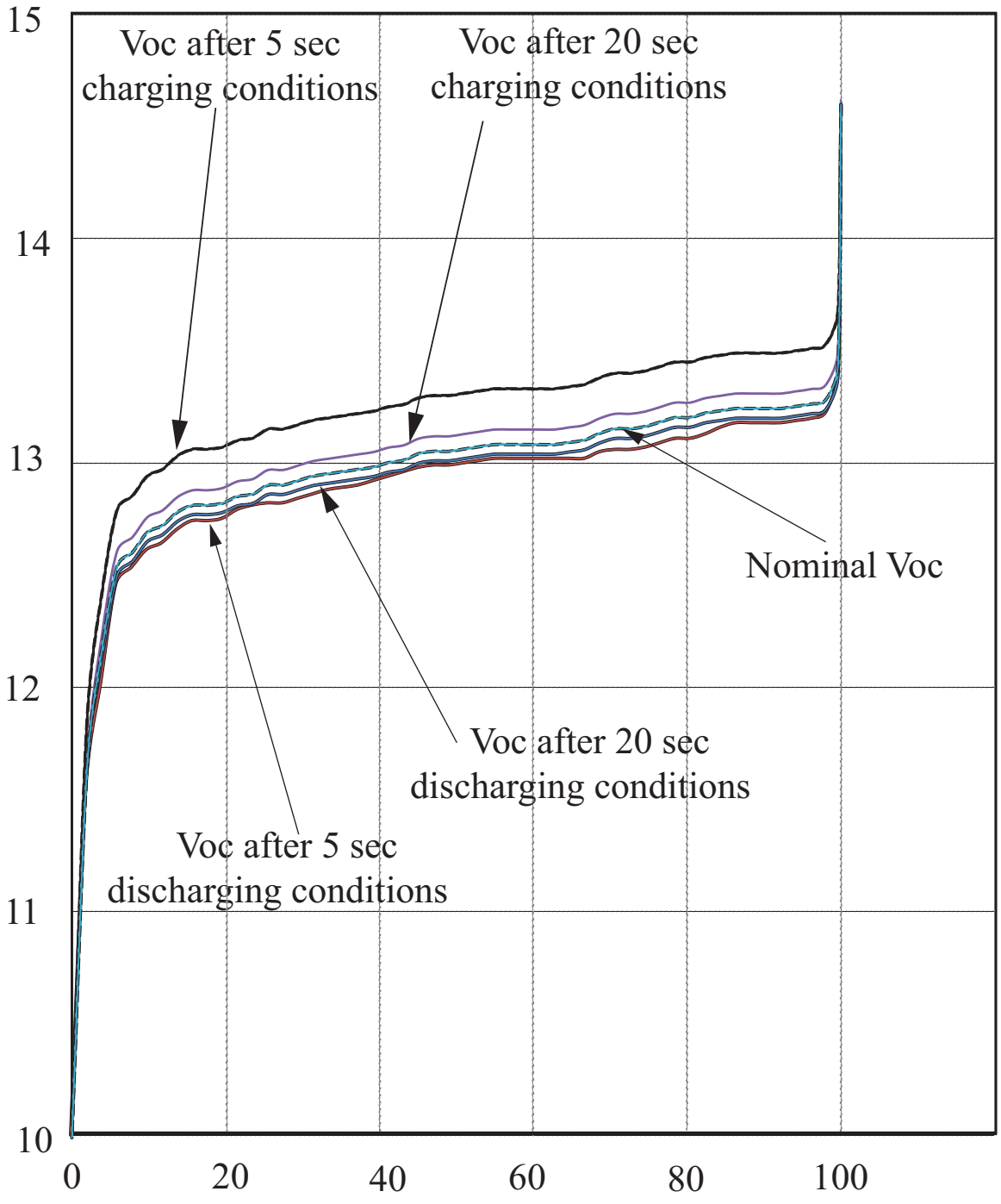

Figure 7.9: SOC vs. V_{ov} of Lithium-ion Battery with Longer Waiting Time

7.3 Nonlinear Control Design

The nonlinear control strategy for the hybrid system consisting of SOFC, ultra-capacitor and lithium-ion battery is presented through a schematic diagram shown in Fig.7.10. The strategy incorporates the lithium-ion battery shown in Fig. 7.3 and the same ultra-capacitor and SOFC used in the previous hybrid system and they are discussed in sections 3.2 and 2.1, respectively.

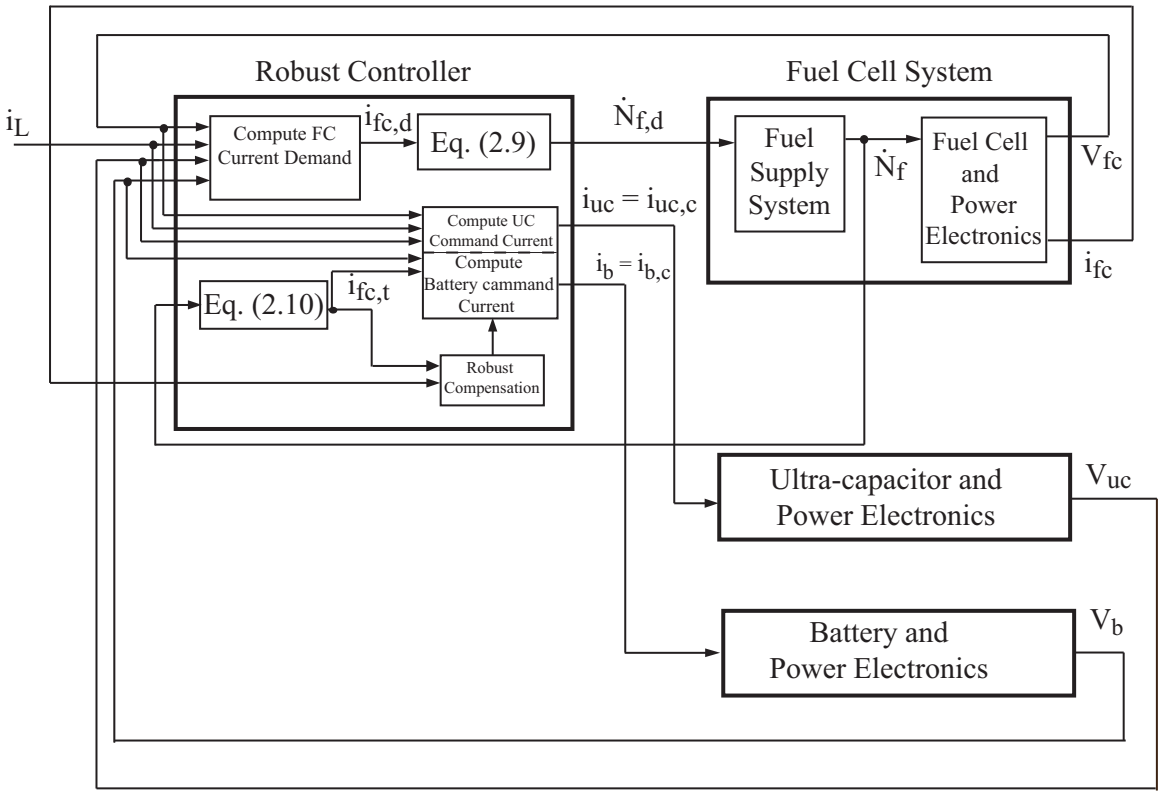

Figure 7.10: Nonlinear Control Approach for Battery Ultra-capacitor Hybrid System

The control strategy is a modified version of the strategy used for the fuel cell ultra-capacitor in section 4.2. The control objectives are:

1. To minimize the fluctuation in the fuel cell utilization,

2. maintain the SOC of both the ultra-capacitor and the battery at desired levels,

3. the control strategy is required to be robust to uncertainties of the system, and

4. to improve the hybrid system ability to handle high power applications and large transients in load demands

We consider the Lyapunov candidate function

$$\bar{V} = \frac{1}{2}\left(E_s^2 + E_{fc}^2 + E_{sb}^2\right) + \bar{V}_{fc} \tag{7.1}$$

where E_{sb} is the error in the state of charge of the battery. The derivative of the above candidate function is

$$\dot{\bar{V}} = \left(\dot{E}_s E_s + \dot{E_{fc}} E_{fc} + \dot{E_{sb}} E_{sb}\right) + \dot{\bar{V}}_{fc} \tag{7.2}$$

$\dot{\bar{V}}_{fc}$ is negative definite based on Eq.(4.18). $\dot{E}_{fc}$ is the same as in Eq.(4.33) given below

$$\begin{aligned}\dot{E}_{fc} = \quad & -\left[k_p/k_d + \left(V_{fc}/k_d V_{uc}\right)\left(\bar{\eta}_1/\bar{\eta}_2\right)\right] E_{fc} + \\ & \frac{1}{k_d \eta_2 V_{uc}}\left[V_L i_L\left(1 - \frac{\eta_2}{\bar{\eta}_2}\right) - \eta_1 V_{fc} i_{fc}\left\{1 - \frac{\bar{\eta}_1}{\eta_1}\frac{\eta_2}{\bar{\eta}_2}\right\}\right] - \frac{1}{k_d \delta_2}\end{aligned}$$

As in discussion around Eq.(4.33), the above expression can be simplified to the following

$\dot{E}_{fc} = -\alpha E_{fc} + \frac{1}{k_d}(\beta - \delta_2)$

then

$\dot{E}_{fc} E_{fc} = -\alpha E_{fc}^2 + E_{fc}\frac{1}{k_d}(\beta - \delta_2)$

where αE_{fc}^2 is positive. We choose β as in Eq.(4.13). For more details, see section 4.2. Because the objective is to develop a control strategy that is independent of the model of the lithium-ion battery, then the error in the state of charge of the battery E_{sb} depends on this observation :

$$\begin{aligned}\dot{E}_{sb} > 0 \quad \text{if} \quad i_b < 0 \\ \dot{E}_{sb} < 0 \quad \text{if} \quad i_b > 0\end{aligned} \tag{7.3}$$

where

$$\begin{aligned} E_{sb} &= S_b - S_{b,t} \\ \Rightarrow \dot{E}_{sb} &= \dot{S}_b \end{aligned} \tag{7.4}$$

We assume that $\dot{E}_{sb}$ can be related to i_b by the following

$$\dot{E}_{sb} = -\alpha_b(t) i_b, \quad \alpha_b(t) > 0 \quad \forall \quad t \geq 0 \tag{7.5}$$

where

$$i_b = \frac{V_L i_L - \bar{\eta}_1 V_{fc}[i_{fc,t} - g(E_s) - \delta_{b1}]}{\bar{\eta}_3 V_b} \tag{7.6}$$

replacing $i_{fc,t}$ by $E_{fc,t} + i_{fc,d}$

$$i_b = \frac{V_L i_L - \bar{\eta}_1 V_{fc}[E_{fc,t} + i_{fc,d} - g(E_s) - \delta_{b1}]}{\bar{\eta}_3 V_b} \tag{7.7}$$

and

$$i_{fc,d} = \frac{V_L i_L}{\bar{\eta}_1 V_{fc}} + g(E_s) + g(E_{sb}) + \delta_{b1} \tag{7.8}$$

substituting $i_{fc,d}$ into Eq.(7.7), and i_b into Eq.(7.5) then

$$\dot{E}_{sb}E_{sb} = -\frac{\alpha_b(t)E_{sb}}{\bar{\eta}_3 V_b}[V_L i_L - \bar{\eta}_1 V_{fc} E_{fc,t} - \bar{\eta}_1 V_{fc}(\frac{V_L i_L}{\bar{\eta}_1 V_{fc}} + g(E_s) + g(E_{sb}) + \delta_{b1} - g(E_s) - \delta_{b1})] \tag{7.9}$$

simplifying Eq.(7.9)

$$\dot{E}_{sb}E_{sb} = -\frac{\alpha_b(t)E_{sb}}{\bar{\eta}_3 V_b}[-\bar{\eta}_1 V_{fc} E_{fc,t} - \bar{\eta}_1 V_{fc} g(E_{sb})] \tag{7.10}$$

$g(E_{sb})$ is designed to be

$$g(E_{sb}) = -k_b E_{sb} \tag{7.11}$$

thus

$$\dot{E}_{sb}E_{sb} = \frac{\alpha_b(t)E_{sb}\bar{\eta}_1 V_{fc} E_{fc,t}}{\bar{n}_3 V_b} - \frac{\alpha_b(t)E_{sb}^2 \bar{\eta}_1 V_{fc} k_b}{\bar{\eta}_3 V_b} \tag{7.12}$$

Now let us find the expression of $\dot{E}_s E_s$

$$\dot{E}_s = \frac{-i_{uc}}{C V_{max}} \tag{7.13}$$

where

$$i_{uc} = \frac{V_L i_L - \eta_1 V_{fc} i_{fc} - \eta_3 V_b i_b}{\eta_2 V_{uc}} \tag{7.14}$$

and

$$i_{fc} = E_{fc} + E_{fc,t} + i_{fc,d} \tag{7.15}$$

replacing $i_{fc,d}$ with its value as in Eq .(7.8)

$$i_{fc} = E_{fc} + E_{fc,t} + \frac{V_L i_L}{\bar{\eta_1} V_{fc}} + g(E_s) + g(E_{sb}) + \delta_{b1} \tag{7.16}$$

i_b is given in Eq .(7.7)

$$i_{uc} = \frac{1}{\eta_2 V_{uc}}[V_L i_L - \eta_1 V_{fc}(E_{fc} + E_{fc,t} + \frac{V_L i_L}{\bar{\eta_1} V_{fc}} + g(E_s) + g(E_{sb}) + \delta_{b1})] - (\frac{\eta_3 V_b}{\eta_2 V_{uc}}) \frac{V_L i_L - \bar{\eta_1} V_{fc}[E_{fc,t} + i_{fc,d} - g(E_s) - \delta_{b1}]}{\bar{\eta_3} V_b} \tag{7.17}$$

Simplifying Eq .(7.17) and replacing $g(E_s) = -k_s E_s$, $g(E_{sb}) = -k_b E_{sb}$, and $i_{fc,d}$ as Eq.(7.8)

$$i_{uc} = [\frac{V_L i_L}{\eta_2 V_{uc}}[1 - \frac{\eta_1}{\bar{\eta_1}}] + \frac{\eta_3 V_{fc}}{\eta_2 V_{uc}}[\frac{\eta_1}{\eta_3} - \frac{\bar{\eta_1}}{\bar{\eta_3}}]k_b E_{sb} - \frac{\eta_1 V_{fc} E_{fc}}{\eta_2 V_{uc}} - \frac{\eta_3 V_{fc}}{\eta_2 V_{uc}}[\frac{\eta_1}{\eta_3} - \frac{\bar{\eta_1}}{\bar{\eta_3}}]E_{fc,t} + \frac{\bar{\eta_1} V_{fc} k_s E_s}{\eta_2 V_{uc}} - \frac{\bar{\eta_1} V_{fc} \delta_{b1}}{\eta_2 V_{uc}}] \tag{7.18}$$

Substituting Eq .(7.18) into Eq .(7.13) and defining

$e_{13} = [\frac{\eta_1}{\eta_3} - \frac{\bar{\eta_1}}{\bar{\eta_3}}]$

thus

$$\dot{E}_s E_s = \frac{-E_s}{C V_{max}}(\frac{V_L i_L}{\eta_2 V_{uc}}[1 - \frac{\eta_1}{\bar{\eta_1}}] + \frac{\eta_3 V_{fc}}{\eta_2 V_{uc}} e_{13} k_b E_{sb} - \frac{\eta_1 V_{fc} E_{fc}}{\eta_2 V_{uc}} - \frac{\eta_3 V_{fc}}{\eta_2 V_{uc}} e_{13} E_{fc,t} + \frac{\bar{\eta_1} V_{fc} k_s E_s}{\eta_2 V_{uc}} - \frac{\bar{\eta_1} V_{fc} \delta_{b1}}{\eta_2 V_{uc}}) \tag{7.19}$$

Substituting Eq.(4.18), Eq.(4.33), Eq .(7.12) and Eq.(7.19) into Eq.(7.2)

$$\dot{\bar{V}} \leq -\mathcal{E}_b^T Q_b \mathcal{E}_b + \frac{E_{fc}(\beta - \delta_2)}{k_d} - \frac{E_s}{CV_{max}}[\frac{V_L i_L}{\eta_2 V_{uc}}(1 - \frac{\eta_1}{\bar{\eta}_1}) - \frac{\eta_1 V_{fc}\delta_{b1}}{\eta_2 V_{uc}}] \tag{7.20}$$

where,

$$\mathcal{E}_b = \begin{bmatrix} E_s \\ E_{fc,t} \\ E_{fc} \\ E_{sb} \end{bmatrix}, \quad Q_b = \begin{bmatrix} \frac{\bar{\eta}_1 V_{fc} k_s}{\eta_2 V_{uc} C V_{max}} & \frac{-\eta_1 V_{fc} e_{13}}{2\eta_2 V_{uc} C V_{max}} & \frac{-\eta_1 V_{fc}}{2\eta_2 V_{uc} C V_{max}} & \frac{\eta_3 V_{fc} e_{13} k_b}{2\eta_2 V_{uc} C V_{max}} \\ \frac{-\eta_3 V_{fc} e_{13}}{2\eta_2 V_{uc} C V_{max}} & \alpha_3 & 0 & \frac{-\alpha_b(t)\bar{\eta}_1 V_{fc}}{2\bar{\eta}_3 V_b} \\ \frac{-\eta_1 V_{fc}}{2\eta_2 V_{uc} C V_{max}} & 0 & \alpha & 0 \\ \frac{\eta_3 V_{fc} e_{13} k_b}{2\eta_2 V_{uc} C V_{max}} & \frac{-\alpha_b(t)\bar{\eta}_1 V_{fc}}{2\bar{\eta}_1 V_b} & 0 & \frac{\alpha_b(t)\bar{\eta}_1 V_{fc} k_b}{\bar{\eta}_3 V_b} \end{bmatrix} \tag{7.21}$$

In Eq.(7.21) , note that Q_b is symmetric. Also, note that k_s , k_b and α are tunable positive constants. α_3 is not tunable because it depends on the dynamic of the fuel supply system, but it is positive. So, by tuning appropriately the tunable parameters, we can ensure that $Q_b > 0$. Furthermore, from the *Rayleigh-Ritz Inequality* [62],

$$\mathcal{E}_b^T Q_b \mathcal{E}_b \geq \inf\left(\lambda_{min,Q_b}\right) ||\mathcal{E}_b||^2 > 0 \quad \forall\, \mathcal{E}_b \neq 0 \tag{7.22}$$

where λ_{min,Q_b} represent the smallest eigen values of Q_b at any time. Now to ensure that $\dot{V}$ ≤ 0 we need to tune δ_{b1} and δ_{b2} as follows

$$\begin{array}{rcl} [\frac{V_L i_L}{\eta_2 V_{uc}}(1 - \frac{\eta_1}{\bar{\eta}_1})]\frac{\eta_2 V_{uc}}{\eta_1 V_{fc}} & \geq & \delta_{b1} \quad \text{if} \quad E_s \geq 0 \quad \text{and} \\ [\frac{V_L i_L}{\eta_2 V_{uc}}(1 - \frac{\eta_1}{\bar{\eta}_1})]\frac{\eta_2 V_{uc}}{\eta_1 V_{fc}} & \leq & \delta_{b1} \quad \text{if} \quad E_s \leq 0 \end{array} \tag{7.23}$$

and

$$\beta \leq \delta_2 \tag{7.24}$$

Note that the conditions in Eqs.(7.23) and (7.24) are implementable, because β, as well as all the voltages and the current are all measurable. Although the efficiencies η_1 and η_2 are not known, their upper and lower bounds can be estimated. Thus we conclude that $\dot{V} \leq 0$ and the design system is stable under these operating conditions.

Chapter 8

Conclusions and Future Work

This thesis addresses the control of a hybrid SOFC ultra-capacitor system. For the SOFC, the fuel starvation problem is addressed by controlling the fuel utilization, U. Transient control of U is achieved using a steady-state property of the fuel cell. Transient deviation of U from its target is attenuated using a feedback based current regulation method. In addition, the thesis assumes a general stability behavior of the fuel supply system without precise knowledge of its dynamics. An ultra-capacitor is used for compensating the excess or deficit power during transients.

Two control designs are proposed. The first is a robust nonlinear control strategy for which stability properties of the closed-loop system are proved. The second is a standard robust H_∞ approach. Both address multiple objectives: minimizing the fluctuation in the fuel cell utilization during transients in power demand, maintaining a constant ultra-capacitor SOC, and the control strategies are required to be robust to uncertainties of the system. An experimental test-stand is developed, consisting of an emulated SOFC and actual ultra-capacitor and power-electronics components, forming a laboratory scale hybrid power grid. Both control strategies show comparable performance on this platform.

Next the hybrid system is expanded to high power applications, where conditions such as saturated fuel flow, limiting current density of fuel cell, and limiting ultra-capacitor current, are more likely to occur. To prevent these scenarios, an investigation is conducted to improve the performance of the hybrid system with an additional energy storage element. It is found that combining the ultra-capacitor with a lithium-ion battery is potentially a

winning combination. Lithium-ion batteries are characterized by high energy density and light weight, and ultra-capacitors are characterized by high efficiency and durability. In combination, they can protect the SOFC from the transients in power demand and improve the ability of the hybrid system to operate in high power applications.

A nonlinear control strategy is developed for the combined lithium-ion and ultra-capacitor hybrid system. The strategy addresses multiple objectives: minimizing the fluctuation in U, maintaining a constant ultra-capacitor and battery SOCs, be robust to uncertainties of the system, and extending the lifetime of the battery.

In future work, test stand experiments are required to validate the designed control approach for SOFC Ultra-capacitor Battery system. A switching mechanism for measurements of the lithium-ion battery V_{oc} is required. Furthermore, the hybrid system could be extended to multiple power sources such solar cells, and wind turbines. A smart grid control design will be required for such complex hybrid systems.

Another area of future work is the feedback based current shaping method discussed is section 2.4. In its current state of development, it only compensates for delay D1 introduced by the fuel supply system dynamics. For complete disturbance rejection, the i_{fc} regulation needs to include the delay D_2 introduced by the dynamics of fuel processor. Future research is required to attempt to incorporate this delay using a model-independent or observer-based approach.

References

[1] http://www1.eere.energy.gov/hydrogenandfuelcells/fuelcells/m.html/.

[2] A. J. Slippey. Dynamic modeling and analysis of multiple sofc system configurations. Master's thesis, Rochester Institute of technology, 2009.

[3] http://www.maxwell.com/ultracapacitors/index.html.

[4] http://www.dspaceinc.com/.

[5] http://www.sorensendcpowersupplies.com/.

[6] http://www.zahninc.com/.

[7] http://www.tequipment.net/.

[8] http://www.valence.com/.

[9] http://hydrogen.energy.gov/.

[10] J. T. Pukrushpan, A. G. Steafanpoulou, and H. Peng. *Control of Fuel Cell Power Systems*. Springer, 2004.

[11] X. Li. *Principles of Fuel Cells*. Taylor and Francis Group, 2006.

[12] J. Larminie and A. Dicks. *Fuel Cell Systems Explained*. John Wiley & Sons, Inc., second edition, 2003.

[13] J. R. Meacham, F. Jabbari, J. Brouwer, J. L. Mauzey, and G. Scott Samuelsen. Analysis of stationary fuel cell dynamic ramping capabilities and ultra capacitor energy storage using high resolution demand data. *Journal of Power Sources*, 156:472–479, 2006.

[14] T. Das and R. Weisman. A feedback based load shaping strategy for fuel utilization control in sofc systems. *American Control Conference, St. Louis, MO*, 2009.

[15] A. Lazzaretto, A. Toffolo, and F. Zanon. Parameter setting for a tubular SOFC simulation model. *ASME Journal of Energy Resources Technology*, 126:40–46, 2004.

[16] K. Sedghisigarchi and A. Feliachi. Control of grid-connected fuel cell power plant for transient stability enhancement. *IEEE Power Engineering Society Transmission and Distribution Conference*, 1:383–388, 2002.

[17] W. Schmittinger and A. Vahidi. A review of the main parameters influencing long term performance and durability of pem fuel cells. *Journal of Power Sources*, 180:1–14, 2008.

[18] F. Mueller, J. Brouwer, F. Jabbari, and S. Samuelsen. Dynamic simulation of an integrated solid oxide fuel cell system including current-based fuel flow control. *ASME Journal of Fuel Cell Science and Technology*, 3:144–154, 2006.

[19] F. Bidault, D. J. L. Brett, P. H. Middleton, and N.P. Brandon. Review of gas diffusion cathodes for alkaline fuel cells. *Journal of Power Sources*, 187:39–48, 2009.

[20] B. Y. S. Lin, D. W. Kirk, and S. J. Thorpe. Performance of alkaline fuel cells: A possible future energy system? *Journal of Power Sources*, 161:474–483, 2006.

[21] A. Liu and Y. Weng. Performance analysis of a pressurized molten carbonate fuel cell/micro-gas turbine hybrid system. *Journal of Power Sources*, 195:204–213, 2010.

[22] P. M. Biesheuvel and J. J. C. Geerlings. Thermodynamic analysis of direct internal reforming of methane and butane in proton and oxygen conducting fuel cells. *Journal of Power Sources*, 185:1162–1165, 2000.

[23] N. Sammes, R. Bove, and K. Stahl. Phosphoric acid fuel cells: Fundamentals and applications. *Elsevier Ltd*, 8:372–378, 2004.

[24] C. Wang and A. J. Appleby. High-peak-power polymer electrolyte membrane fuel cells. *Center for Electrochemical Systems and Hydrogen Research*, 150:A493–A498, 2003.

[25] J. J. Baschuk and X. Li. Modelling of polymer electrolyte membrane fuel cells with variable degrees of water flooding. *Journal of Power Sources*, 86:181–196, 2000.

[26] E. Jannelli, M. Minutillo, and E. Galloni. Performance of a polymer electrolyte membrane fuel cell system fueled with hydrogen generated by a fuel processor. *Journal of Fuel Cell Science and Technology*, 4:435–440, 2007.

[27] A. Drolia, P. Jose, and N. Mohan. An approach to connect ultracapacitor to fuel cell powered electric vehicle and emulating fuel cell electrical characteristics using switched mode converter. *Proceedings of Industrial Electronics Conference*, pages 897–901, 2003.

[28] P. Thounthong, S. Rael, and B. Davat. Control strategy of fuel cell/supercapacitors hybrid power sources for electric vehicle. *Journal of Power Sources*, 158:806–814, 2006.

[29] A. Vahidi, A. Stefanopoulou, and H. Peng. Current management in a hybrid fuel cell power system: A model-predictive control approach. *IEEE Transactions on Control Systems Technology*, 14(6):1047 – 1057, 2006.

[30] J. Sun and I. Kolmanovsky. Load governor for fuel cell oxygen starvation protection: A robust nonlinear reference governor approach. *Proceeding of the 2004 American Control Conference, Boston, MA June 30 - July 2*, pages 828–833, 2004.

[31] A. Arce, A. J. del Real, and C. Bordons. MPC for battery/fuel cell hybrid vehicles including fuel cell dynamics and battery performance improvement. *Journal of Process Control*, 19:12891304, 2009.

[32] M. Uzunoglu and M. S. Alam. Dynamic modeling, design and simulation of a pem fuel cell/ultracapacitor hybrid system for vehicular applications. *Energy Conversion and Management*, 48:1544–1553, 2007.

[33] V. Paladini, T. Donateo, A. de Risi, and D. Laforgia. Super-capacitor fuel-cell hybrid electric vehicle optimization and control strategy development. *Energy Conversion and Management*, 48:3001–3008, 2007.

[34] A. Hajizadeh and M. A. Golkar. Intelligent power management strategy of hybrid distributed generation systems. *Electrical Power and Energy Systems*, 29:783–795, 2007.

[35] Z. Jiang, L. Gao, and R. A. Dougal. Adaptive control strategy for active power sharing in hybrid fuel cell/battery power sources. *IEEE Transactions on Energy Conversion*, 22(2):507–515, 2007.

[36] E. M. Fleming and I. A. Hiskens. Dynamics of a microgrid supplied by solid oxide fuel cells. *iREP Symposium - Bulk Power System Dynamics and Control - VII, Charleston, SC*, 2007.

[37] M.Y.Ayad, M.Becherif, A.Djerdir, and A.Miraoui. Sliding mode control for energy management of dc hybrid power sources using fuel cell, batteries and supercapacitors. *International Conference on Clean Electrical Power*, pages 500–505, 2007.

[38] P. Rodatz, G. Paganelli, A. Sciarretta, and L. Guzzella. Optimal power management of an experimental fuel cell/supercapacitor-powered hybrid vehicle. *Control Engineering Practice*, 13:4153, 2005.

[39] A. Payman, S. Pierfederici, and F. Meibody-Tabar. Energy control of supercapacitor/fuel cell hybrid power source. *Energy Conversion and Management*, 49:1637–1644, 2008.

[40] M. Fliess, J. Levine, P. Martin, and P. Rouchon. Flatness and defect of nonlinear systems: Introductory theory and examples. *International Journal of Control*, 61(6):1327–1361, 1995.

[41] R. Bove and S. Ubertini. *Modeling Solid Oxide Fuel Cells: Methods Procedures and Techniques*. Fuel Cells and Hydrogen Engergy. Springer, 1st edition, 2008.

[42] S. Campanari. Thermodynamic model and parametric analysis of a tubular SOFC module. *Journal of Power Sources*, 92:26–34, 2001.

[43] H. Gorgun, M. Arcak, S. Varigonda, and S. A. Bortoff. Observer designs for fuel processing reactors in fuel cell power systems. *International Journal of Hydrogen Energy*, 30:447–457, 2005.

[44] T. Das. An adaptive observer design for recirculation based solid oxide fuel cell systems using cell voltage measurement. *American Control Conference, St. Louis, MO.*, 2009.

[45] V. Tsourapas, A. G. Stefanopoulou, and J. Sun. Model-based control of an integrated fuel cell and fuel processor with exhaust heat recirculation. *IEEE Transactions on Control Systems Technology*, 15(2):233–245, 2007.

[46] R. Kandepu, L. Imsland, B. A. Foss, C. Stiller, B. Thorud, and O. Bolland. Modeling and control of a SOFC-GT-based autonomous power system. *Energy*, 32:406–417, 2007.

[47] A. F. Burke. Batteries and ultracapacitors for electric, hybrid, and fuel cell vehicles. *Proceedings of the IEEE*, 95:806–820, 2007.

[48] J. Bauman and M. Kazerani. A comparative study of fuel-cellbattery, fuel-cellultracapacitor, and fuel-cellbatteryultracapacitor vehicles. *IEEE Transaction on Vehicular Technology*, 2:760–769, 2008.

[49] D. D. Domenico, G. Fiengo, and A. Stefanopoulou. Lithium-ion battery state of charge estimation with a kalman filter based on a electrochemical model. *IEEE International Conference on Control Applications*, 1:702–707, 2008.

[50] S. Lee, J. Kim, J. Lee, and B. H. Cho. State of charge and capacity estimation of lithium-ion battery using a new open-circuit voltage versus state of charge. *Journal of Power Sources*, 185:1367–1373, 2008.

[51] M. L. Ferrari, A. Traverso, L. Magistri, and A. F. Massardo. Influence of anodic recirculation transient behavior on the SOFC hybrid system performance. *Journal of Power Sources*, 149:22–32, 2005.

[52] A. Y. Karnik and J. Sun. Modeling and control of an ejector based anode recirculation system for fuel cells. *Proceedings of ASME Fuel Cell 2005*, pages 721–731, 2005.

[53] T. Das, S. Narayanan, and R. Mukherjee. Steady-state and transient analysis of a steam reformer based solid oxide fuel cell system. *ASME Journal of Fuel Cell Science and Technology*, 7:1–20, 2010.

[54] J. Xu and G. F. Froment. Methane steam reforming, methanation and water-gas shift: I. Intrinsic kinetics. *AIChE Journal*, 35(1):88–96, 1989.

[55] R. Bove, P Lunghi, and N. M. Sammes. SOFC mathematic model for systems simulations - part 2: Definition of an analytical model. *International Journal of Hydrogen Energy*, 30:189–200, 2005.

[56] T. R. Crompton. *Battery reference Book*. Newnes, 2000.

[57] http://www.tms.org/.

[58] G. A. Nazri and G. Pistoiam. *Lithium Batteries science and technology*. Klumer Acadimic Publisher, 2004.

[59] A. G. Stefanopoulou and K. Suh. Mechatronics in fuel cell systems. *Control Engineering Practice*, 15:277289, 2007.

[60] H. Khalil. *Nonlinear Systems*. Prentice-Hall, Inc. Upper Saddle River, NJ, 3 edition, 2002.

[61] J-J E.Slotine and W.Li. *Applied Nonlinear Control*. Prentice Hall, 1991.

[62] W. J. Rugh. *Linear System Theory*. Prentice Hall, Upper Saddle River, NJ, 2 edition, 1996.

[63] S. Skogestad and I. Postlethwaite. *Multivariable Feedback Control: Analysis and Design*. John Wiley & Sons, Ltd., 2 edition, 2005.

[64] T. Das, S. Narayanan, and R. Mukherjee. Model based characterization of transient response of a solid oxide fuel cell system. *ASME International Mechanical Engineering Congress and Exposition*, pages 655–664, 2007.

[65] http://www.epa.gov/otaq/emisslab/testing/dynamometer.htm/.

Appendix A

Nonlinear Setup and Control-Desk control interfacing

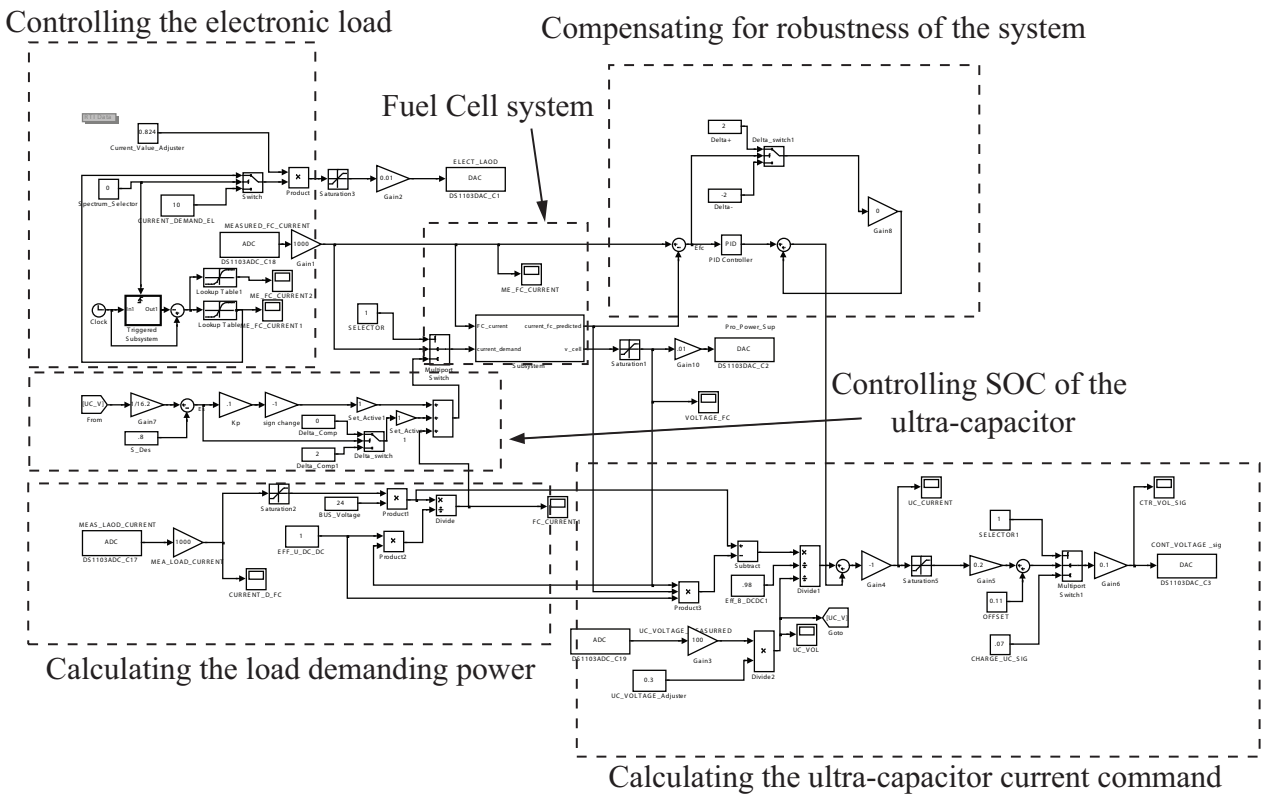

Figure A.1: The Overall Simulink Model of the Hybrid System with Nonlinear Controller

The Simulink setup for the nonlinear control system is presented in Fig.A.1. As discussed in section 4.2 , the nonlinear controller maintains the state of charge of the ultracapacitor at the desired level. The fuel cell current is shaped to reduce drastic fluctuation in fuel utilization. Also, the robustness in the hybrid system are considered. All these control constrains are designed and highlighted in Fig.A.1. As discussed in section 5.8, all the sensor input and the power electronics control outputs are interfaced through dSPACE into the presented Simulink setup shown above. In the experimental setup, the control parameters

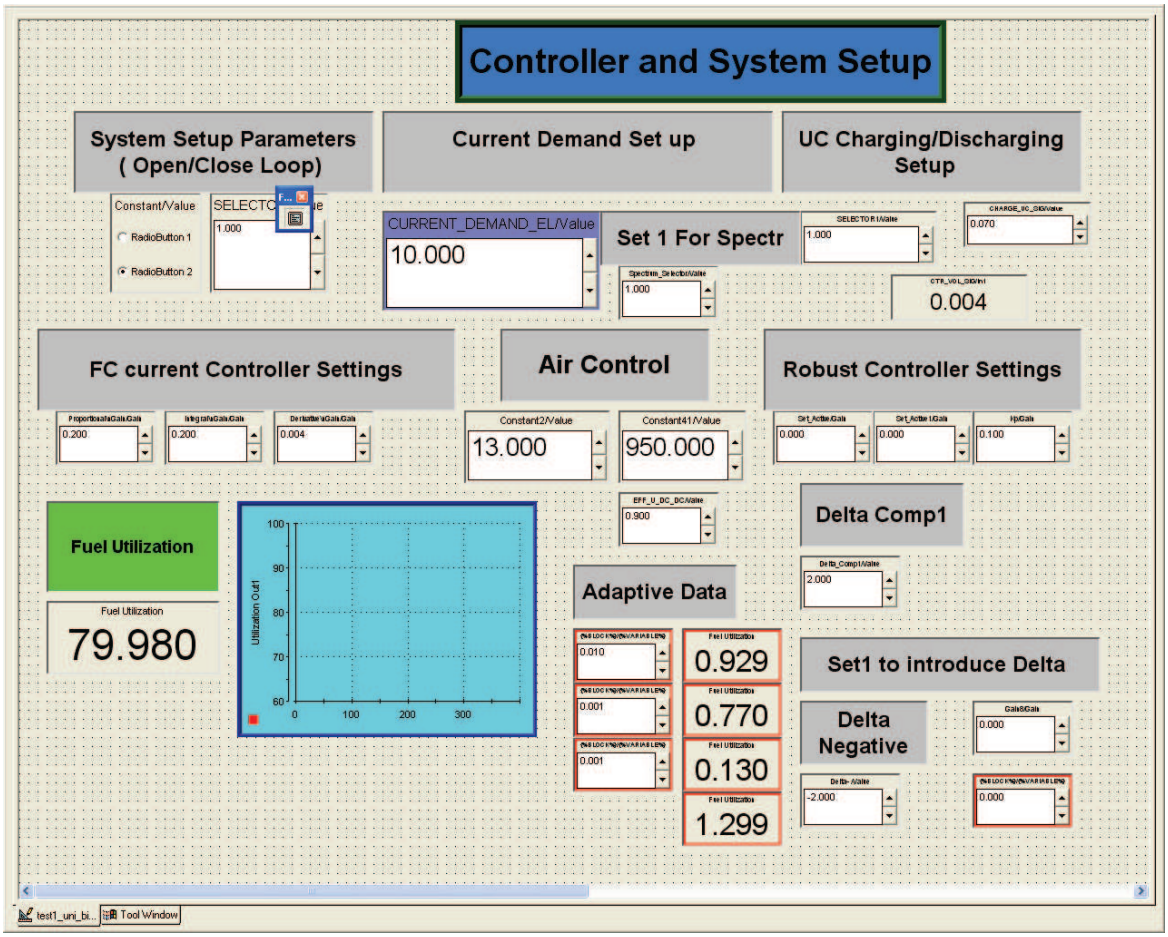

Figure A.2: Control and System Setup Using Control-Desk Interface Software

and system setup can be adjusted in real time by using the Control-Desk software as shown in Fig A.2. In addition, all the sensed signals are displayed in real time as shown in Fig.A.3.

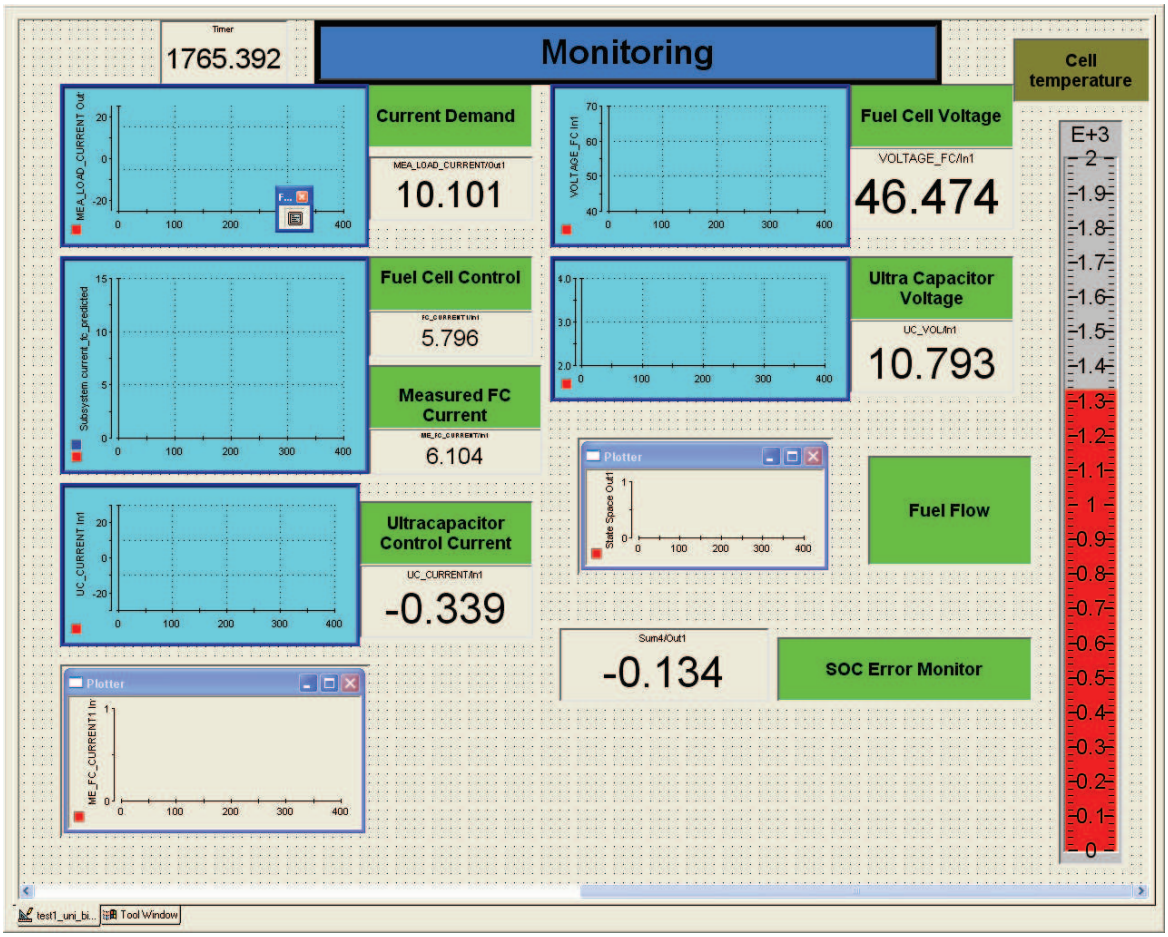

Figure A.3: Monitoring Setup Using Control-Desk Interface Software

Appendix B

H_∞ Matlab Code and Simulink Setup

The following Matlab code is used to assign all the weights of the developed state space model discussed in section 4.3. The second part of the code designs the H_∞ controller and checks the stability of the close-loop system.

```
%                                   PART I
%  Tahar  Allag
%  function  name : ex_INTPRO_G
%  This  function  forms  the  Generalized  Plant
%  for  a  standard  feedback  configuration.
%  All  design  weights  are  defined  here.
%  Testing  with  Matlab  7.x
clear all
Init − all
clc
s = tf('s'); % a convenient trick for transfer functions
assignin('base','s',s); % export s to the workspace
open  GenPlant_Int
P = 0.015 ; %  taken  as  nominal  P
% weights % Setting the weights here
```

$Wr = 1$; % *can be a filter*

$Wn = 1/16.2$; % *depends on max Vuc*

$Wdelta = 0.9$; %

$Wd = 0.1$; %

$Wy = makeweight(10, 1, 0.0005)$;

$n1 = ureal('n1', 0.91, 'Range', [0.90.92])$;

$n2 = ureal('n2', 0.9, 'Range', [0.880.92])$;

% *Number of measurements* (y) *and control* (u)

$ny = 1$

$nu = 1$

% *Export variables* $(e.g., weights)$ *to workspace*

$assignin('base', 'P', P)$;

$assignin('base', 'Wr', Wr)$;

$assignin('base', 'Wn', Wn)$;

$assignin('base', 'Wdelta', Wdelta)$;

$assignin('base', 'Wd', Wd)$;

$assignin('base', 'Wy', Wy)$;

$assignin('base', 'ny', ny)$;

$assignin('base', 'nu', nu)$;

% *Generalized Plant*

$load\_system('GenPlant\_Int')$; % *load simulink model into workspace*

$[a, b, c, d]$=$linmod('GenPlant\_Int')$; % *extract the LTI model*

% $open\_system('GenPlant\_Int')$;

$G = ss(a, b, c, d)$ % *Form State − Space LTI object*

$assignin('base', 'G', G)$ % *export to workspace*

%

%%%%%

%

```
%                                   PART II
%  m_file :  H - infinity  with  weights
%  Testing  with  Matlab
%  This  m_file  calls  the  above  function  name : ex_INTPRO_G
clc
format compact
format short
echo on
Form Generalized Plant
%  Form  Generalized  Plant
ex_INTPRO_G
%  Synthesis  of  Controllers  (H∞)
tol = 1e-2;  %  tolerance  should  not  be  too  small
gmin = 0;  gmax = 10;  %  range  for  gamma  iteration
[K, Tzw, gopt] = hinfsyn(G, ny, nu, gmin, gmax, tol)
%  controller
%  Form  stardard  "Plant"  without  design  weights
load_system('GenPlant_NoInt');  %  load  model  into  workspace
[a, b, c, d]=linmod('GenPlant_NoInt');  %  extract  the  LTI  model
close_system ('GenPlant_NoInt');  %  close  simulink  model
P = ss(a, b, c, d);
%  Check  the  closed  loop.
%  with  H - infinity  controller.
Tzw = lft(P, K); %  close  the  loop
if  prod(1. * [pole(Tzw)≤ 0])  %  Check  poles  in  LHP
disp('Closed  Loop  is  Unstable')
end;
```

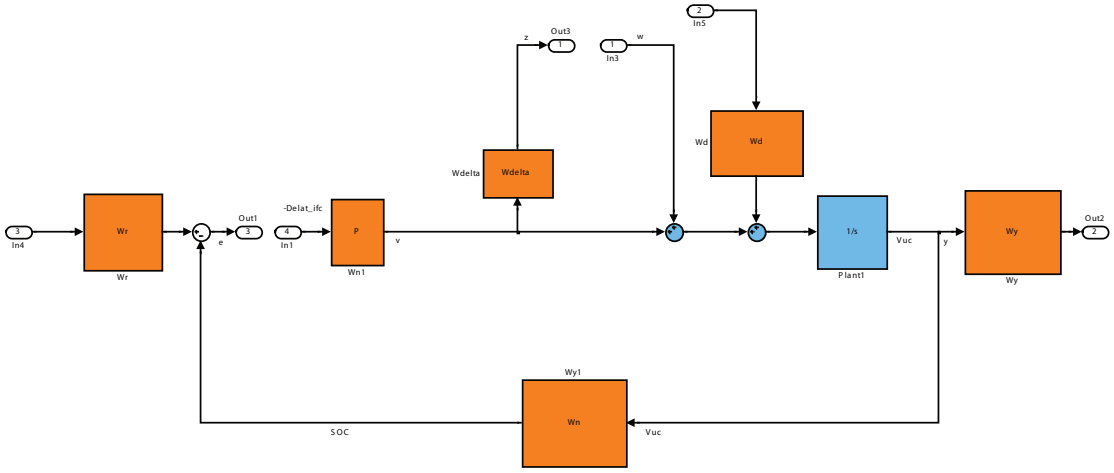

Figure B.1: Standard H_∞ Simulink Model with Weights

The above Matlab code calls the Simulink model shown in Fig.B.1. This model represents the standard H_∞ set up of the hybrid system with modeled uncertainties and disturbances. A prototype Simulink model of the hybrid system and the designed controller is represented in Fig.B.2. This model is used to test the performance of the H_∞ controller before applying it to the hardware setup. The same SOFC system is used as in the hardware and the DC/DC converters and the ultra-capacitor are model.

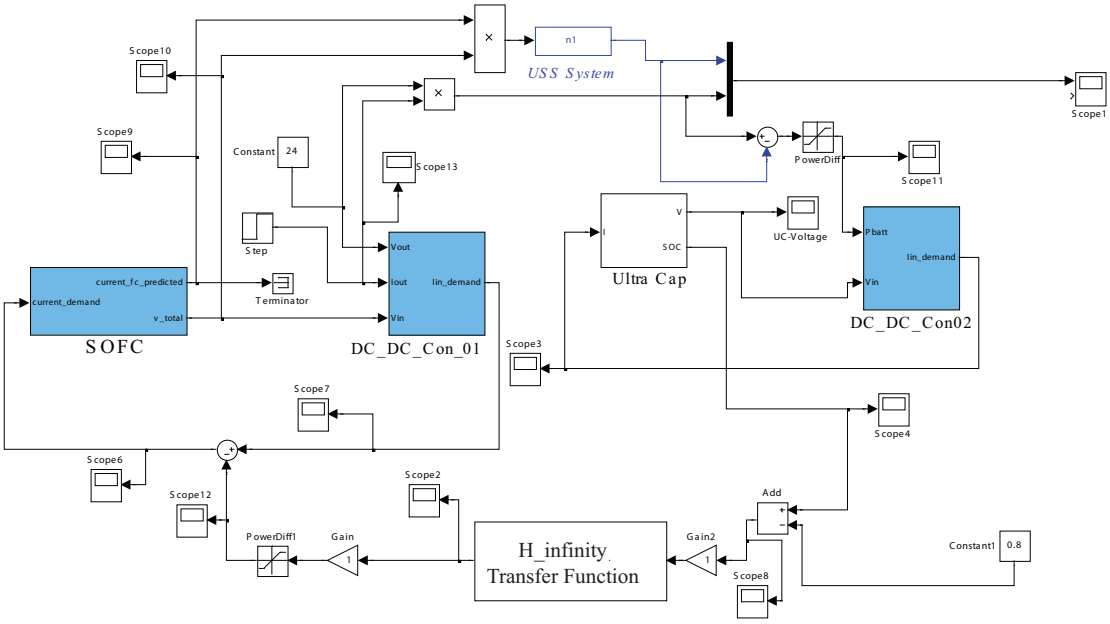

Figure B.2: Simulink Model of the Hybrid System with H_∞ Model

Appendix C

Future Work

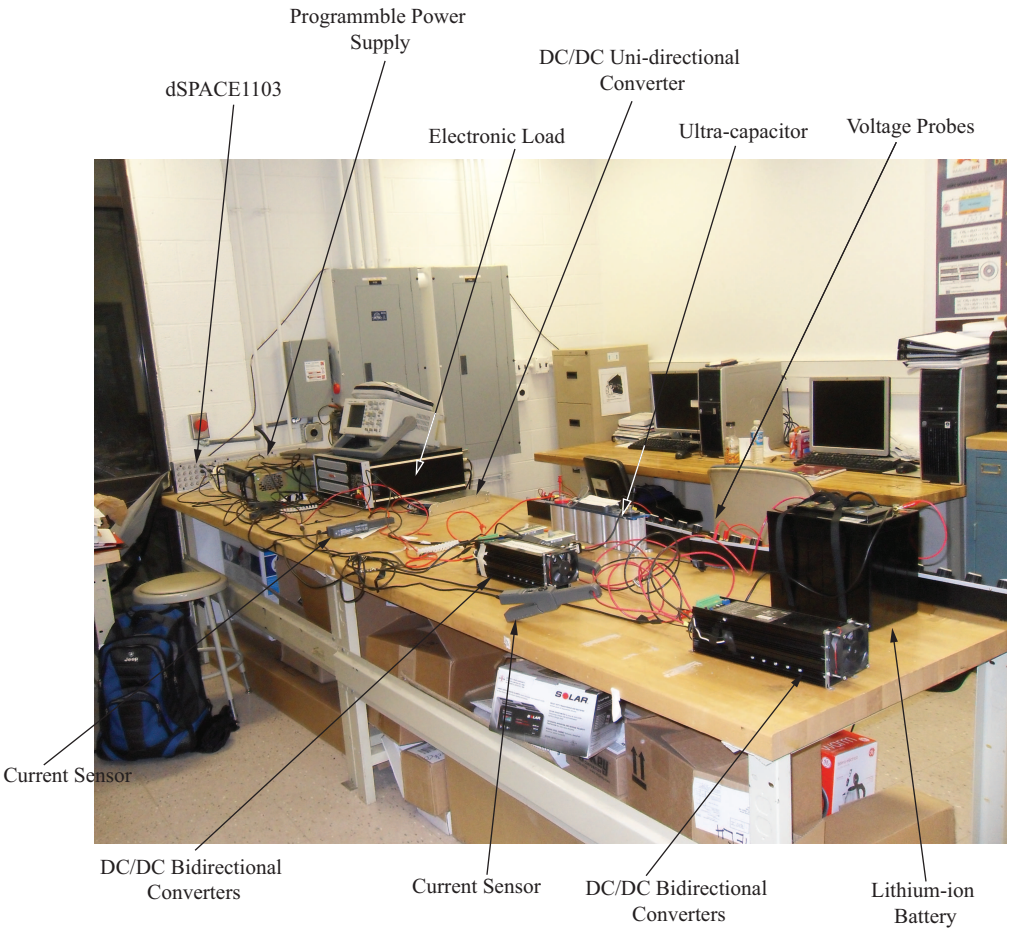

Figure C.1: Preliminary Hardware Setup for Ultra-capacitor Battery SOFC Hybrid System

In future work, the nonlinear control developed in section 7.2 needs to be tested in the hardware to validate the performance of the strategy. A primarily test stand setup for the battery ultra-capacitor is shown in Fig.C.1. This test stand setup is not yet completely designed, and a lot of improvement needs to be addressed in future work.

First of all, the hybrid system nominal operating power needs to be at least from 5KW to 10KW. Consequently, high power wires are required. Also, the SD-1000L-24 unidirectional DC/DC converter used in the previous test stand setup described in section 5, is designed only for maximum current of 50A at the output. This does not support the required power, thus it is required to be changed. To satisfy safety requirements during tests, fuses and circuit breakers are required for the system. dSPACE 1103 has 38 analog to digital and digital to analog converters. These is largely enough to the required test stand. The DC5050F-SU bidirectional DC/DC converter is designed to draw up to 50A which is enough for the ultra-capacitor. However, the battery is required to supply the system with high power, thus high power bidirectional DC/DC is needed. The maximum voltage of the lithium-ion battery is 12.6V, thus the voltage probes explained in section 5.4 can be used to measured the open-circuit voltage of the battery. However, a switching mechanism is needed to disconnect the battery from the grid. Also, the 80i-110 AC/DC current probes can be used for this set up because they have 10mV/A range.